A HIGH RESOLUTION STUDY OF PROTON RESONANCES IN ^{55}Co, ^{59}Cu, and ^{61}Cu

DAVID S. FLYNN

Triangle Universities Nuclear Laboratory
Department of Physics
Duke University

1976

A HIGH-RESOLUTION STUDY OF PROTON RESONANCES IN ^{55}Co, ^{59}Cu, AND ^{61}Cu

by

David Sheldon Flynn

Department of Physics
Duke University

Date: _____

Approved:

_____

E. G. Bilpuch, Supervisor

_____

_____

_____

_____

A dissertation submitted in partial fulfillment of the requirements for the degree of Doctor of Philosophy in the Department of Physics in the Graduate School of Arts and Sciences of Duke University

1976

ABSTRACT

(Physics)

A HIGH-RESOLUTION STUDY OF PROTON RESONANCES IN ^{55}Co, ^{59}Cu, AND ^{61}Cu

by

David Sheldon Flynn

Department of Physics
Duke University

Date:_____

Approved:

_____

E. G. Bilpuch, Supervisor

_____

_____

_____

_____

An abstract of a dissertation submitted in partial fulfillment of the requirements for the degree of Doctor of Philosophy in the Department of Physics in the Graduate School of Arts and Sciences of Duke University

1976

A HIGH-RESOLUTION STUDY OF PROTON RESONANCES IN ^{55}Co, ^{59}Cu, AND ^{61}Cu

by

David Sheldon Flynn

In the past several years, experiments measuring proton excitation functions for all available even-even isotopes in the mass region $40 \leq A \leq 64$ have been performed at the Triangle Universities Nuclear Laboratory. Particular emphasis has been placed on the study of fragmented analogue states. Statistical properties of the proton resonances have also been investigated. The overall energy resolution (with solid targets) was about 300 eV. Due to voltage limitations of the high-resolution system, the beam energies have been limited to 3.3 MeV or less. One purpose of this work was to develop a new system which would make possible the extension of these experiments to higher energies.

The energy range of an electrostatic-analyzer homogenizer system was extended by the introduction of a molecular dissociator which operated on the diatomic hydrogen ions from the Van de Graaff accelerator. Energy resolutions of 300 to 400 eV with solid targets were obtained routinely up to proton energies of 4.5 MeV with an electrostatic analyzer originally limited to measuring

proton energies below 2.7 MeV. Improvements to the Van de Graaff accelerator are expected to permit this system to operate as high as 5 or 6 MeV.

In earlier experiments, rather low level densities were observed in the nuclei ^{55}Co, ^{59}Cu, and ^{61}Cu. These nuclei thus seemed particularly suitable for study at higher energies. In addition, systematic investigations of s-wave strength functions indicated that ^{55}Co has anomalously low s-wave strength below 3.3 MeV. The second purpose of this work was to investigate ^{55}Co, ^{59}Cu, and ^{61}Cu by proton bombardment at energies above 3.3 MeV.

Proton elastic and inelastic scattering excitation functions were measured for ^{54}Fe (E_p = 3.28 to 4.53 MeV), ^{58}Ni (E_p = 3.11 to 4.20 MeV), and ^{60}Ni (E_p = 2.95 to 3.45 MeV). The excitation functions were measured at 160°, 122°, 105°, and 90° for the elastically scattered protons and 160°, 122°, and 90° for the inelastically scattered protons. The data were fit with an R-matrix code; resonance parameters were extracted for 131 resonances in ^{55}Co, 86 resonances in ^{59}Cu, and 75 resonances in ^{61}Cu.

Four isobaric analogue resonances (IAR) were positively identified in ^{55}Co and seven were tentatively identified. Two IAR were positively identified in ^{59}Cu and four were tentatively identified. Coulomb energies and spectroscopic factors were determined. Spins, parities, and spectroscopic factors of the IAR are in excellent agreement with

those of the parent states; Coulomb energies agreed well with that of the ground state for both ^{55}Co and ^{59}Cu.

An analysis of the statistical fluctuations of the reduced widths was performed on several species of levels of ^{55}Co and ^{59}Cu. The spin and energy dependence of level densities in ^{55}Co and ^{59}Cu were investigated. Proton strength functions were determined for each spin and parity with $\ell<3$ for ^{55}Co and ^{59}Cu, and for $\ell=0,1$, and 2 for ^{61}Cu. The anomalous behavior of the proton s-wave strength function of ^{55}Co was examined.

ACKNOWLEDGEMENTS

I would like to thank my advisor, Dr. E. G. Bilpuch, for suggesting these experiments and for his advice and support throughout the work. Special thanks go to Dr. G. E. Mitchell for his advice throughout the course of this work and in particular in the preparation of this dissertation. I would especially like to express my appreciation to Dr. L. W. Seagondollar for his enthusiastic and dedicated support and for the many hours he spent in the laboratory helping to perform the experiments. The support of Dr. H. W. Newson is greatly appreciated.

The advice of Dr. J. D. Moses and Dr. W. C. Peters in the early stages of this experiment is appreciated. For stimulating discussions and helpful advice, I owe a special thanks to Dr. D. A. Outlaw. Thanks go to Mr. W. K. Wells for assistance in performing some preliminary measurements and to Mr. K. A. Sage for several stimulating discussions. Discussions with Dr. S. Maripuu, Dr. R. Y. Cusson, and Dr. W. J. Thompson have been of great value.

The professional manner in which Mr. S. Edwards, Mr. R. L. Rummel, and Mr. A. W. Lovette performed the necessary construction and maintenance required for the equipment used in this experiment is gratefully acknowledged. Many

hours were contributed by Mrs. Joseph Bailey and Mr. J. D. Turner in the preparation of the figures in this dissertation.

I would like to give a special thanks to Mr. Daniel Blackwelder and to Mr. William McCord for initially giving me an appreciation of physics and for their continuing interest in my graduate studies.

I am very grateful to my parents for their continuing encouragement. Perhaps the greatest debt I owe is to my wife, Marilee; her interest and encouragement has been a great source of strength. Her many hours of assistance in preparing this dissertation is greatly appreciated. I am grateful to L. L. F., S. L. F., and D. A. F. for their patience and understanding.

This work was supported in part by the United States Energy Research and Development Administration. Some of the computations involved were performed at the Triangle Universities Computation Center which is supported in part by the National Science Foundation.

D. S. F.

CONTENTS

LIST OF FIGURES

LIST OF TABLES

A HIGH-RESOLUTION STUDY OF PROTON RESONANCES IN ^{55}Co, ^{59}Cu, AND ^{61}Cu

CHAPTER I

INTRODUCTION

In the past several years, experiments measuring proton excitation functions for all available even-even isotopes in the mass region $40 \leq A \leq 64$ have been performed at the Triangle Universities Nuclear Laboratory. Particular emphasis has been placed on the study of fragmented analogue states. Statistical properties of the proton resonances have also been investigated. The overall energy resolution was $\sim$300 eV. Due to voltage limitations of the high-resolution system, the beam energies have been limited to 3.3 MeV or less. One purpose of this work was to develop a new system which would make possible the extension of these experiments to higher energies.

An electrostatic-analyzer homogenizer system has been developed which extends the range of proton energies to $\sim$5.4 MeV. This was accomplished by dissociating the molecular beam before it entered the analyzer. A description of

this system is given in section II A. The equipment and procedures are discussed in section II B. Corrections for systematic energy-measurement errors are derived and discussed in the appendix.

In earlier experiments, rather low level densities were observed in the nuclei ^{55}Co, ^{59}Cu, and ^{61}Cu. These nuclei thus seemed particularly suitable for study at higher energies. In addition, systematic investigations of s-wave strength functions indicated that ^{55}Co has anomalously low s-wave strength below 3.3 MeV. The second purpose of this work was to investigate ^{55}Co, ^{59}Cu, and ^{61}Cu by proton bombardment at energies above 3.3 MeV.

Proton elastic and inelastic scattering excitation functions were measured for ^{54}Fe (E_p = 3.28 to 4.53 MeV), ^{58}Ni (E_p = 3.11 to 4.20 MeV), and ^{60}Ni (E_p =2.95 to 3.45 MeV). (Although the homogenizer system is capable of operating as high as ~5.4 MeV, the present experiment was limited to energies below ~4.5 MeV due to sparking in the Van de Graaff accelerator. Due to the high level density and low average reduced widths of the resonances, measurements of ^{60}Ni + p were performed only to 3.45 MeV.) The data were fit with an R-matrix code, and resonance parameters were extracted. The fitting procedures and results are presented in chapter III.

The identification and analysis of isobaric analogue resonances is discussed in section IV A. In section IV B an

analysis of the statistical properties of the resonances is presented, and in section IV C the strength functions are presented and discussed.

CHAPTER II

EXPERIMENTAL EQUIPMENT AND PROCEDURES

A. Energy Measurement and Control

1. Introduction

In 1958 a method of canceling energy fluctuations of the beam from a Van de Graaff accelerator was reported (Parks et al. 1958). This system used a cylindrical electrostatic analyzer (ESA) to generate error signals which controlled the voltage on the target. In order to stabilize the system and to improve linearity, the error signal was also fed back (out of phase) to the outer plate of the ESA. This system has been used with the Duke 3 MV Van de Graaff accelerator for over a decade to produce high-resolution nuclear spectroscopic data up to proton energies of 3.3 MeV with an overall energy spread as low as 100 eV on cryogenically pumped gas targets (Keyworth 1968) and 250 eV on solid

targets (Prochnow et al. 1972).

In the attempted extension of this system to energies above 3.3 MeV, difficulties are encountered in maintaining the necessary voltages on the ESA plates. One solution (Dzubay et al. 1972) is to replace the ESA with a magnetic analyzer and to vary the potential on a stripper (through which the control beam passes) to obtain negative feedback. The data presented in this dissertation were obtained with the Duke 4 MV Van de Graaff and an ESA homogenizer system which operated on a proton beam produced when the diatomic molecular hydrogen beam passed through a water vapor dissociator[1]. Since these dissociated protons have close to one-half the energy of the diatomic ions and thus about one-half the energy of the protons which bombard the target, the energy range of the homogenizer system was doubled. Sparking in the Van de Graaff accelerator limited the experiment to proton energies less than 4.5 MeV. Sparking in the 1-meter ESA occurred at an electric field suitable for control at 5.4 MeV.

2. Water-Vapor Dissociator

Sectional views of the dissociator are shown in

---

1. The diatomic beam is a secondary beam produced in the same source and accelerated by the same potential as the primary proton beam used to perform the experiment.

figure 1. The beam passed through a region of water vapor in the dissociation canal and was transformed from an ionized diatomic beam (HH^+) to a beam of protons (H^+) and other particles. The energy of the dissociated protons was modulated by the variable potential of the dissociator, thus providing negative feedback for the homogenizer system.[1]

The water was kept at room temperature (vapor pressure ~20 torr) in a reservoir connected to the dissociator by a gate valve which was normally closed. Through another connection, the vapor flowed from the reservoir through a flow rate meter to the dissociation canal. In normal operation, the flow rate was adjusted to about 100 cc/min. The resulting proton beam current was 30 - 60% of the diatomic beam current. The water vapor was contained in the dissociation canal by the effect of eight cylindrical surfaces maintained at low temperatures by contact with a reservoir of liquid nitrogen. At the normal ESA vacuum of $\sim 5 \times 10^{-6}$ torr and with the normal water vapor flow, the dissociator had a net pumping effect on the ESA vacuum (i.e., opening the gate valve between the ESA and the dissociator improved the ESA vacuum). After several weeks

---

1. One could provide negative feedback either by driving the voltage on the dissociator or by driving the voltage on a plate of the ESA. The ESA used sustains higher electric fields if the magnitudes of the plate voltages are nearly equal. Since the high voltage makes it difficult to drive the plate with the fluctuating signal, the voltage on the dissociator was driven for feedback.

Figure 1. Sectional Views of the Water-Vapor Dissociator.

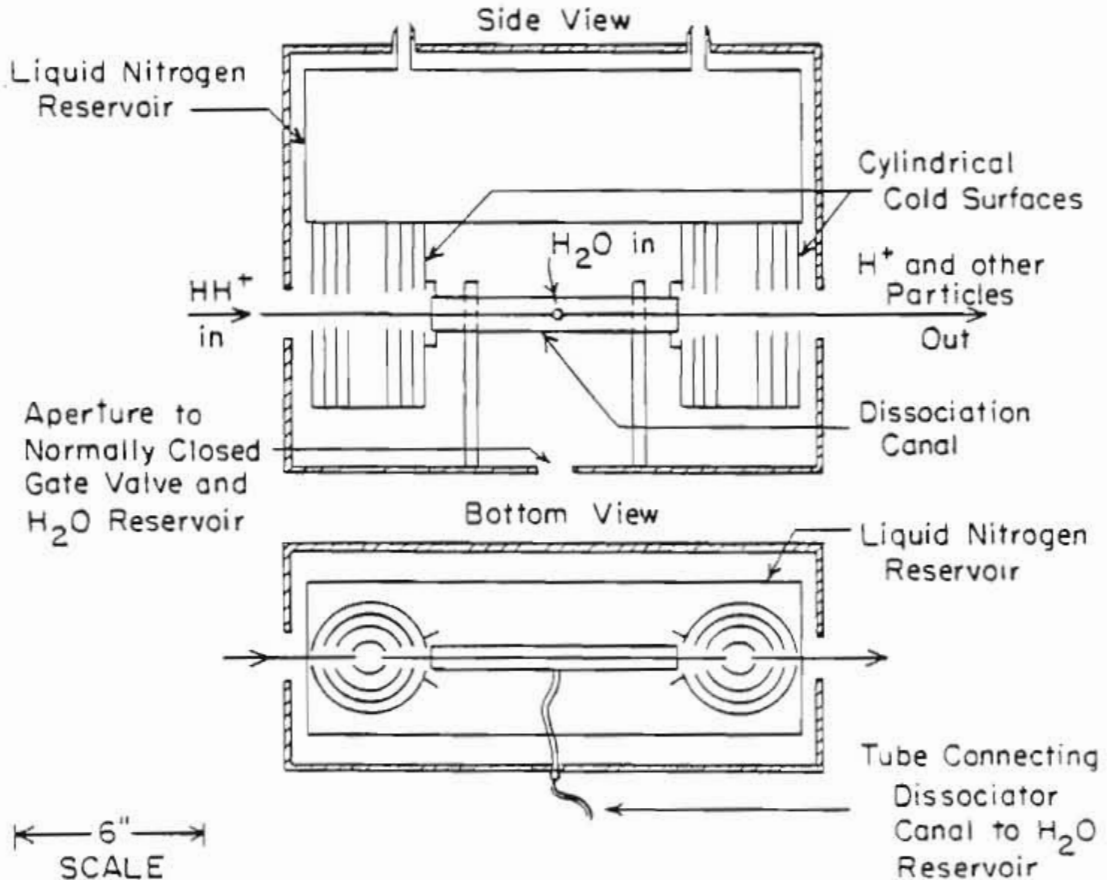
Side View
Liquid Nitrogen Reservoir
Cylindrical Cold Surfaces
H_2O in
H^+ and other Particles
HH^+ in
Out
Aperture to Normally Closed Gate Valve and H_2O Reservoir
Dissociation Canal
Bottom View
Liquid Nitrogen Reservoir
Tube Connecting Dissociator Canal to H_2O Reservoir
6"
SCALE

of operation, the ice which had collected on the cold surfaces was transported back to the water reservoir by isolating the dissociator, warming the nitrogen reservoir, cooling the water reservoir with liquid nitrogen, and then opening the gate valve between the dissociator and the water reservoir.

3. System Description

The components of the modified ESA homogenizer system are shown in figure 2. The HH^+ beam was first used, in conjunction with the analyzing magnet, as a part of a conventional corona control system for the Van de Graaff accelerator. As discussed in section II 4 (see figure 4), the typical energy resolution obtained by this system alone was about 1.6 keV fwhm. After passing through the corona control slit, the HH^+ ions entered the homogenizer system. Here an additional time dependent energy correction was obtained, and the energy resolution was further improved. To aid in the description of the homogenizer system the following definitions are adopted:

T = energy of protons approaching the target,

T_R = energy of protons reacting with the target,

T_M = energy of molecular ions approaching the dissociator,

T_E = energy of protons in the ESA

Figure 2. Block Diagram of the Accelerator-Homogenizer System. (Gain-of-500 amplifiers are shown in detail in figure 6.)

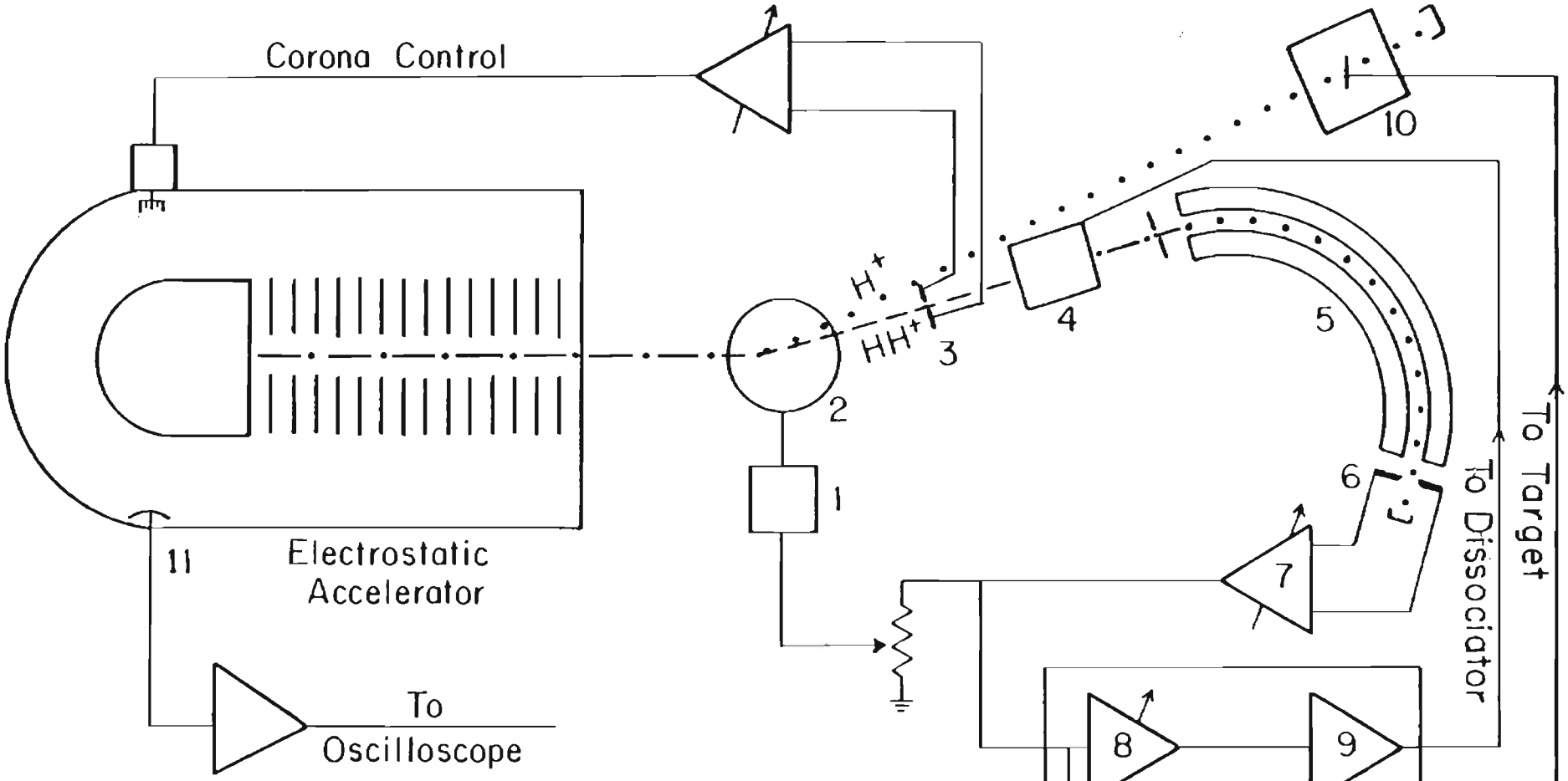

1) Magnet Current Supply
2) Analyzing Magnet
3) Corona Control Slit
4) Water-Vapor Dissociator
5) Electrostatic Analyzer
6) Homogenizer Control Slit
7) Preamplifier (P.A.R. Model 113)
8) Inverter Amplifier
9) Gain-of-500 Amplifier
10) Target Chamber
11) Capacitive Probe

(These energies are obtained by averaging over the kinetic energies of the particles in the beam for a time interval which is short compared to the characteristic fluctuation times of the Van de Graaff voltage (i.e., $\Delta t \ll 1$msec)),

V_D = voltage on the dissociator,

V_T = voltage on the target,

V_S = voltage between electrodes of the homogenizer control slit,

G_p = voltage gain of the preamplifier,

β = voltage gain of the inverter amplifier shown in figure 2,

$G_A = \frac{e}{2}\left(dV_S/dT_E\right)$ = gain of the analyzer,

$G_O = \frac{e}{2}\left(dV_T/dT_E\right)$ =open loop gain of the homogenizer system,

$G_C = e\left(dV_T/dT_M\right)$ = closed loop gain of the homogenizer system.

The dissociator converted the diatomic beam into a proton beam. The protons leave the dissociator with an energy given by[1]

$$T_E = 1/2\left(T_M + eV_D\right) \qquad (1)$$

Since the energy of the diatomic ions was decreased by eV_D

---

1. The energy of the protons between the dissociator and the ESA is not the same as that of the protons inside the ESA (T_E). This difference is due to the non-zero potential along the ideal path through the ESA. Since the difference is small and time independent, it is neglected in the immediate discussion. See the appendix for more details.

as they entered the dissociator, the dissociated protons had an approximate energy of 1/2 (T_M-eV_D) inside the dissociator. The protons then gained an energy eV_D upon leaving the dissociator.

In passing through the ESA, each proton was bent through an arc whose radius of curvature depended on the proton's energy. Two insulated electrodes, forming an image slit, collected the current produced by protons whose energies were either too high or too low to allow them to pass through the slit. The difference between these currents produced a signal which was dependent on the average proton energy. The change in this signal for a change in proton energy is the analyzer gain (G_A). This gain was strongly dependent on the intensity, focus, and energy of the beam. For this reason the analyzer gain fluctuated, and the improved system linearity and gain stabilization provided by negative feedback was required.

The signals from the slit electrodes were subtracted and amplified by the preamplifier shown in figure 2. The output from this preamplifier was sent to a gain-of-500 amplifier which varied the potential of the target. The preamplifier signal was also sent to the inverter amplifier which in turn was connected to another gain-of-500 amplifier. This latter amplifier varied the dissociator potential and thus the energy of the dissociated proton beam (see equation 1).

From the above information and $T = T_M$, one can show that the energy of the protons reacting with the target (T_R) was related to the energy of the protons before experiencing the potential on the target (T) by

$$dT_R / dT = (1 - G_c)$$

For the reaction energy to be constant, the closed loop gain, G_C, must be one. This closed loop gain is related to the other gains in the system by the conventional feedback expression:

$$G_c = \frac{G_o}{1 - \beta G_o}$$

where

$$G_o = 500 G_A G_P$$

In a negative feedback system, linearity and stability are improved as G_o is increased. In this system, maximum values of G_o were limited to 10 - 20 since phase shifts caused oscillation at higher gains. In adjusting the homogenizer system, G_o was maximized and β was adjusted for best reaction energy stabilization. Since G_o is not infinite, fixing β at the ideal value of -1 would have left the reaction energy fluctuating by an amount equal to 5 - 10% of the original energy fluctuations. With the above values for G_o, equation 3 and the null condition ($G_c = 1$) yield $\beta = -.90$ to $-.95$ (which agrees with the value measured electronically after adjusting the system as described

above).

To reduce efforts in data taking, and to stabilize the system further, a signal from the preamplifier was fed back to the analyzing magnet current supply (see figure 2). This signal caused the accelerator energy to track slow components of the homogenizer signal (only variations with characteristic times greater than ~0.5 sec. were tracked due to the large inductances involved). With this feature, manual adjustment of the magnet current supply was performed after 20 - 40 keV of data had been measured, rather than after each step of 100 - 400 eV as was previously required.

4. Performance

Potential fluctuations on the high voltage terminal of the accelerator were monitored with a capacitance probe as shown in figure 2. With a high impedance bridging amplifier, the frequency response of the monitoring system was excellent: even the low frequency component (~3Hz) of the fluctuations was reproduced. Figure 3 is from a photograph of an oscilloscope screen which simultaneously displayed the terminal voltage fluctuations (upper trace) and the target voltage fluctuations (lower trace). Since the resolution was substantially improved by the correction voltage applied to the target, and since the target signal and terminal signal tracked one another, it appears that the large beam energy spread without homogenizer was caused

Figure 3. Terminal Voltage and Target Voltage Fluctuations Displayed Simultaneously on an Oscilloscope. Note that although the coupling to the terminal is capacitive, the low frequency component still tracks well.

Figure 4. Typical Beam Energy Distribution Caused by Terminal Voltage Fluctuations on the 4 MV Van de Graaff (note the asymmetry).

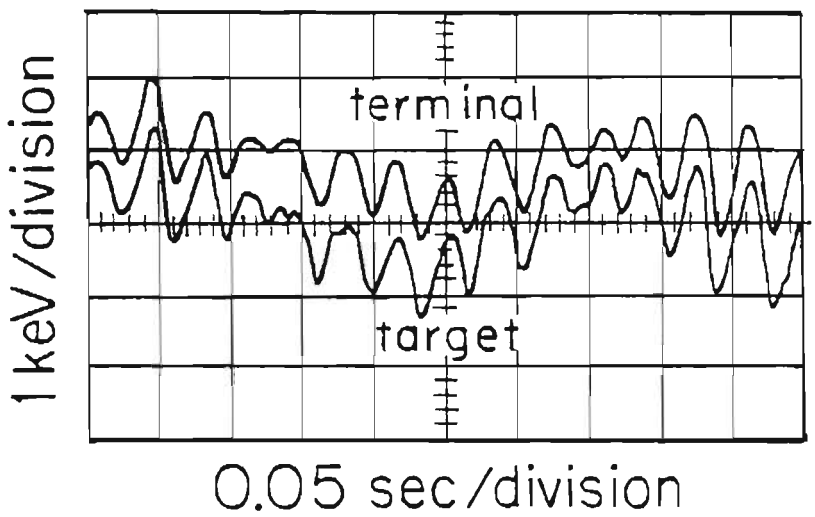
terminal
target
1 keV/division
0.05 sec/division

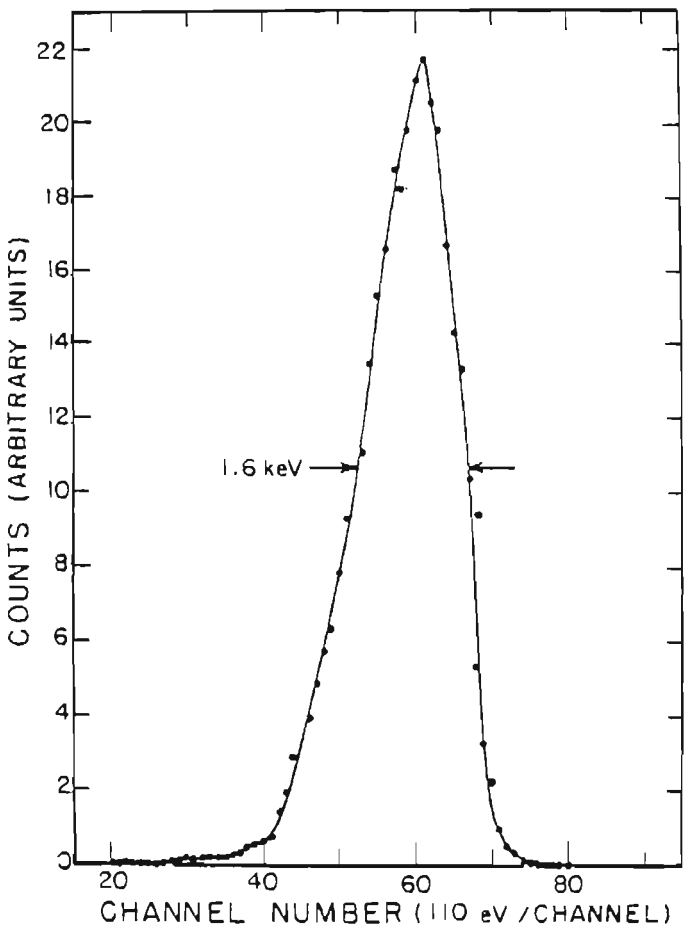
1.6 keV
COUNTS (ARBITRARY UNITS)
CHANNEL NUMBER (110 eV/CHANNEL)
0
2
4
6
8
10
12
14
16
18
20
22
20
40
60
80

principally by terminal fluctuations. Observing terminal voltage fluctuations is of considerable aid in the initial tuning of the accelerator and the corona control system; these adjustments can be performed without the homogenizer system. Also, during the experiment, continuous monitoring of the relative amplitudes and shapes of the two independently measured signals (as shown in figure 3) provided an early indication of difficulties such as detuning of the accelerator or gain changes in the ESA or homogenizer.

The bottom trace in figure 3 shows a typical target voltage signal. To obtain a quantitative estimate of the effect of the time dependent beam energy fluctuations upon measured energy resolution, the target signal was chopped into equal time segments and pulse height analyzed. The result, shown in figure 4, indicates that for measurements without the homogenizer system, time dependent fluctuations in the beam energy would contribute 1.6 keV fwhm to the observed experimental resolution. Of course, the total experimental resolution contains time uncorrelated components due to Doppler broading and straggling. With solid targets, this time uncorrelated energy spread ranges from 100-300 eV depending upon target thickness and beam energy. Since the observed total experimental resolution with the homogenizer system (shown in figure 5) is $\sim$300 eV, one concludes that residual time dependent beam energy fluctuations are essentially eliminated.

Figure 5 shows elastic scattering data obtained at 160° for protons on ^{58}Ni. The solid line represents a fit obtained with the R-matrix code Multi (Sellin 1969) and a resolution function[1] of 290 eV fwhm, a natural width of 9 eV, and a $J^{\pi} = 5/2^{-}$. To indicate the value of improved resolution, the cross section was calculated with the same resonance parameters and a resolution of 1.6 keV (to simulate the system operation without the homogenizer). The result is the dashed line in figure 5; with the statistics normally obtained in these experiments, one could scarcely recognize the resonance without the homogenizer, much less identify its ℓ-value.

5. Energy Measurements

For a slow moving particle to follow an ideal path through an ESA whose plate separation is much smaller than its radius of curvature, Newton's second law of motion requires that

$$eE = eV/d = \frac{mv^2}{r} = \frac{2T}{r} \qquad (1)$$

---

1. Straggling in thin targets causes an asymmetry in the resolution function (Ophel and Kerr 1975). Figure 4 illustrates that the time dependent energy fluctuations also produce an asymmetry. The resolution function used in the calculation was constructed with convenient functions and adjusted to fit the data from small inelastic (p,p') resonances. It is asymmetric with a low energy tail that is about 10% as high as the peak at an energy twice the fwhm below the energy of the peak.

Figure 5. An $\ell = 3$ Resonance of Width $\Gamma = 9$ eV Observed in ^{59}Cu. The solid line represents a fit; an asymmetric resolution function of 290 eV fwhm was used in the calculation. The dashed line was calculated with the same resonance parameters and a resolution function of 1.6 keV fwhm.

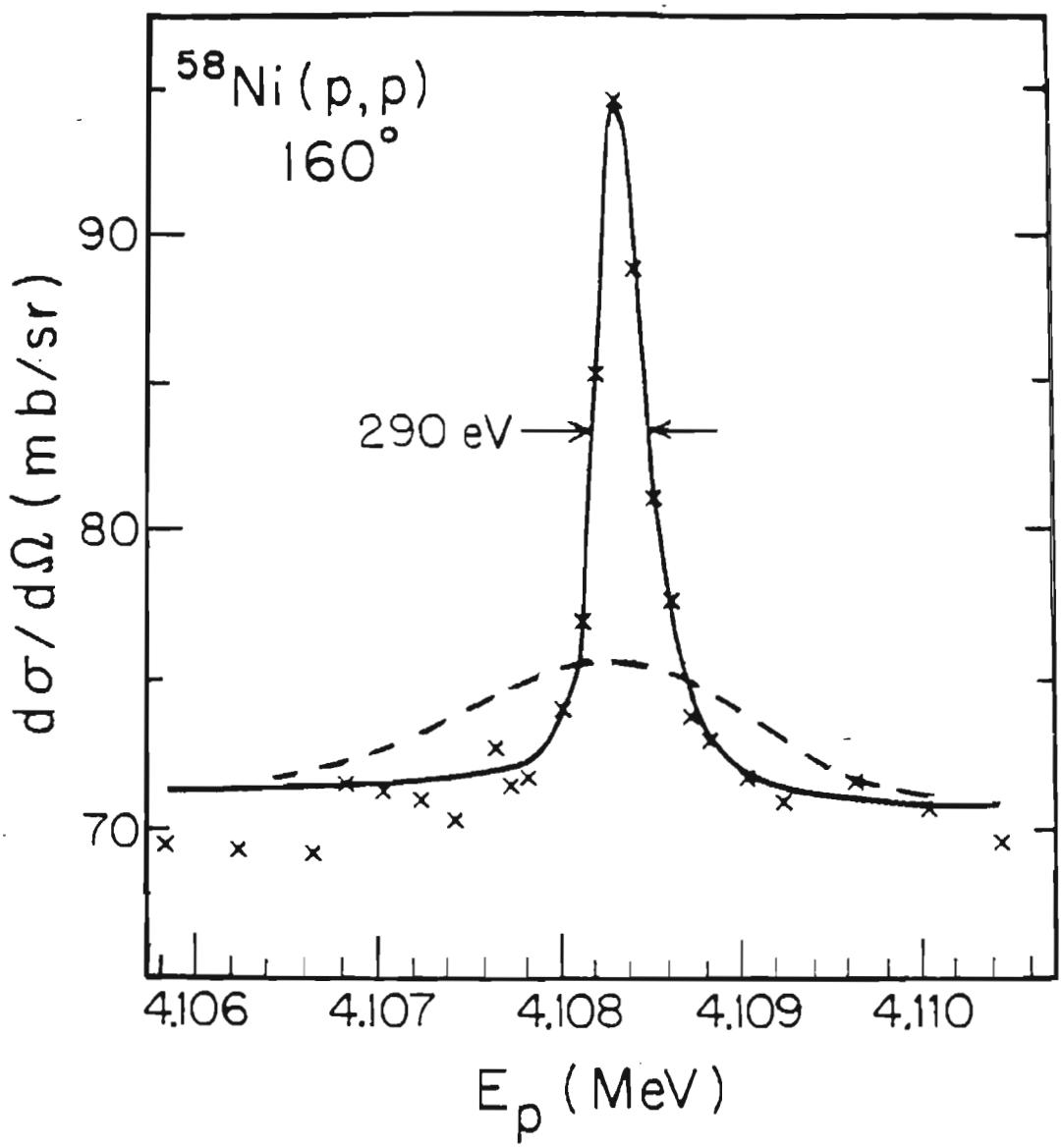
58Ni (p, p)
160°
290 eV
dσ/dΩ (mb/sr)
90
80
70
4.106
4.107
4.108
4.109
4.110
Ep (MeV)

where

e = proton charge,

V = voltage between the plates of the ESA,

d = ESA plate separation,

T = kinetic energy of the particle,

r = radius of curvature of the ESA.

If r and d are known, then the energy of the particles is obtained by measuring the plate voltage which is required for the particles to pass through the ESA. Figure 6 shows schematically the voltage dividers and differential voltmeter (DVM) which were used to measure this voltage. (Notice that any instabilities in the plate power supplies are compensated for by applying the off null signal, "recorder output", from the DVM to the dissociator with the proper gain.)

Equation 1 was tested by calibrating the Van de Graaff generating voltmeter, accurately measuring the analyzer voltage (with magnitudes of plate voltages equal), and observing the generating voltmeter reading when the molecular (undissociated) beam passed through the ESA. The value of the quantity r/d was found to be 139. The geometrical parameters r and d are known to be 39.99 inches and 0.305 inches respectively. This yields r/d = 131 which is in fair agreement with that obtained with the elementary equation.

The energy calibration was performed with the $^{13}C(p,n)$ threshold reaction. Adoption of the threshold of

Figure 6. Schematic Diagram of Circuits Associated With the Electrostatic Analyzer (the differential voltmeter, the 10 KV Fluke voltage supply, and both 100K helipots are located in the control room).

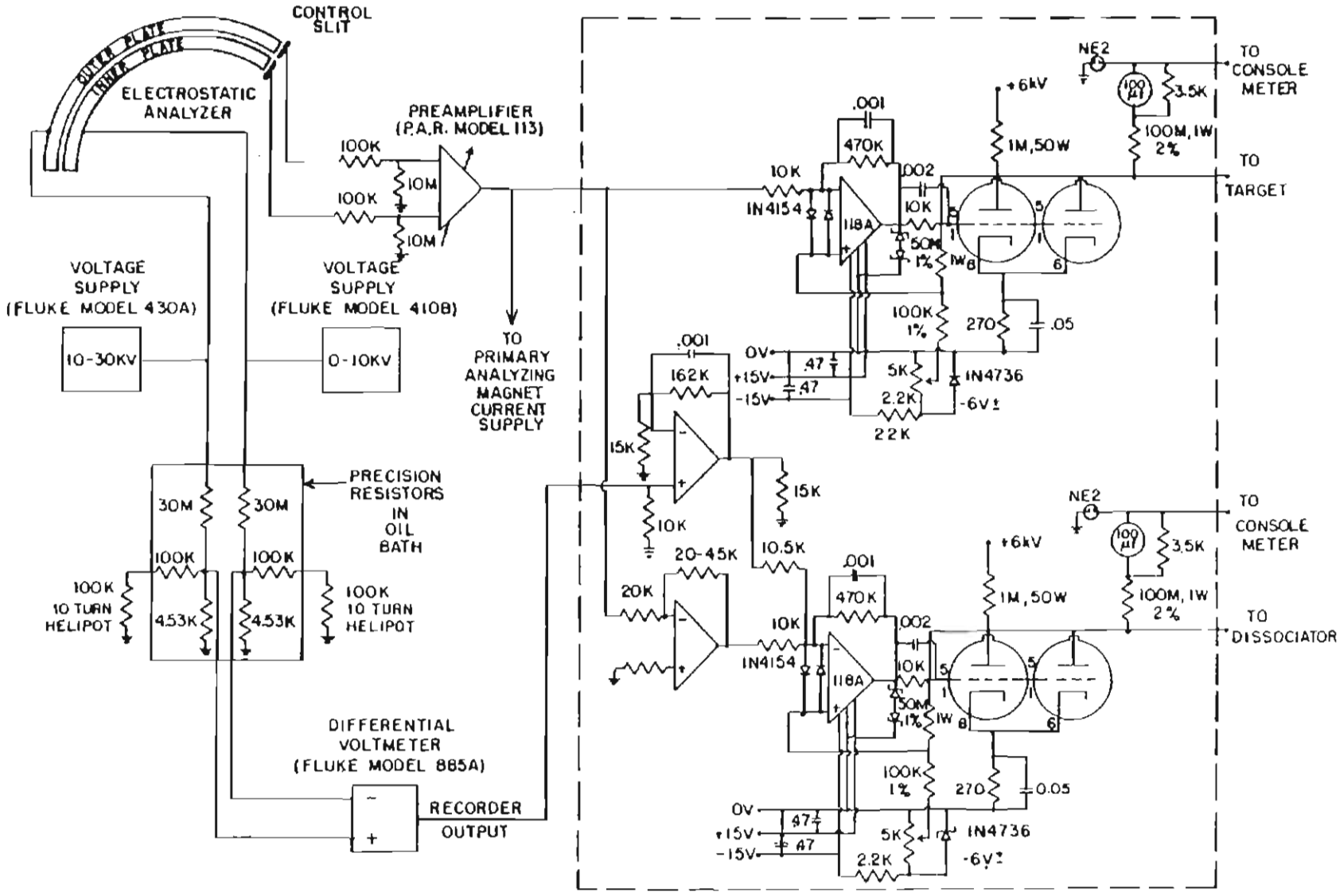
CONTROL SLIT
OUTER PLATE
INNER PLATE
ELECTROSTATIC ANALYZER
PREAMPLIFIER (P.A.R. MODEL 113)
100K
10M
100K
10M
VOLTAGE SUPPLY (FLUKE MODEL 430A)
10-30KV
VOLTAGE SUPPLY (FLUKE MODEL 410B)
0-10KV
TO PRIMARY ANALYZING MAGNET CURRENT SUPPLY
30M
30M
PRECISION RESISTORS IN OIL BATH
100K
100K
100K 10 TURN HELIPOT
4.53K
4.53K
100K 10 TURN HELIPOT
DIFFERENTIAL VOLTMETER (FLUKE MODEL 885A)
RECORDER OUTPUT
.001
470K
10K
IN4154
118A
.002
10K
50M 1%
1W
1M, 50W
+6kV
NE2
100 μA
3.5K
100M, 1W 2%
TO CONSOLE METER
TO TARGET
100K 1%
270
.05
.001
162K
0V
+15V
-15V
.47
.47
5K
2.2K
22K
IN4736
-6V±
15K
10K
15K
10.5K
20-45K
20K
.001
470K
10K
IN4154
118A
.002
10K
50M 1%
1W
1M, 50W
+6kV
NE2
100 μA
3.5K
100M, 1W 2%
TO CONSOLE METER
TO DISSOCIATOR
100K 1%
270
0.05
0V
+15V
-15V
.47
.47
5K
2.2K
IN4736
-6V±

this reaction as a standard removed many problems associated with absolute energy measurements. In chapter III and in the appendix, errors in the energies measured with this system are discussed more fully.

In early use of the dissociator-homogenizer, very slow 10 - 15 keV energy drifts were observed. These drifts were caused by the neutral and HH^+ beam components entering the ESA and heating the outer plate. A small-angle-deflecting magnet was placed between the dissociator and the ESA to remove these unwanted components from the beam. After this modification, energy reproducibility within ± 600 eV was obtained.

B. Data Accumulation

1. Beam Preparation

In these experiments the radio frequency ion source in the Duke 4 MV Van de Graaff accelerator was used to produce a beam of hydrogen ions. As shown in figure 1, the primary analyzing magnet separated the monatomic ions (protons) from the diatomic ions (HH^+). The proton beam was used to produce the reactions investigated. As discussed in the previous section, the HH^+ beam was used to provide signals to correct for energy fluctuations. The beam focusing and steering facilities of the accelerator were

used to maximize the H^+ beam current passing through the corona control slit. This procedure also fixed the path of the proton beam. The magnetic deflectors shown in figure 7 were adjusted to provide optimum proton beam alignment and focus at the target.

The target chamber used in these experiments is described by D. G. Gerke (1963); this chamber is shown schematically in figure 7 a. The original intense beam collimator was used except for some details shown in figure 7 b. The lavite shaft, the aluminum shaft, and the three tantalum collimating disks were fabricated on a lathe and then press fitted together to insure proper alignment of the three holes. Scattering from the last collimating disk produced a background of low energy protons which makes observation of the (p,p') reaction difficult. This scattering was minimized by the middle collimating disk whose aperture was small enough to shield the last collimating disk from the beam. To aid in minimizing this scattered current, the last disk was electrically insulated and the current striking it was read externally. When the beam was aligned and focused, currents of less than 10^{-2} μA were observed on this last disk (typical currents throughout the system are listed in table 2).

Figure 7. Target Chamber Arrangement and Intense Beam Collimator.

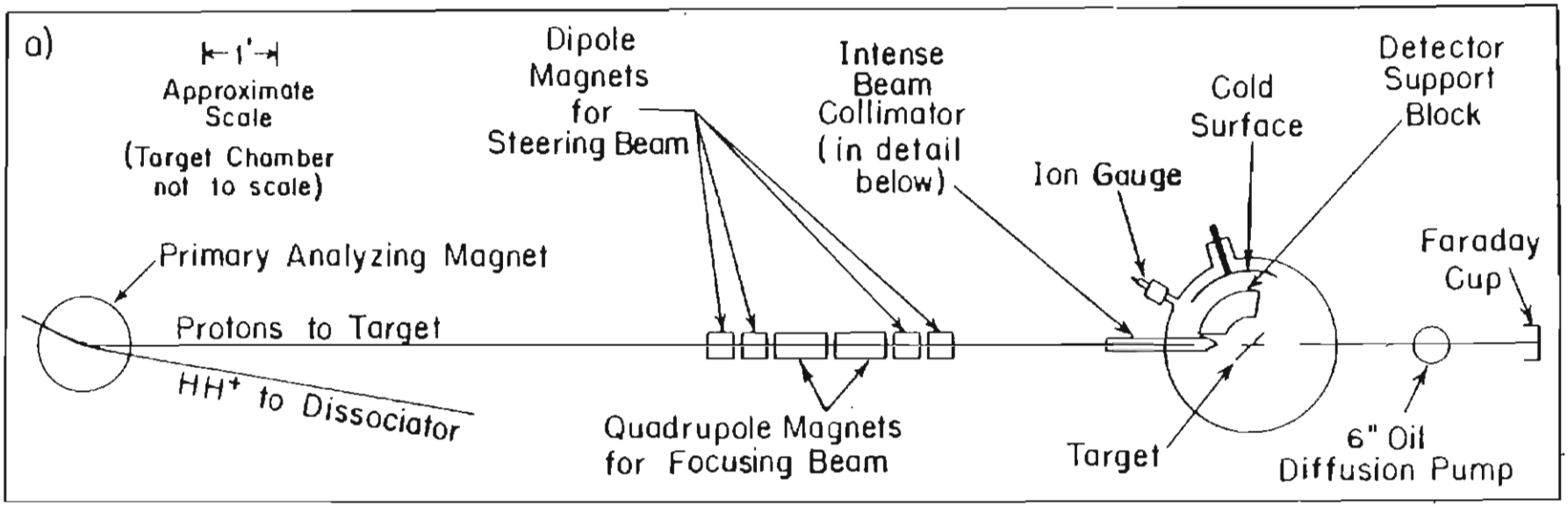
a)
1'
Approximate Scale
(Target Chamber not to scale)
Dipole Magnets for Steering Beam
Intense Beam Collimator (in detail below)
Cold Surface
Detector Support Block
Ion Gauge
Faraday Cup
Primary Analyzing Magnet
Protons to Target
HH+ to Dissociator
Quadrupole Magnets for Focusing Beam
Target
6" Oil Diffusion Pump

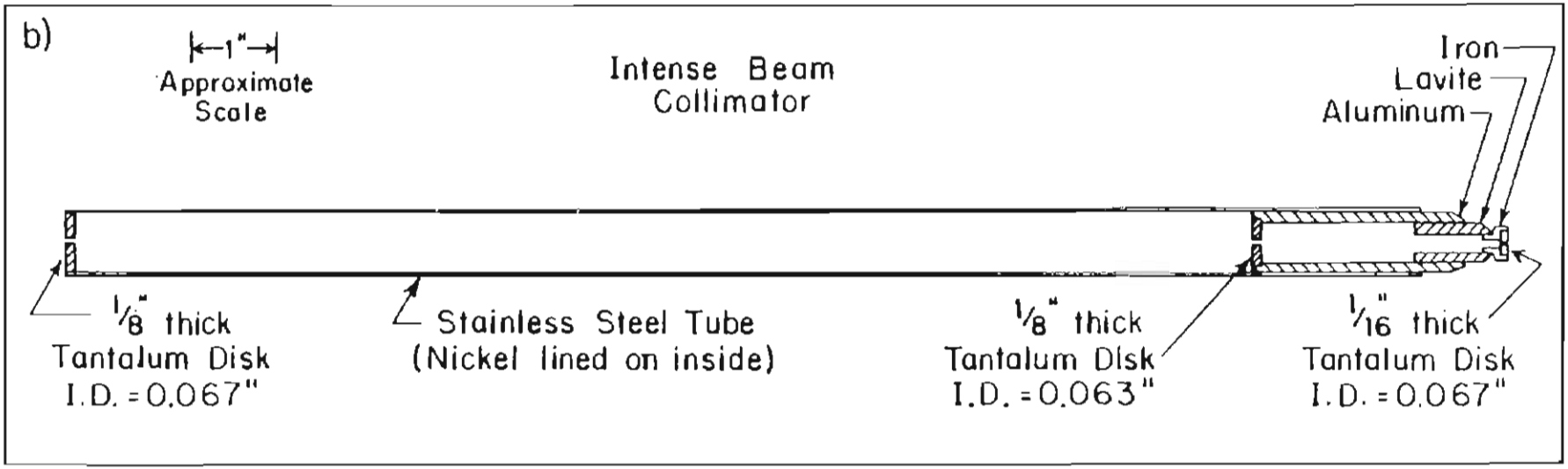
b)
1"
Approximate Scale
Intense Beam Collimator
Iron
Lavite
Aluminum
1/8" thick Tantalum Disk I.D. = 0.067"
Stainless Steel Tube (Nickel lined on inside)
1/8" thick Tantalum Disk I.D. = 0.063"
1/16" thick Tantalum Disk I.D. = 0.067"

2. Targets

Targets were prepared from ferrous oxide and from nickel powders obtained from Oak Ridge National Laboratory. The specific enrichments of the isotopes are listed in table 1.

Isotopic thicknesses of 1 - 4 μgm/cm^2 were evaporated onto 5 μgm/cm^2 self-supporting carbon backings. The nickel isotopes were evaporated with Al_2O_3 covered molybdenum boats. The iron was reduced and evaporated with a deep carbon crucible (this avoided the tungsten contaminant observed by Lindstrom, 1970). Typical proton spectra are shown in figure 8. Notice that the elastic and inelastic proton groups of interest are well separated from the other proton groups.

Doppler broadening is the limiting factor for the observed energy resolution in these experiments. Reducing the total target thickness reduces the beam spot temperature and improves the energy resolution. The ultimate lifetime of a target is limited by impurity buildup on the target. The rate of impurity buildup is a strong function of the vacuum; with a 6 inch oil diffusion pump and a surface in the target chamber cooled by liquid nitrogen, a vacuum less than 5 x 10^{-6} torr was maintained.

TABLE 1.

TARGET COMPOSITION

Isotope	% Enrichment	Contaminant	%
^{54}Fe	96.81	^{56}Fe	3.04
(Fe_2O_3 powder)		^{57}Fe	0.12
		^{58}Fe	0.03
^{58}Ni	99.89	^{60}Ni	0.11
(nickel powder)		^{61}Ni	<0.01
		^{62}Ni	<0.01
		^{64}Ni	<0.01
^{60}Ni	99.79	^{58}Ni	0.21
(nickel powder)		^{61}Ni	<0.05
		^{62}Ni	<0.05
		^{64}Ni	<0.05

Figure 8. Typical Spectra for the Three Isotopes Studied.

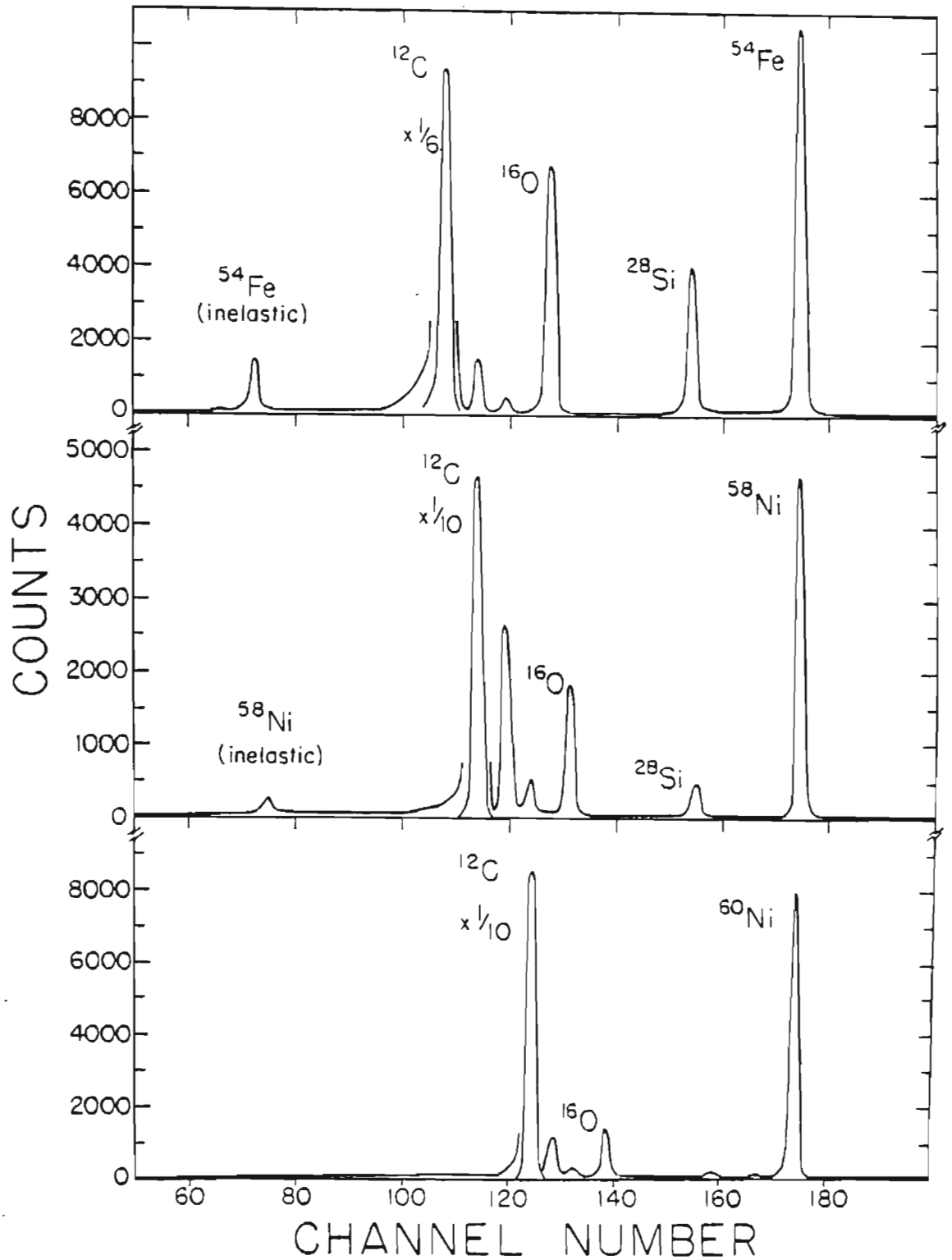
COUNTS
CHANNEL NUMBER
^{12}C
x 1/6
^{16}O
^{28}Si
^{54}Fe
^{54}Fe
(inelastic)
^{12}C
x 1/10
^{58}Ni
^{16}O
^{28}Si
^{58}Ni
(inelastic)
^{12}C
x 1/10
^{60}Ni
^{16}O
0
2000
4000
6000
8000
1000
3000
5000
60
80
100
120
140
160
180

3. Detection

Scattered protons were observed with Ortec silicon surface barrier detectors (active area of 50 mm^2 and a depletion depth of 200 - 300 microns). The detector resolution was 15 - 20 keV. The detectors were mounted in one unit with their relative orientation fixed (see figure 9) to minimize alignment problems and to make possible the use of the existing rotating table inside the target chamber. The detectors were located at laboratory angles of 90°, 105°, 122°, and 160° with respect to the beam direction. The target-detector distances and the collimator geometries were adjusted to maximize the solid angle for reactions near the target spot while minimizing the solid angle for reactions outside this region. The relative solid angles between the different detectors were adjusted so that equal counting rates were observed from the Coulomb scattering background (i.e., the solid angles vary as $\sin^{-4}(\theta/2)$). In this experiment, the observed counting rates were small enough that the rate of occurrence of overlapping pulses was negligible. In retrospect, it appears that adjusting the solid angles to maintain equal counting rates was not the best procedure. If each solid angle had been maximized (maintaining sufficient collimation), higher counting rates could have been obtained at the forward angles and thus

Figure 9. Detector Mount and Collimation.

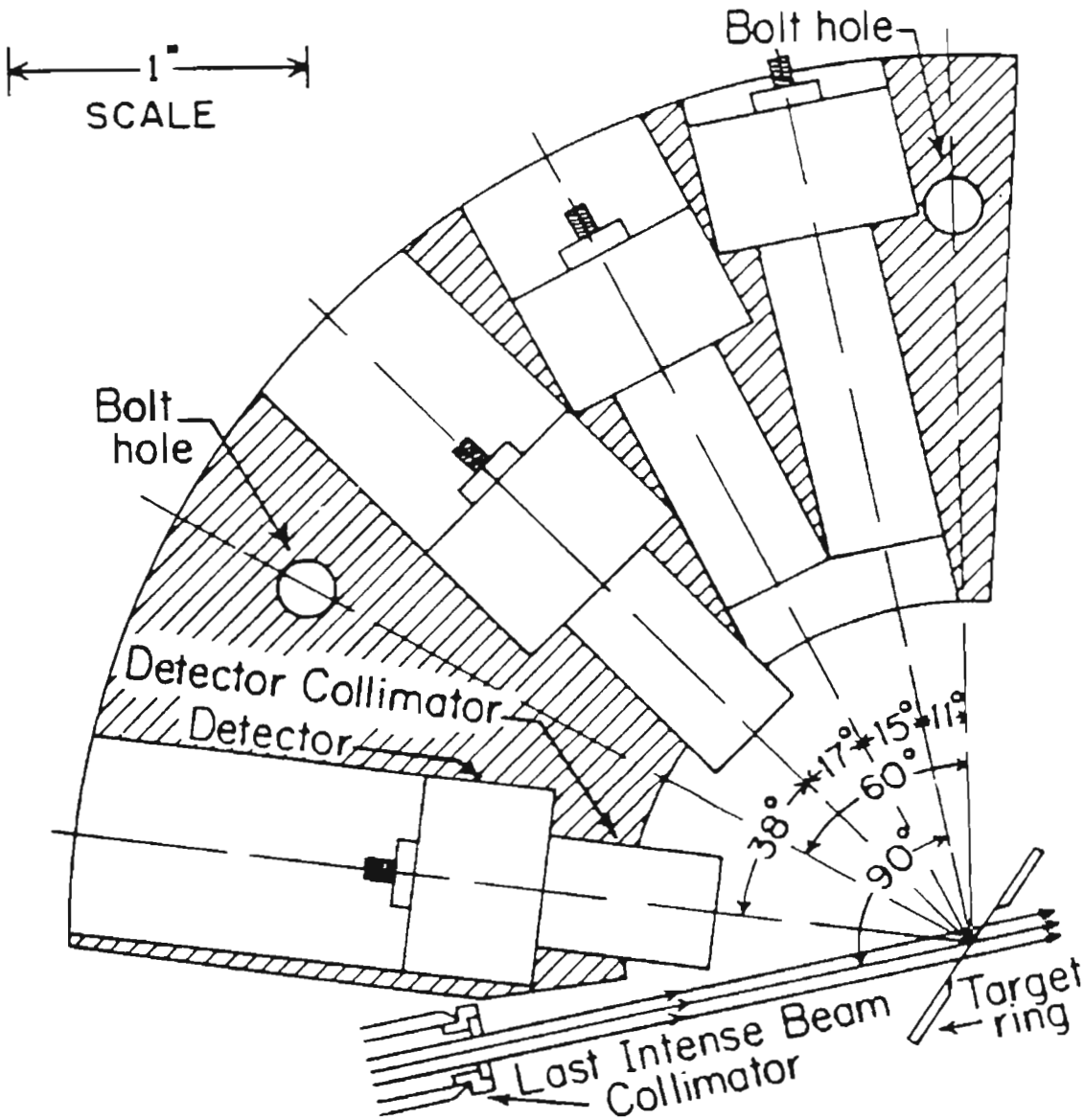

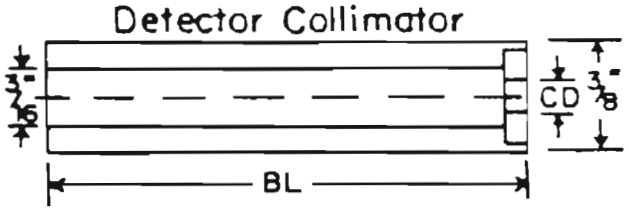

Back Angle	BL	CD	Solid Angle(sr)
90°	1.05	0.055	0.0013
105°	0.81	0.070	0.0021
122°	0.68	0.064	0.0031
160°	0.57	0.067	0.0050

better statistics would have been obtained at these angles. This would have aided in the identification of the spin of small p- and d-wave resonances.

4. Electronics

During the experiment, currents were monitored at various locations throughout the system. Some typical currents are listed in table 2. The primary proton beam current (read on the Faraday cup--see figure 7) was integrated to 100 - 150 μC. Scalers counted the pulses from the elastic proton group of interest at four angles while three other scalers counted the pulses from the inelastic proton group. The scaler's contents were printed on paper and punched on paper tape with a teletype. Figure 10 shows a block diagram of the electronics connecting the detectors to the scalers. At 90°, 122°, and 160°, the biased amplifiers fed two single channel analyzers (SCA). One SCA was adjusted for the elastic peak while the other SCA was adjusted for the inelastic peak. The pulser and 400 channel analyzer were used to maintain the proper adjustment of the gains, bias level, and windows.

5. Procedure

The differential cross sections were measured in

TABLE 2.

TYPICAL CURRENTS

Accelerator	Current in μA
total beam stop (ahead of magnet)	30.0
corona control slit (both electrodes)	2.0
corona current	60.0
Primary Proton Beam	
beam stop	5.5
last collimating disk	0.01
Faraday cup	5.0
Control (HH^+) Beam	
beam stop	4.5
nonstripped beam (measured before ESA input slit)	2.0
ESA input slit (both electrodes)	2.0
H^+ out of ESA	0.05

Figure 10. Block Diagram of the Charged Particle Counting System.

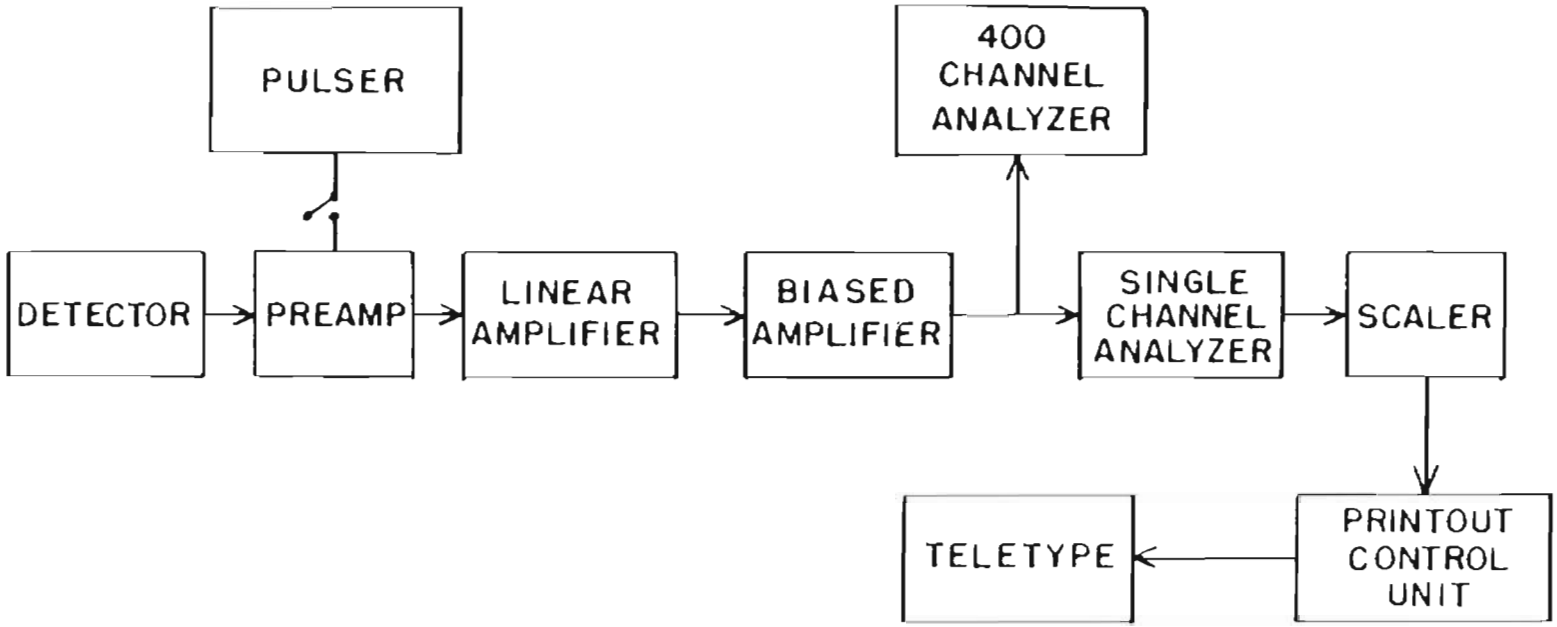
PULSER
400 CHANNEL ANALYZER
DETECTOR
PREAMP
LINEAR AMPLIFIER
BIASED AMPLIFIER
SINGLE CHANNEL ANALYZER
SCALER
TELETYPE
PRINTOUT CONTROL UNIT

energy intervals of 5 – 100 keV with each interval taken in 100 - 500 eV steps. The measuring time for each data point was about 30 seconds. Data were recorded on paper tape as a set of eight numbers: energy, number of elastically scattered protons at four angles, and number of inelastically scattered protons at three angles. With these counting times, the Coulomb background yielded counts of 5,000 - 10,000 for elastic protons corresponding to statistical fluctuations of 1 - 1.4%. The background observed in the inelastic scattering was dependent on the beam focus and steering. Typical values for this background are 500, 300, and 100 counts for 160°, 122°, and 90°, respectively, corresponding to a differential cross section of 5 – 10 mb/sr.

CHAPTER III

PRELIMINARY ANALYSIS

A. Introduction

In the analysis of these data, a set of resonance parameters is first extracted from the measured cross sections. In this chapter the details of this phase of the analysis are discussed, and the experimental data and resonance parameters are presented.

The original data were printed on paper and punched on paper tape. Each data run overlapped with the previous one, and a resonance was always included in the overlap region. It was thus possible to obtain accurate (±100 eV) values of the energy shifts from run to run. With the TUNL Alpha computer, the paper tapes were read, energies were shifted, and cards were punched, thus producing continuous excitation functions for each of the three isotopes studied. The data were edited to eliminate overlapping points. Again

with the Alpha computer, tentative resonance parameters were obtained for most of the data by analysis with the single channel R-matrix code Multeye (Lindstrom 1969). This procedure had numerous advantages: ease of operation, faster turn-around time, and visual display. Starting from these tentative resonance parameters, the data were then fit with the aid of the TUCC IBM 370/165 computer and the multichannel R-matrix code Multi (Sellin 1969). The final resonance parameters (after the corrections described in section III D) are presented in section III E. The normalized data and calculated fits were recorded on cards during the final fitting process; these cards were then used to generate the plots also shown in section III E. Following a brief résumé of R-matrix theory in the next section, the details of the fitting process are discussed in section III C.

B. R-Matrix Theory

One of the first models invoked to explain nucleon-nucleus scattering was the "extreme independent-particle" model (e.g., Bethe 1935). In this model it is assumed that projectiles are scattered by a potential well; the model predicts resonances which are broad and spaced far apart. The discovery of narrow, closely-spaced resonances in 1935 (e.g., protons: Hafstad and Tuve 1935, neutrons: Moon and

Tillman 1935) contradicted the predictions of the extreme independent-particle model.

In 1936 Bohr proposed that the sharp, closely-spaced resonances were due to long-lived virtual states of the nucleus composed of the target plus the projectile. Bohr suggested that the strength of the force between two nucleons was so strong that when a projectile entered the nucleus it rapidly shared its energy with all of the nucleons in the nucleus. Conversely, for a nucleon to subsequently leave the nucleus, the nucleon had to regain this energy from several nucleons. Since this latter process is improbable the "compound" nucleus stayed together for a relatively long time.

At the time when the Bohr Hypothesis was presented, there was no theoretical formalism which could easily be adopted to describe the compound nucleus. The notion of the projectile strongly interacting with each nucleon in the nucleus prohibited a straightforward analysis in terms of potentials.

With nonrelativistic quantum mechanics, Kapur and Peierls (1938) provided the first theory of nuclear reactions which both explained the resonance structure and appeared consistent with what was then known about nuclear forces. They reasoned that if a resonance were narrow then the life of the compound state would be long and the wave function inside the nucleus would not change appreciably if

Brändle et al. quote (see table 14) are about half as large as those obtained in the present work; this discrepency is not understood.

The value $S_p = 0.004$ obtained by Arai et al. is a factor of ten smaller than the present value. They misassigned the $3/2^-$ resonance at 3.933 MeV proton energy as the IAR; the better choice is the resonance (at $E_p = 4.002$ MeV) which is just above the highest energy measured by Arai et al. Comparison of the Coulomb energies also supports the present assignment (see table 10).

Inelastic spectroscopic factors were obtained in the same manner as elastic spectroscopic factors. The values for Γ_{sp} were calculated as discussed earlier and are listed in table 12. The inelastic spectroscopic factors are listed in table 15 where Γ_i is the total inelastic decay width of the i^{th} fragment of the IAR.

B. Statistical Properties

1. Introduction

The nuclei ^{55}Co and ^{59}Cu are so near shell closures that the properties of states of excitation $\sim$8 MeV may not be adequately described by the usual statistical models. Standard statistical analyses were performed and in a number

the nucleus were prevented from decaying by imposing a boundary condition at some radius "outside" of the nucleus. Thus by studying the virtual or resonant states of the actual nucleus, one could gain information about the discrete states of the "boxed in" nucleus.

With a similar approach, Wigner and Eisenbud (1947) developed R-matrix theory. A classic review of this theory was presented by Lane and Thomas in 1958. In the following, a few of the more important aspects of the theory will be presented.

The major assumptions of R-matrix theory are:

(i) nonrelativistic quantum mechanics applies,

(ii) breakup into only two product nuclei is considered,

(iii) for each pair of product nuclei there exists a distance of separation beyond which no polarizing force exists.

The generality of R-matrix theory means that it could be employed to describe most reactions. In practice, the R-matrix formalism is extremely well suited for the analysis of isolated resonances.

Excitation functions can be properly fitted for several exit channels even when resonances are interfering with one another. However, in the fitting process the values of a set of "resonance parameters" must be assumed; these resonance parameters are identified as the properties

of the states of the compound nucleus. Thus by fitting the scattering data with the R-matrix expressions, one obtains information such as the spin (total angular momentum), parity, resonance energy, and reduced widths of a compound state.

The reduced-width amplitude for a given breakup into two product nuclei (channel) is

$$\gamma_{\lambda c} = [\hbar^2/(2 M_c a_c)]^{1/2} \int_{a_c} \Phi_\lambda \psi_\lambda \, dS$$

where

c = the channel,

M_c = the reduced mass $= \frac{M_1 M_2}{M_1 + M_2}$,

a_c = the separation beyond which the nuclei experience no further polarizing force,

ψ_λ = the λ^{th} eigenstate of the nucleus with artificial boundary conditions,

Φ_c = the angular component of the part of the wave function corresponding to the channel c.

The reduced width is the square of the magnitude of the wave function at the surface for channel c and level λ.

The partial width, $\Gamma_{\lambda c}$, of the resonance as observed in a particular channel in an experiment is dependent on both the reduced width, $\gamma^2_{\lambda c}$, and the pentrability, P_c. The penetrability is given by

$$P_c = k_c / [F_l^2(k_c a_c) + G_l^2(k_c a_c)],$$

where

$$k_c = \sqrt{2 M_c E_c}/\hbar \quad ,$$

E_c = kinetic energy of nuclei in channel c,

F_ℓ , G_ℓ = Coulomb wave functions.

For isolated resonances the partial laboratory width is given by

$$\Gamma_{\lambda c} = 2 P_c \gamma^2_{\lambda c} ;$$

and the total laboratory width of the resonance is

$$\Gamma_\lambda = \Sigma_c \Gamma_{\lambda c} .$$

C. Fitting Procedures

A set of resonance parameters was extracted from the data with the aid of the computer code Multi (Sellin 1969). This code uses the multi-level, multi-channel equations of R-matrix theory (presented by the review article of Lane and Thomas (1958)). The output from Multi includes plots of the calculated excitation functions (cross sections as a function of energy) superimposed on the experimental data. One then varies the parameters manually and reruns the program until a satisfactory visual fit is obtained.

Only the elastic and inelastic channels were considered in the analysis. The (p,α) and (p,γ) channels were open but were neglected: alpha decay is severely inhibited by the very low penetrability; and capture widths are normally very small compared to particle widths.

In these calculations a channel radius of 1.25 x $(A_1^{1/3} + A_2^{1/3})$ fm[1] was assumed, and hard sphere potential phase shifts up to $\ell = 4$ were included. The channel boundary values were chosen equal to the shift function separately for each resonance. The calculated excitation functions were averaged with an asymmetric "resolution function" (see footnote in section II A 4). The resulting averaged excitation functions were then compared with the experimental results. Extremes of the fwhm resolution (Γ_S) ranged from 290 to 500 eV with about 80% of the data in the range 330 to 350 eV. The experimental resolution was determined by simultaneously varying Γ_p (or $\Gamma_{p'}$) and Γ_S for a resonance with $\Gamma_p \ll \Gamma_S$ until the best fit was obtained.

The resonance description includes both discrete and continuous variables for each open channel. For the elastic channel, the discrete variables are the spin and parity of the compound state. There are several inelastic decay channels. Each channel is characterized by channel spin 3/2 or 5/2 (since the inelastic decay leaves the target in a 2^+ state) and by exit orbital angular momentum. Angular momentum and parity conservation, combined with penetrability considerations limit the possible inelastic channels to those listed in table 3. The continuous variables are the resonance energy and a width for each channel (Γ_c).

---

1. A_1, A_2 are the proton mass and target mass (in AMU).

TABLE 3.

ALLOWED INELASTIC EXIT CHANNELS[1]

Initial State J^π	Out-going ℓ'-value ℓ'	Exit Channel Spin s'
$1/2^+$	2	3/2, 5/2
$1/2^-$	1	3/2
$3/2^-$	1	3/2, 5/2
$3/2^+$	0	3/2
	2	3/2, 5/2
$5/2^+$	0	5/2
	2	3/2, 5/2
$5/2^-$	1	3/2, 5/2
$7/2^-$	1	5/2
$7/2^+$	2	3/2, 5/2
$9/2^+$	2	5/2

1. The inelastic decay is from an initial state to a 2^+ final state; $\ell'=3$ and higher ℓ' values are neglected.

Identification of the spin and parity of the compound state is primarily determined from the shape of the the elastic excitation functions. Figures 11 and 12 show typical resonance shapes observed in the present experiment. In principle, one can distinguish the spin and parity (at least through $9/2^+$) simply by a shape analysis at 160°. For larger resonances this can be done except for the pairs $(1/2^+,3/2^-)$, $(5/2^-,7/2^-)$, and $(7/2^+,9/2^+)$. Notice that at 90° the positive parity states show a dip and the negative parity states show a rise. This additional information enables one to distinguish between the $(1/2^+,3/2^-)$ pair. For smaller resonances, statistical fluctuations and experimental resolution make a shape analysis at 160° less reliable[1]. In these cases, the 90° data is especially useful: the 90° data combined with the 160° data almost always provide a determination of the ℓ-value.

The excitation functions at 105° and 122° were measured to help to determine spins (J). These angles were chosen in the following manner. The cross section for a small (60 eV) $1/2^-$ resonance was calculated at 160°. The cross section for a $3/2^-$ resonance was then calculated at 160° and the resonance parameters adjusted to make the excitation function coincide as closely as possible with that of the $1/2^-$ resonance. Cross sections were then

---

1. An asymmetric experimental resolution distorts the shape of the resonance. See the footnote in section II A 4.

Figure 11. Typical Calculated Resonance Shapes in Proton Elastic Scattering. The spin, parity, and elastic width used to calculate each resonance shape are listed above the 160° data. An asymmetric resolution function of width 330 eV was used in the calculation.

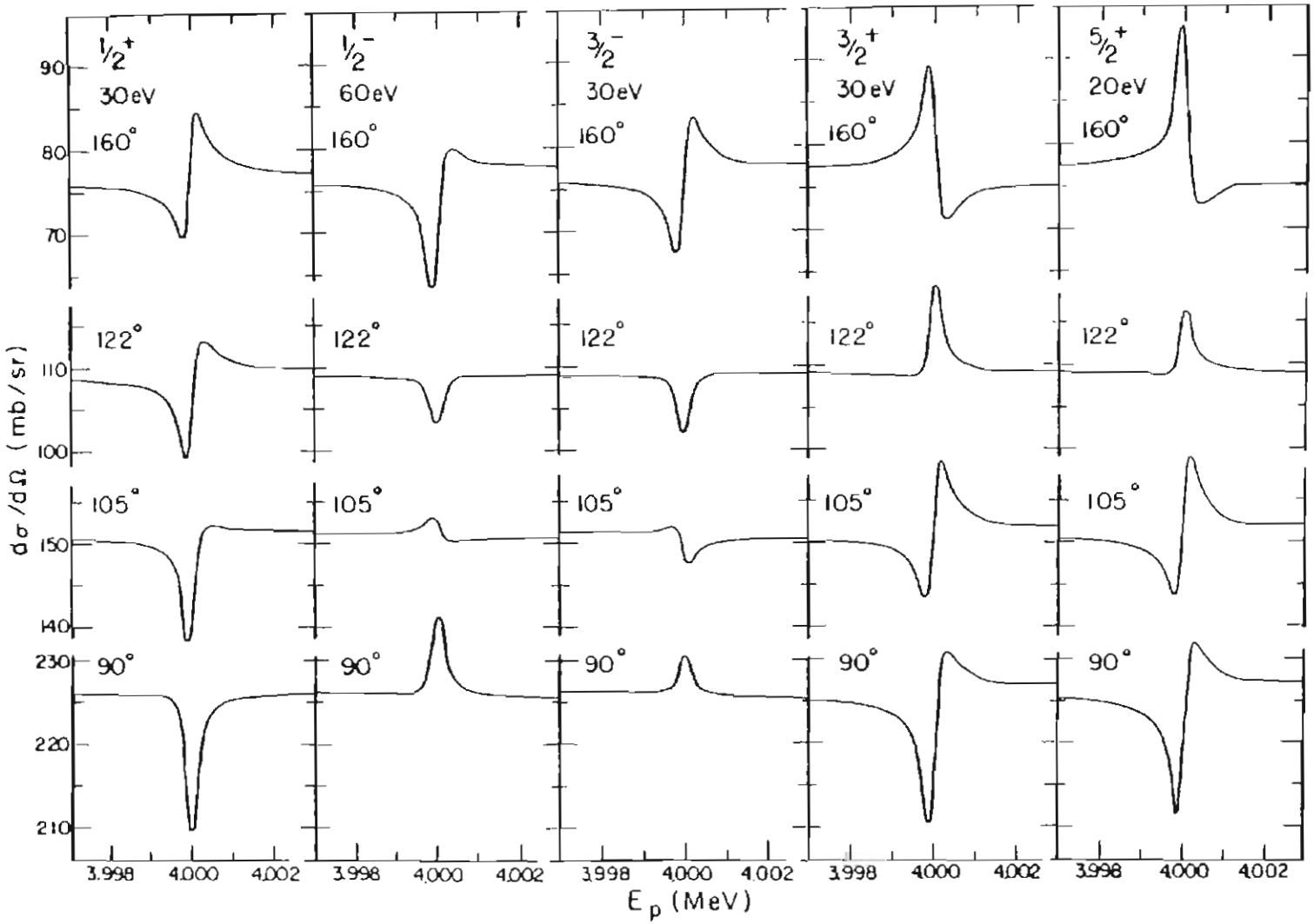
1/2+
30eV
160°
1/2−
60eV
160°
3/2−
30eV
160°
3/2+
30eV
160°
5/2+
20eV
160°
122°
105°
90°
dσ/dΩ (mb/sr)
90
80
70
110
100
150
140
230
220
210
3.998
4.000
4.002
Ep (MeV)

Figure 12. Typical Calculated Resonance Shapes in Proton Elastic Scattering. The spin, parity, and elastic width used to calculate each resonance shape are listed above the 160° data. An asymmetric resolution function of width 330 eV was used in the calculation. (The dashed lines are discussed in the text.)

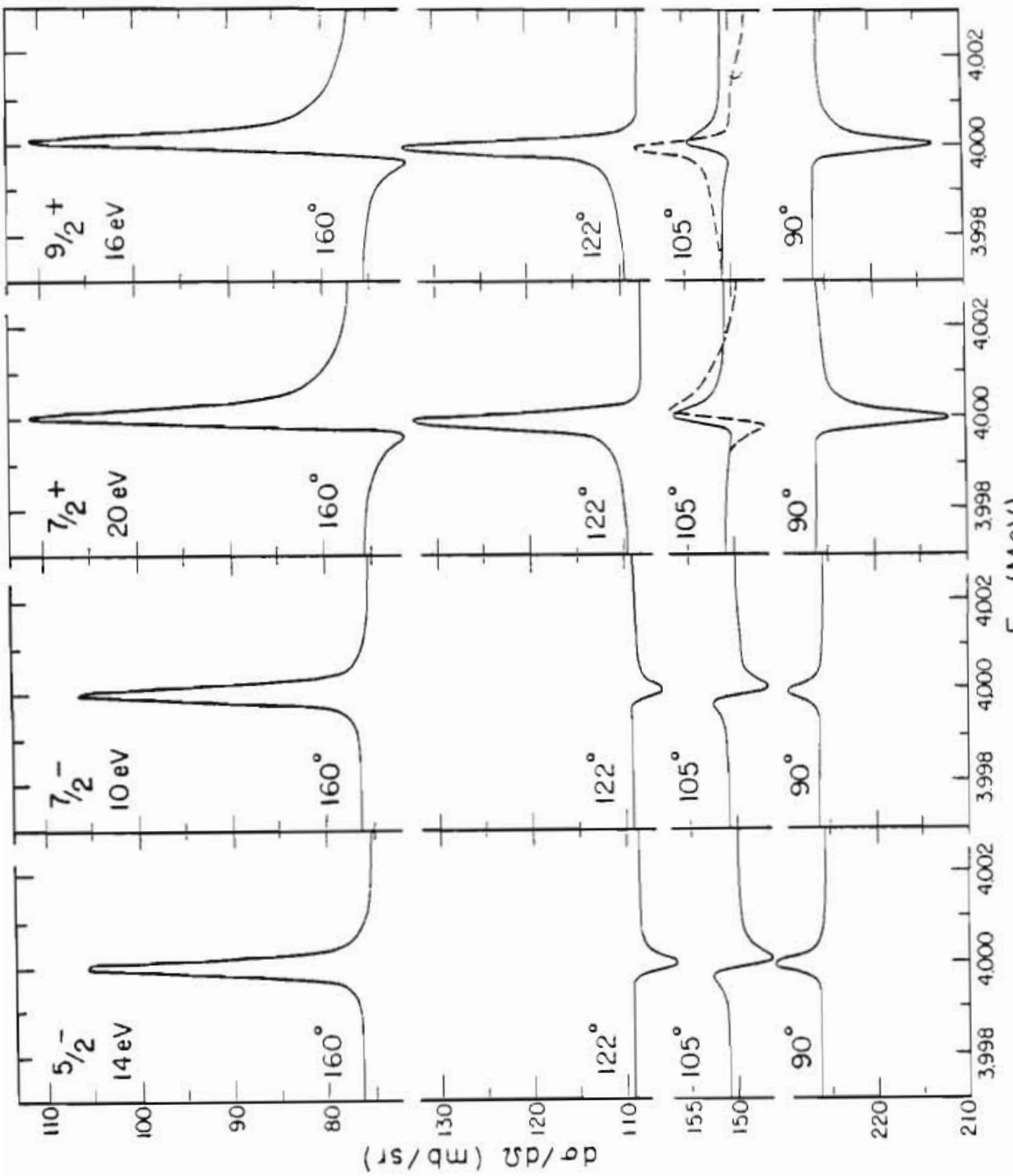
5/2⁻
14 eV
7/2⁻
10 eV
7/2⁺
20 eV
9/2⁺
16 eV
160°
122°
105°
90°
dσ/dΩ (mb/sr)
E_p (MeV)

qenerated at other anqles with these same parameters. Fiqure 11 shows the results at four anqles. The value 105° was chosen because there is a distinct rise in the cross section for $1/2^-$ resonances and a distinct dip in the cross section for $3/2^-$ resonances. The same procedure was followed for the d-wave resonances; the results are also shown in fiqure 11. The value 122° was chosen because at this anqle the difference between the $3/2^+$ and $5/2^+$ cross sections was qreatest. The spin assiqnment of many p- and d-wave resonances with strenqths <1 keV relied on the data at 105° and 122°, respectively.

Interference with other nearby resonances also helped to identify the resonance spins. An example of such interference is shown for the $7/2^+$ and $9/2^+$ resonances at 105° in figure 12. The dashed lines were calculated with an 11 keV $1/2^-$ resonance located at 4.003 MeV. (Note that the dashed lines have been shifted for ease of viewing: 10 mb/sr was subtracted from each point before plottinq.) With the p-wave resonance included, the characteristic shapes of the $7/2^+$ and $9/2^+$ resonances are quite different at 105°. In ^{55}Co, the spin of an $\ell=4$ state at 3.4666 MeV was uniquely identified as 9/2 because of interference with the nearby $1/2^-$ resonance at 3.4720 MeV (data and resonance parameters are presented in section III E).

As discussed above, spins and parities were usually obtained by an analysis of the elastic excitation functions.

Since the elastic excitation function depends on the total decay width, knowledge of the total inelastic width is also necessary in making spin assignments. For example, the peak on the high energy side of the elastic excitation function of a $3/2^-$ resonance is pulled down by increasing inelastic strength until the $3/2^-$ resonance appears very similar to a $1/2^-$ resonance (see the $3/2^-$ resonances at 3.9479 and 4.4051 MeV in figures 19 and 20).

Some spin assignments were made by analyzing the inelastic excitation functions. When the compound state decays by only <u>one</u> inelastic channel, (i.e., only one inelastic reduced width is non-zero) a characteristic angular distribution is obtained. Each of these possible angular distributions is shown in figure 13 for resonances of different spins and parities. In order to generate the other possible inelastic angular distributions, one can add linear combinations of the "characteristic" angular distributions shown for each allowed inelastic channel -- as long as no two exit channels have the same channel spin. Consider the angular distributions shown in figure 13 for $3/2^-$ resonances: if one multiplies the curve labeled (0,20) (decay via s' =5/2) by four and adds it to the curve labeled (20,0) (decay via s' =3/2), then the angular distribution of the curve labeled (4,16) is obtained. This is an example of "incoherent addition" of differential cross sections. On the other hand, consider the angular distributions shown for

Figure 13. Calculated Angular Distributions for the Inelastically Scattered Protons. Spin, parity, and elastic width of the compound state are shown in the upper left corner of each of the smaller figures. The numbers above each curve give the strengths (in eV) of the inelastic exit channels according to the following convention:

$3/2^-$ first number is $\Gamma_{p'}$ for $\ell'=1$, $s'=3/2$
second number is $\Gamma_{p'}$ for $\ell'=1$, $s'=5/2$

$3/2^+$ first number is $\Gamma_{p'}$ for $\ell'=0$, $s'=3/2$
second number is $\Gamma_{p'}$ for $\ell'=2$, $s'=3/2$
third number is $\Gamma_{p'}$ for $\ell'=2$, $s'=5/2$

$5/2^+$ first number is $\Gamma_{p'}$ for $\ell'=0$, $s'=5/2$
second number is $\Gamma_{p'}$ for $\ell'=2$, $s'=3/2$
third number is $\Gamma_{p'}$ for $\ell'=2$, $s'=5/2$

$5/2^-$ first number is $\Gamma_{p'}$ for $\ell'=1$, $s'=3/2$
second number is $\Gamma_{p'}$ for $\ell'=1$, $s'=5/2$

$7/2^-$ number is $\Gamma_{p'}$ for $\ell'=1$, $s'=5/2$

$7/2^+$ first number is $\Gamma_{p'}$ for $\ell'=2$, $s'=3/2$
second number is $\Gamma_{p'}$ for $\ell'=2$, $s'=5/2$

$9/2^+$ number is $\Gamma_{p'}$ for $\ell'=2$, $s'=5/2$

As an aid in distinguishing multiple curves on the same smaller figure, the cross sections represented by the dashed curves were shifted to concide at 90°.

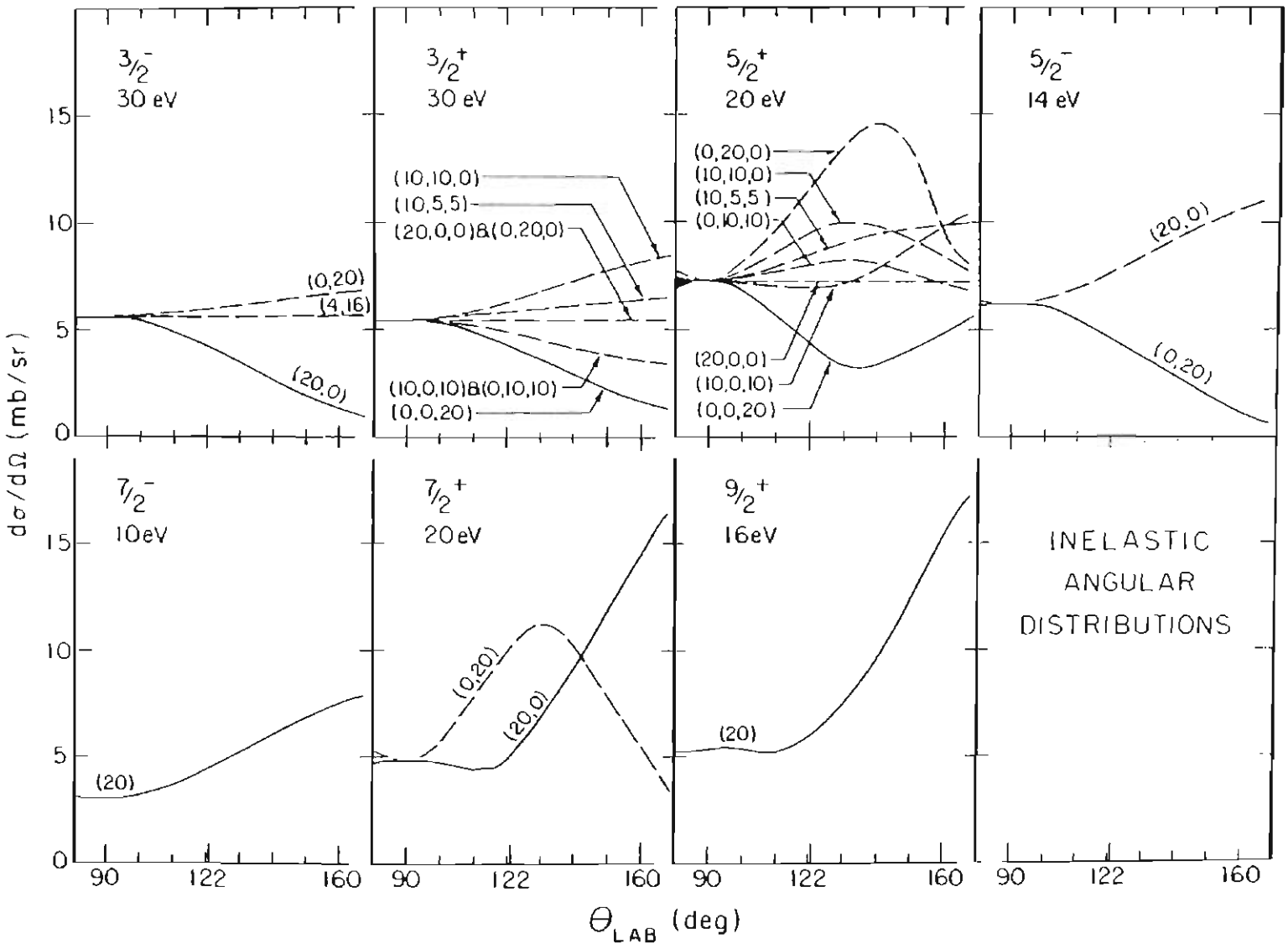
3/2⁻
30 eV
(0,20)
(4,16)
(20,0)
3/2⁺
30 eV
(10,10,0)
(10,5,5)
(20,0,0)&(0,20,0)
(10,0,10)&(0,10,10)
(0,0,20)
5/2⁺
20 eV
(0,20,0)
(10,10,0)
(10,5,5)
(0,10,10)
(20,0,0)
(10,0,10)
(0,0,20)
5/2⁻
14 eV
(20,0)
(0,20)
7/2⁻
10eV
(20)
7/2⁺
20eV
(0,20)
(20,0)
9/2⁺
16eV
(20)
INELASTIC
ANGULAR
DISTRIBUTIONS
dσ/dΩ (mb/sr)
0
5
10
15
90
122
160
θ LAB (deg)

$3/2^+$ resonances: no linear combination of the curve labeled (20,0,0) (decay via s'=3/2) and the curve labeled (0,20,0) (also decay via s'=3/2) can give the curve labeled (10,10,0). This is due to an "interference" term in the expression for the differential cross section and is an example of "coherent addition" of the cross sections.

Several different combinations of the inelastic reduced widths are shown in figure 13 in order to illustrate how this interference term affects the angular distributions. A knowledge of the possible angular distributions of the protons inelastically scattered from a particular compound state is often of value when making spin assignments. An anisotropic distribution for an $\ell=1$ resonance requires that the resonance have J=3/2 and not J=1/2. A nonmonotonic distribution between 90° and 180° for an $\ell=2$ resonance requires J=5/2 and not J=3/2. A monotonically decreasing distribution between 90° and 180° for an $\ell=2$ resonance requires J=3/2 and not J=5/2. A distribution which does not increase at back angles for an $\ell=3$ resonance requires J=5/2 and not J=7/2. A distribution that is not sharply peaked at back angles for an $\ell=4$ resonance requires J=7/2 and not J=9/2. In the analysis of the present data, many spin assignments were made by such considerations of the inelastic data.

Once the spin and parity of a resonance is determined, there are several widths to adjust to obtain the

best fit to the seven excitation functions that were simultaneously measured. These widths are listed in the caption of figure 13. It is not always possible to uniquely assign values to all of these widths. In such cases the assignments were made systematically as follows. For $1/2^+$ resonances both inelastic channels have isotropic distributions; the convention adopted was to make the two widths equal. For p-wave, f-wave, and g-wave resonances there is no such ambiguity, and the widths were adjusted for the best fit. For d-wave resonances problems arise because there are three allowed inelastic exit channels. In the inelastic angular distributions of a $3/2^+$ resonance, shown in figure 13, two different combinations of inelastic reduced widths are shown that can produce the same angular distribution. Since the penetrabilties enhance the $\ell'=0$ strengths relative to the $\ell'=2$ strengths, $\Gamma_{p'}(\ell'=2, s'=3/2)$ was assumed zero unless the experimental distribution increased at back angles. A similar degeneracy does not appear to occur with a $5/2^+$ resonance; although, due to experimental uncertainties, there are difficulties in assigning relative inelastic strengths. Again the $\ell'=0$ component was assumed to predominate and the other strengths were added as necessary to improve the fit.

The experimental uncertainties in the inelastic cross sections severely limit the assignment of relative strengths and, in many cases, even hamper the assignment of

J values. These uncertainties arise mainly from uncertain normalizations[1]. The elastic data are easily normalized from the Coulomb (plus hard sphere) background. Since the inelastic protons are measured at the same time as the elastic protons, their normalizations (mb/sr per count) should be the same as for the elastic protons. Due to incomplete knowledge of the resonance background (i.e., strong resonances at energies just above the range observed affect the "background"), an error is incurred in normalizing the data in this manner. More importantly, the resonance background created by such a large level (or levels) affects the data at 160° more than that at 90° and thus leads to incorrect relative normalizations. Relative normalizations can also be obtained either from the known solid angles or from a resonance with a known inelastic angular distribution.

Relative normalizations obtained from each of the three methods described above agreed within ±20%. Since the inelastic data of the $9/2^+$ resonance at 3.4666 MeV in ^{55}Co appeared excellent, and since the inelastic angular distribution was unique, this distribution was chosen as a reference. The relative normalizations used for all of the inelastic data were obtained from this angular distribution

---

1. Statistical fluctuation in these data are ~5% for smaller resonances and less for larger resonances; the normalization uncertainties may be as large as 15 - 20%.

(the normalization for the inelastic data at 90° was assumed to be the same as that for the elastic data at 90°). Several other resonances with known inelastic angular distributions yield relative normalizations which are consistent within ±15% for norm.(90°)/ norm.(160°) and ±10% for norm.(90°)/ norm.(122°). Inconsistent setting of the window around the inelastic pulses may account for these varying relative normalizations.

There was no coherent inelastic background observed in these experiments. (That is, the inelastic peak in the spectrum (see figure 8) disappeared off resonance.) For this reason, the shape of the inelastic peaks in the excitation function was simply that of the resolution function for $\Gamma_{TOTAL} << \Gamma_S$, a Lorentzian for $\Gamma_{TOTAL} >> \Gamma_S$, or a convolution of the two in general.

There was always an incoherent background in both the elastic and inelastic data. For the elastic data it was normally less than 5% of the Coulomb background and was easily subtracted during the fitting process. For the inelastic data, the background fluctuated depending on the beam conditions (see section II B 1). Typical backgrounds of 500, 300, and 100 counts were observed at 160°, 122°, and 90°, respectively, corresponding to a differential cross section of 5 – 10 mb/sr. The inelastic background was carried throughout the fitting process and was subtracted

when the final plots were made.

D. Energy Corrections

The resonance energies obtained from fitting the excitation functions have been shifted to correct for several errors. First, the measured energy of a given resonance was dependent on the length of time the beam had been in the electrostatic analyzer (see figure 14). A similiar problem has been observed with the 3 MeV homogenizer system (Wilson 1973). Since the drift rate was 3 or 4 times worse in the present system it was necessary to do more than simply correct the data as Wilson did. The first approach was to wait until the system stabilized before taking data. Figure 14 shows that the drift stabilized after about seventeen hours. Some of the data was taken in this manner.

However, energy shifts of several kilovolts were still observed from run to run. These were corrected by measuring several "calibration resonances" throughout the excitation function. One resonance was used as a base and the energy difference between this resonance and each of the other calibration resonances was measured as quickly as possible. The energies obtained in fitting the data were

Figure 14. Energy Drift Versus Time the Beam Passed Through the Electrostatic Analyzer.

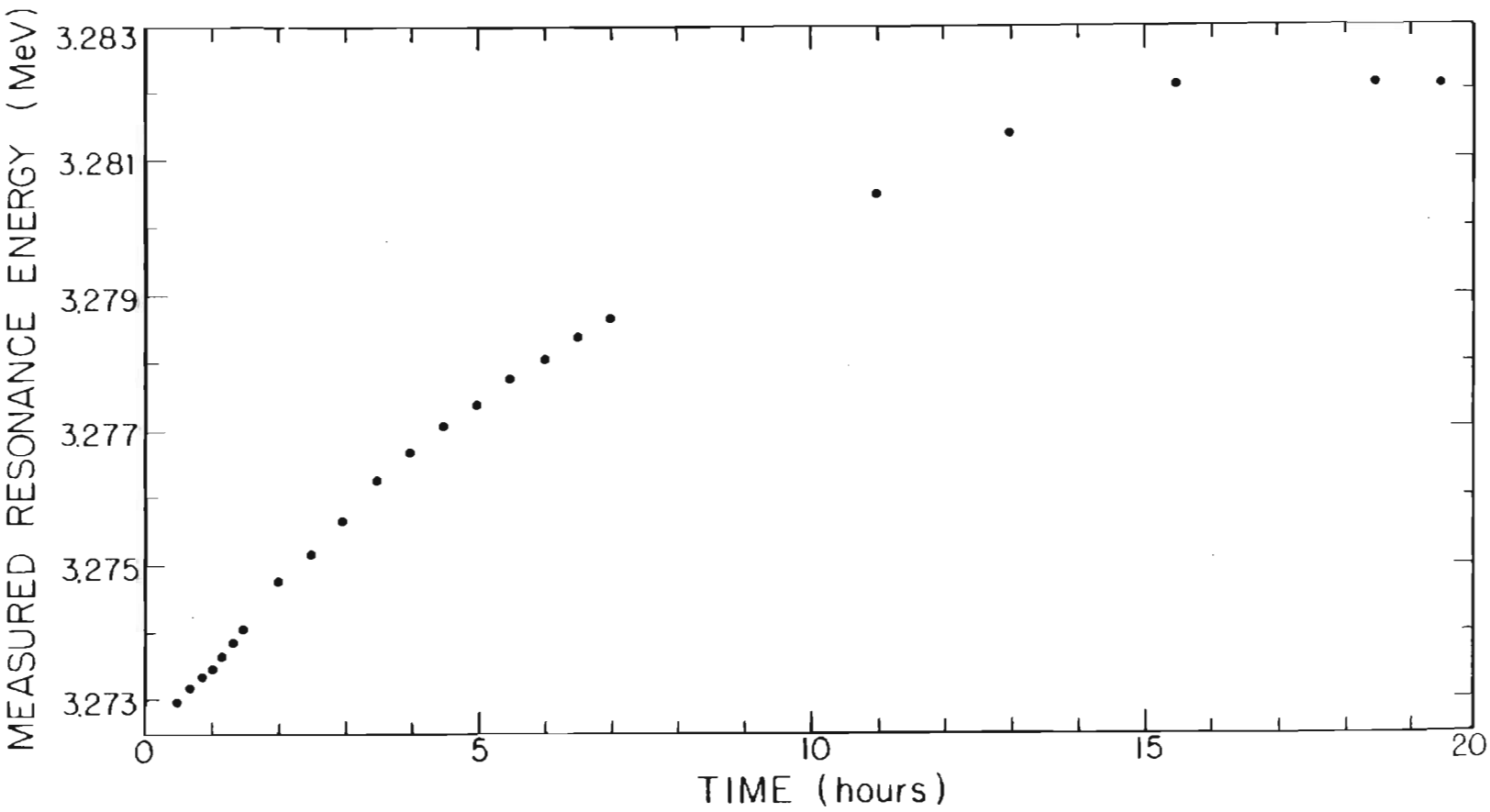
MEASURED RESONANCE ENERGY (MeV)
3.283
3.281
3.279
3.277
3.275
3.273
0
5
10
15
20
TIME (hours)

then shifted[1] so that the calibration resonances were correct.

The second approach to correcting the drift problem was to eliminate the cause. The beam entering the electrostatic analyzer (ESA) consisted of neutral hydrogen and singly ionized atomic and molecular hydrogen. Since only the free protons pass through the ESA, the rest of the beam collides with and heats the outer plate of the ESA. The resulting expansion changes the geometry of the ESA and causes a shift in energy.

In the latter part of this experiment, the energy - shift problem was removed by inserting a magnet[2] between the dissociator and the ESA. This, combined with a limiting slit, kept the unwanted components of the beam out of the ESA. After this modification, the energy reproducibility was consistently within ±600 eV, and no drift was observed.

The measured energies are obtained as discussed in section II A 5. Systematic errors due to relativistic effects and due to the system design are known. These corrections are discussed in the appendix where the follow-

---

1. The resonances between the calibration resonances were corrected by a linear extrapolation.
2. The magnetic field was just strong enough to resolve the components of the beam. The magnet current supply was well regulated and was varied with the energy to keep the protons entering the ESA. The above factors combined in such a way that maladjusting the magnet current the equivalent of 100 keV in reaction energy gave an error in measured energy of only 200 eV.

ing equation is derived:

$$\mathcal{E} \equiv T_R - T_{RM} = T_{RM}(MeV)\left(\frac{T_{RM} - T_{RM}^c}{3760}\right) + \left(\frac{T_{RM}}{T_{RM}^c}\, eV_S^c - eV_S\right)$$

where

$\mathcal{E}$ = error in the measured energies,

T_R = reaction energy,

T_{RM} = measured reaction energy,

V_S = dissociator voltage + target voltage - twice the outer plate voltage,

the superscript "c" means the value at calibration.

All of the resonance energies were corrected with the above equation after calibrating the system on the $^{13}C(p,n)$ threshold at 3.2357 MeV. To illustrate the importance of this correction, suppose that one calibrates at 3.2357 MeV with an outer plate voltage of 24 kV. Then suppose that data are measured up to 4.5 MeV with the same 24 kV on the outer plate. In this case,

T_{RM} = 4.5 MeV,

T_{RM}^c = 3.2357 MeV,

voltage of dissociator = voltage of target = 3 kV,

$V_S = V_S^c = 6{,}000 - 2(24{,}000) = 42$ kV,

and

$$\mathcal{E}\left[\frac{4.5(4.5 - 3.2357)}{3.76} + \left(\frac{4.5}{3.2357}(42) - 42\right)\right]$$

or $\mathcal{E} = 1.51 + 16.41 = \underline{17.92 \text{ keV.}}$

The final energies (presented in section III E) of

several well-identified resonances have been compared with those from other measurements recently performed by Brändle et al. (1975) and Arai et al. (1976). Figure 15 shows the difference between the present resonance energies and those of Brändle and Arai, plotted as a function of energy. Excellent agreement is found except for discontinuties at 3.4 and at 3.9 MeV in ^{58}Ni(p,p). A study of the original data in the present work suggests that the observed energy shifts are not caused by the present data: in order to improve the data, many measurements were repeated; the resonance energies measured on these different occasions were in agreement with each other.

E. Data

In this section all of the data and fits are shown, and the extracted resonance parameters are presented. These parameters are compared with those of other recent measurements.

Figure 16 shows plots of the differential cross sections at 160° for ^{55}Co, ^{59}Cu, and ^{61}Cu over the entire energy range. The solid lines are fits to the data. For more detailed study, figures 17 to 20 show plots of all of the data and fits for ^{54}Fe(p,p) and ^{54}Fe(p,p'); figures 21 to 24 show plots of all of the data and fits for ^{58}Ni(p,p) and ^{58}Ni(p,p'); and figures 25 and 26 show plots of all of

Figure 15. Comparison of Resonance Energies of the Present Work with those of Brändle et al. (top) and Arai et al. (bottom).

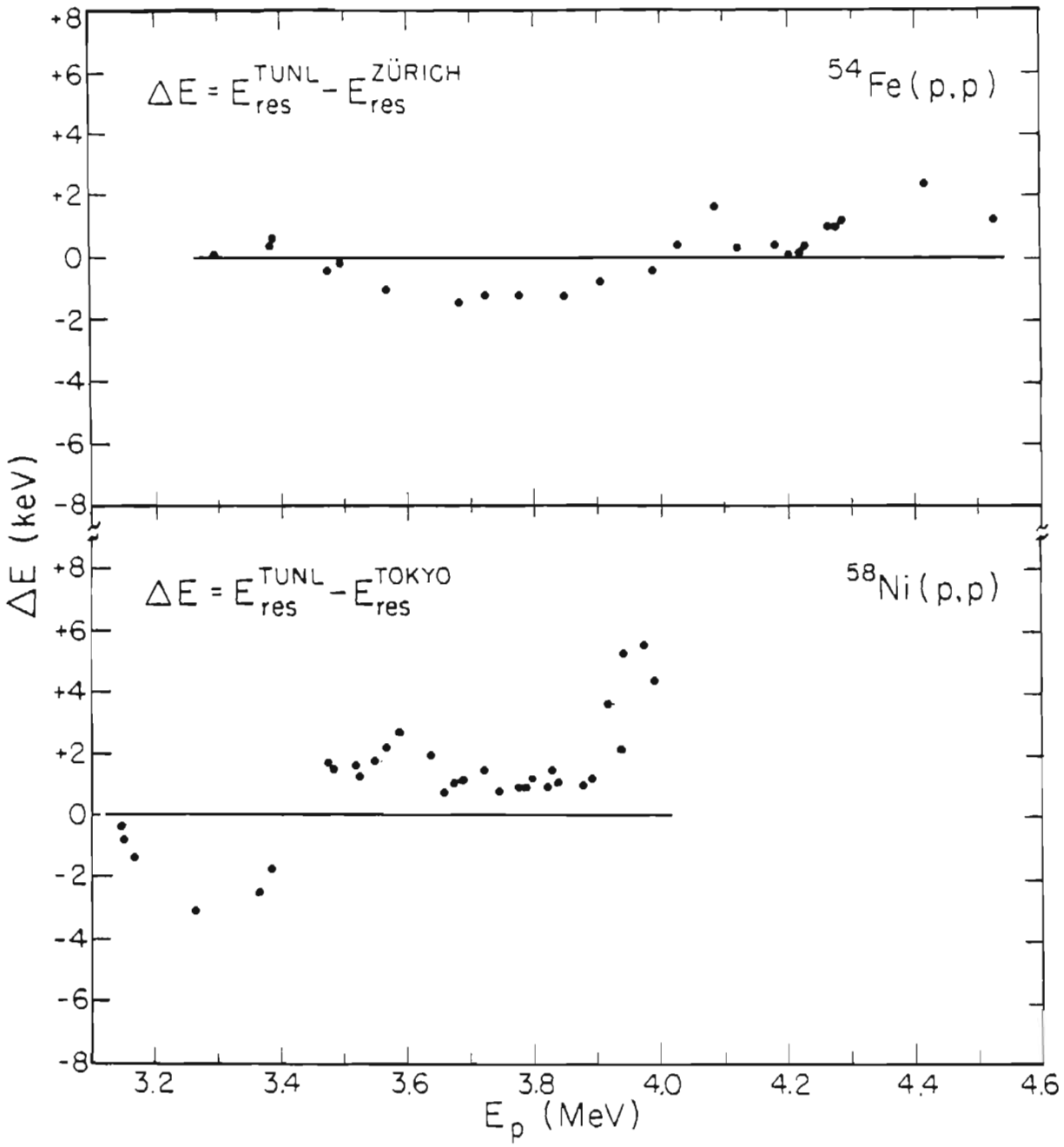
ΔE = E_res^TUNL − E_res^ZÜRICH
54Fe(p,p)
ΔE = E_res^TUNL − E_res^TOKYO
58Ni(p,p)
ΔE (keV)
E_p (MeV)
+8
+6
+4
+2
0
-2
-4
-6
-8
3.2
3.4
3.6
3.8
4.0
4.2
4.4
4.6

Figure 16. The ^{55}Co, ^{59}Cu, and ^{61}Cu Differential Cross Sections at 160° Over the Entire Energy Range. The solid line represents a fit to the data.

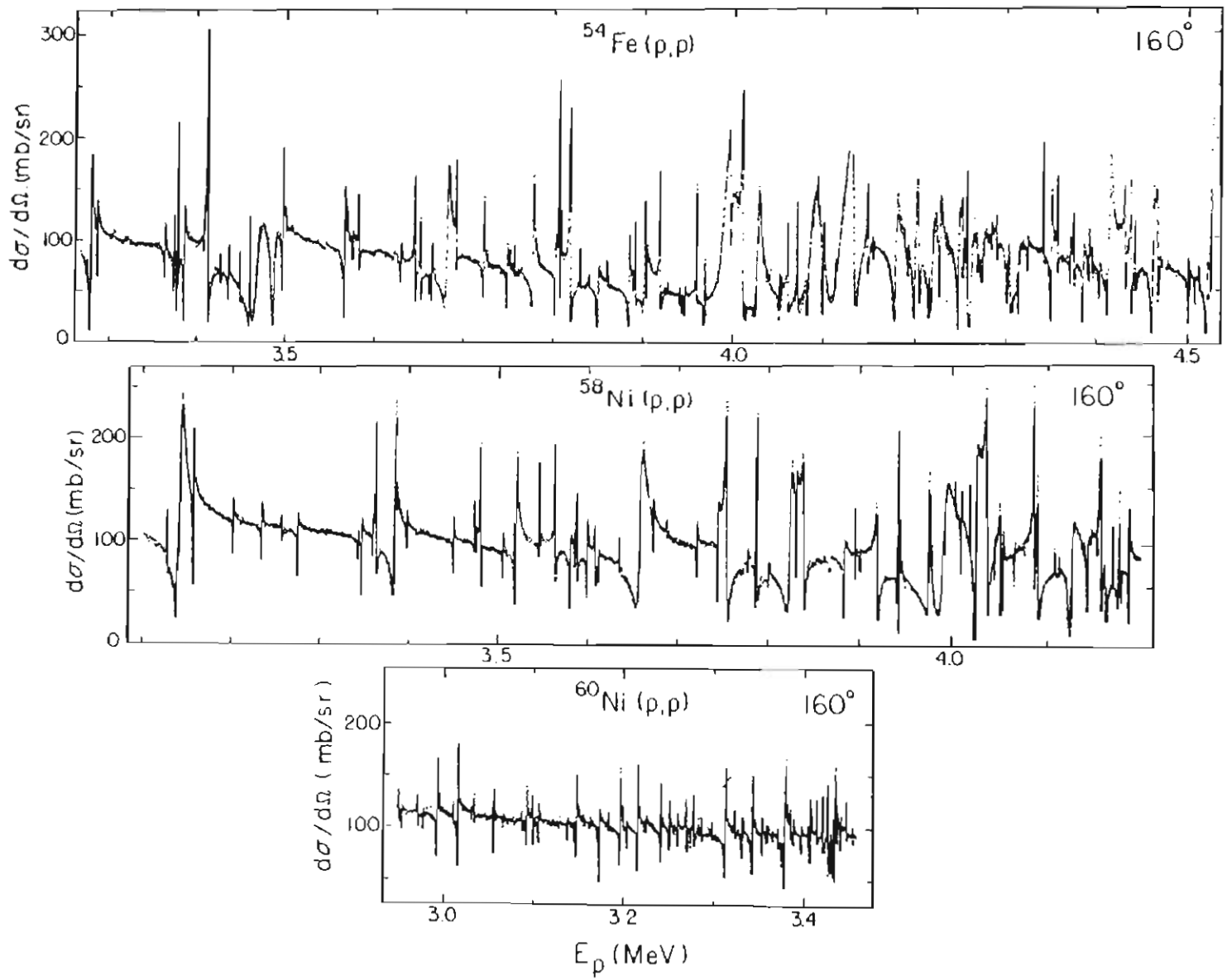
^{54}Fe (p,p)
160°
dσ/dΩ (mb/sr)
300
200
100
0
3.5
4.0
4.5
^{58}Ni (p,p)
160°
dσ/dΩ (mb/sr)
200
100
0
3.5
4.0
^{60}Ni (p,p)
160°
dσ/dΩ (mb/sr)
200
100
3.0
3.2
3.4
E_p (MeV)

Figure 17. The $^{54}Fe(p,p)$ and $^{54}Fe(p,p')$ Differential Cross Sections from 3.28 to 3.56 MeV. The solid line represents a fit to the data.

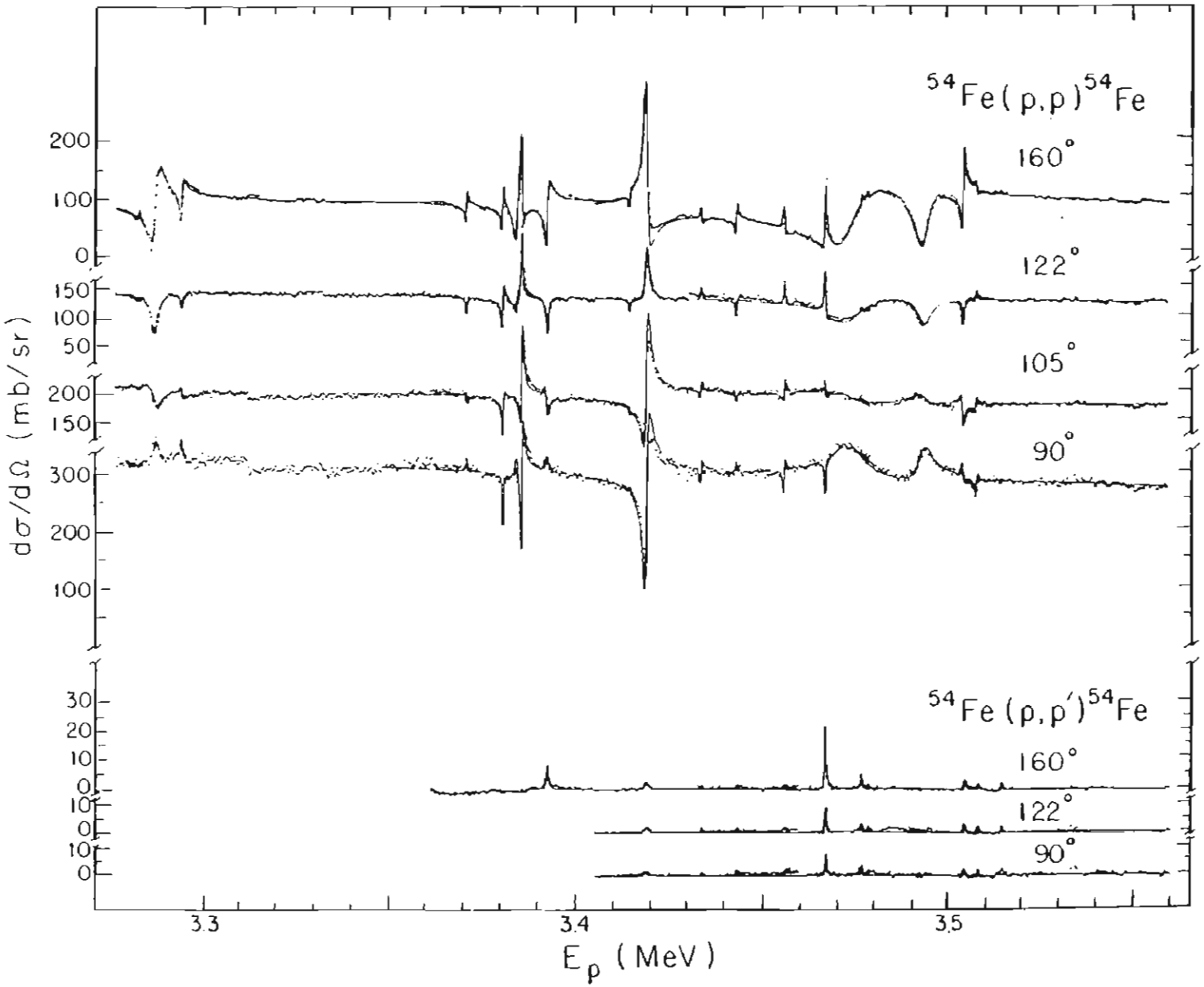
^{54}Fe(p,p)^{54}Fe
160°
122°
105°
90°
^{54}Fe(p,p')^{54}Fe
160°
122°
90°
dσ/dΩ (mb/sr)
E_p (MeV)
3.3
3.4
3.5

Figure 18. The $^{54}Fe(p,p)$ and $^{54}Fe(p,p')$ Differential Cross Sections from 3.56 to 3.86 MeV. The solid line represents a fit to the data.

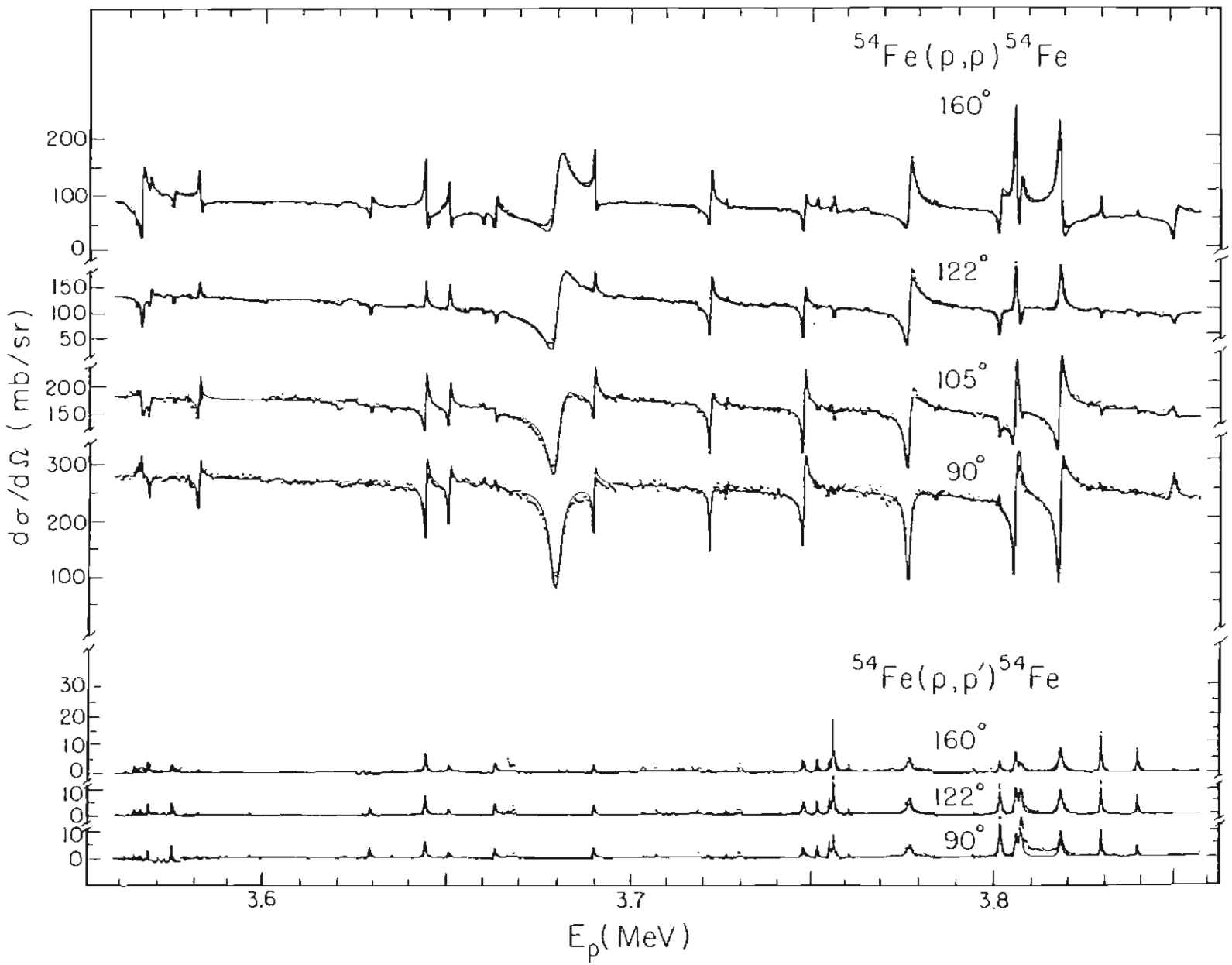
$^{54}Fe(p,p)^{54}Fe$
160°
122°
105°
90°
$^{54}Fe(p,p')^{54}Fe$
160°
122°
90°
dσ/dΩ (mb/sr)
E_p(MeV)
3.6
3.7
3.8

Figure 19. The $^{54}Fe(p,p)$ and $^{54}Fe(p,p')$ Differential Cross Sections from 3.86 to 4.16 MeV. The solid line represents a fit to the data.

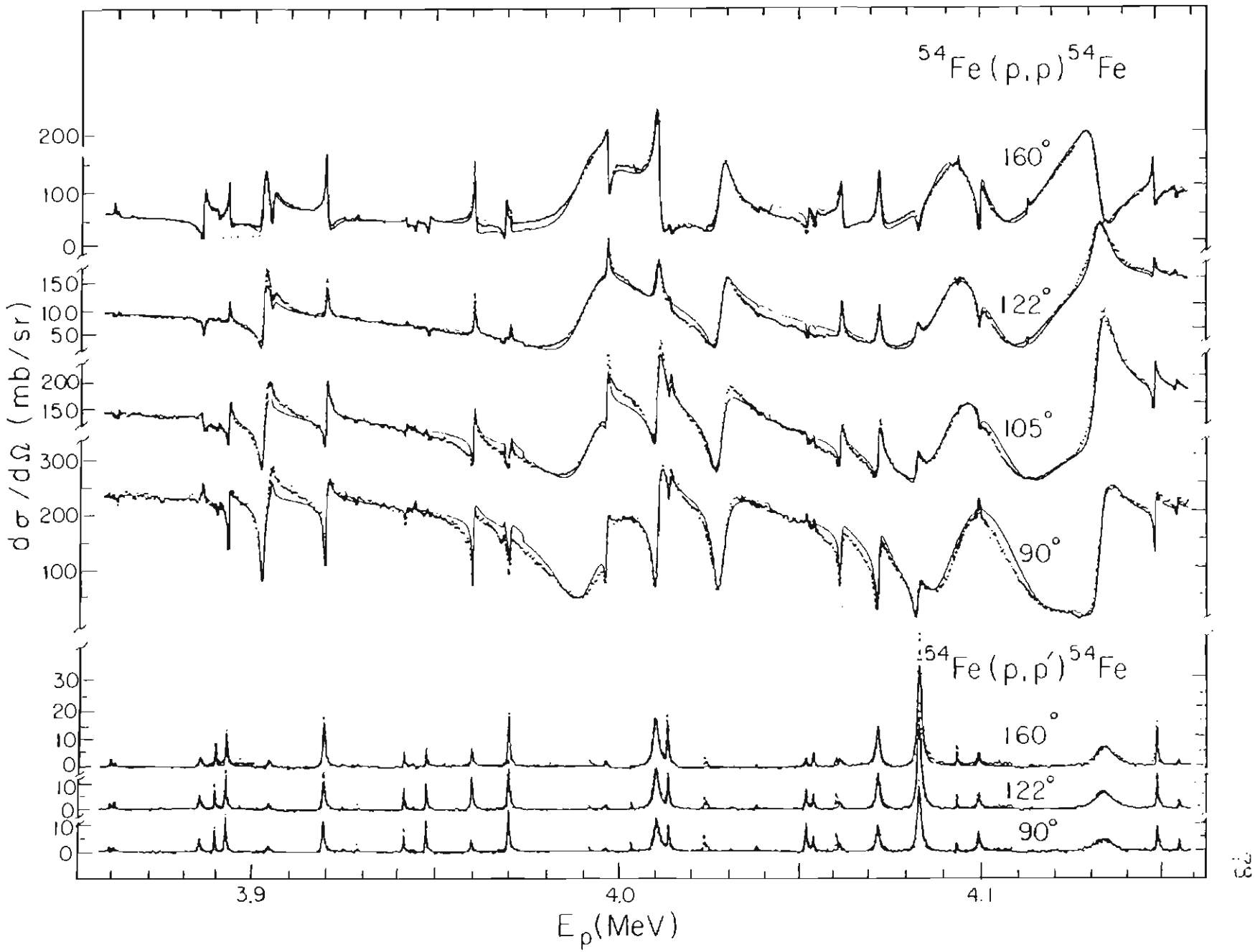
$^{54}Fe(p,p)^{54}Fe$
160°
122°
105°
90°
$^{54}Fe(p,p')^{54}Fe$
160°
122°
90°
dσ/dΩ (mb/sr)
E_p(MeV)
3.9
4.0
4.1

Figure 20. The $^{54}Fe(p,p)$ and $^{54}Fe(p,p')$ Differential Cross Sections from 4.16 to 4.53 MeV. The solid line represents a fit to the data.

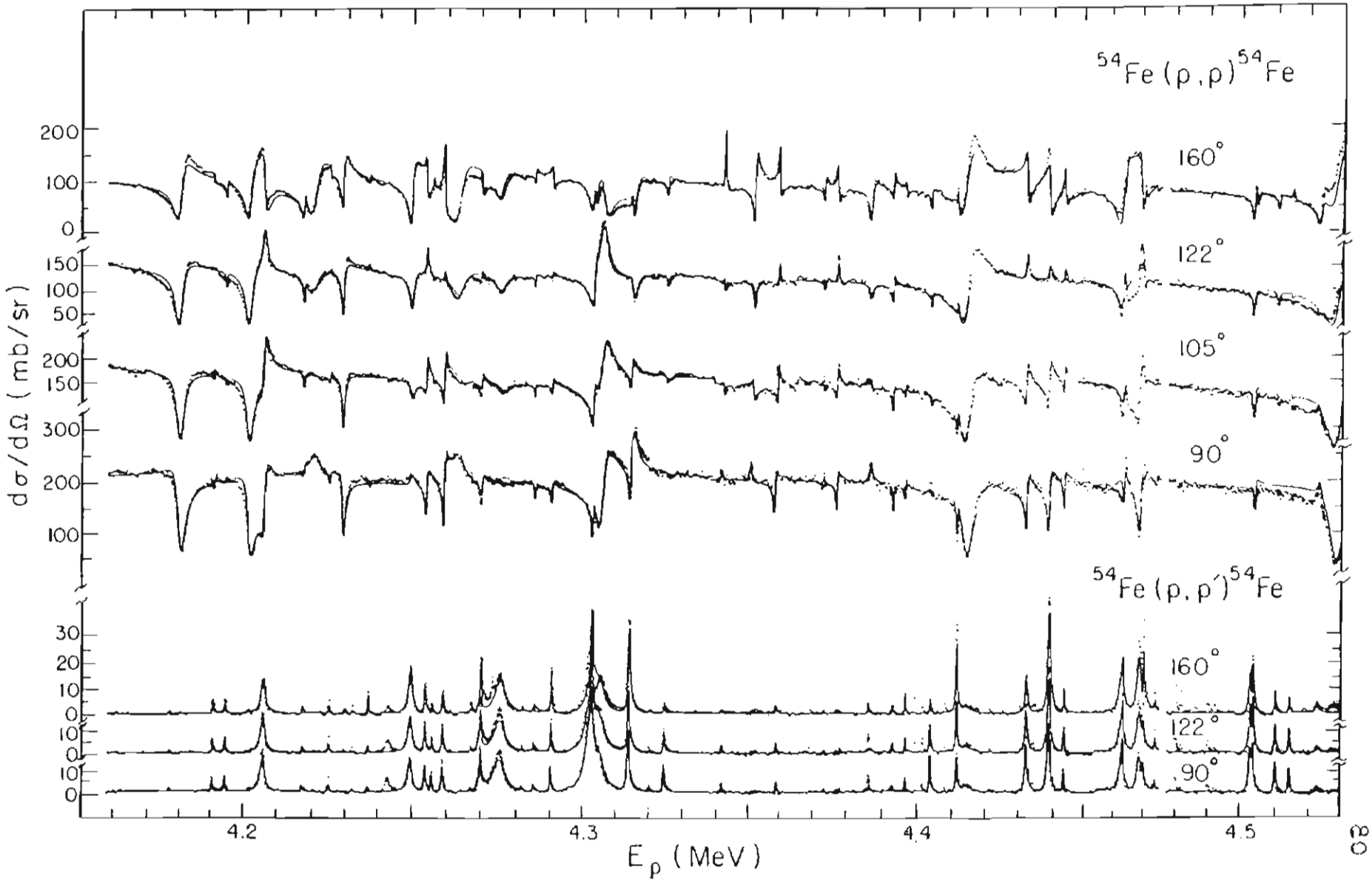
$^{54}Fe(p,p)^{54}Fe$
160°
122°
105°
90°
$^{54}Fe(p,p')^{54}Fe$
160°
122°
90°
$d\sigma/d\Omega$ (mb/sr)
E_p (MeV)
4.2
4.3
4.4
4.5
200
100
0
150
100
50
200
150
300
200
100
30
20
10
0
10
0
10
0

Figure 21. The ^{58}Ni(p,p) and ^{58}Ni(p,p') Differential Cross Sections from 3.11 to 3.40 MeV. The solid line represents a fit to the data.

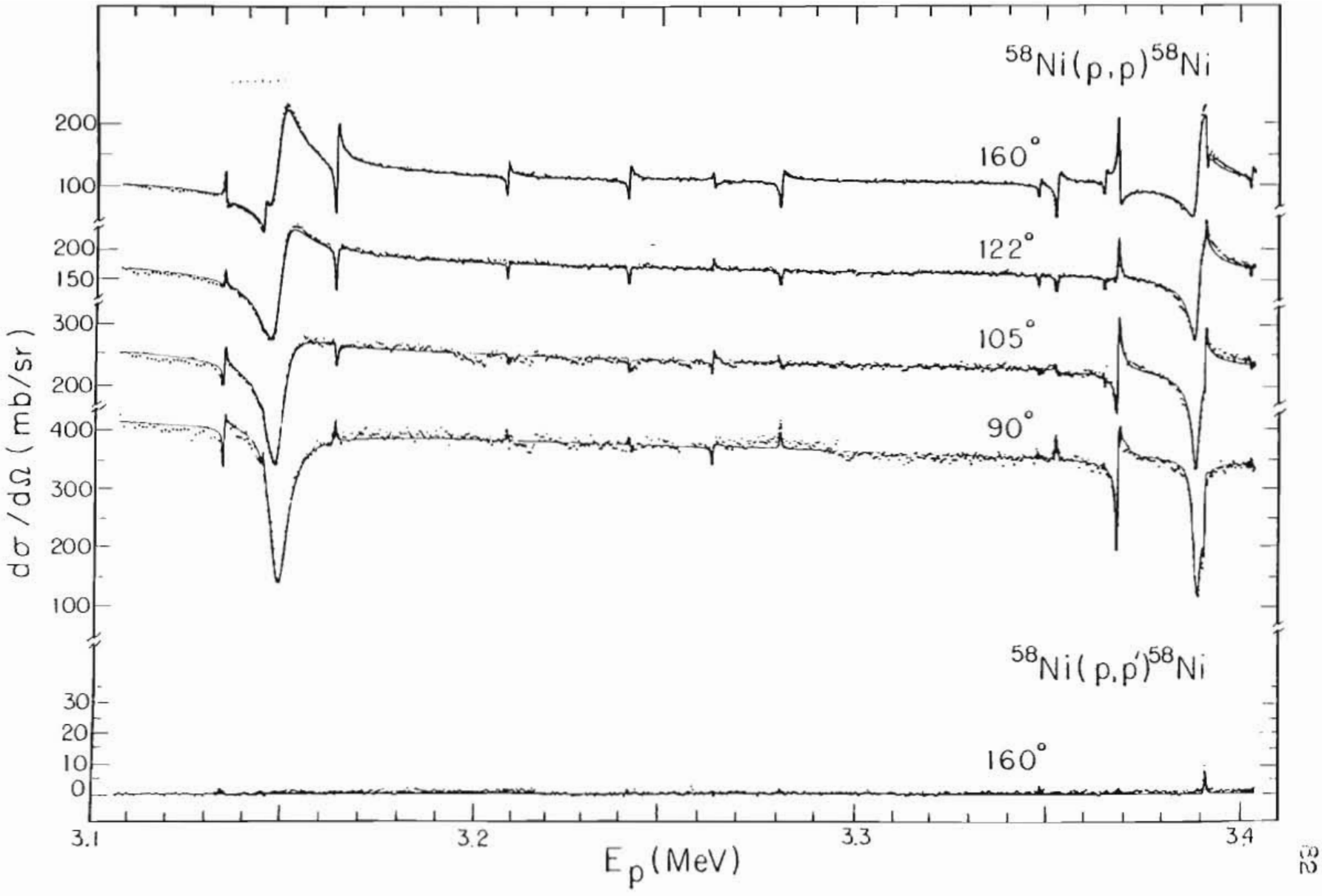
^{58}Ni(p,p)^{58}Ni
160°
122°
105°
90°
^{58}Ni(p,p')^{58}Ni
160°
dσ/dΩ (mb/sr)
E$_p$ (MeV)
3.1
3.2
3.3
3.4

Figure 22. The ^{58}Ni(p,p) and ^{58}Ni(p,p') Differential Cross Sections from 3.40 to 3.70 MeV. The solid line represents a fit to the data.

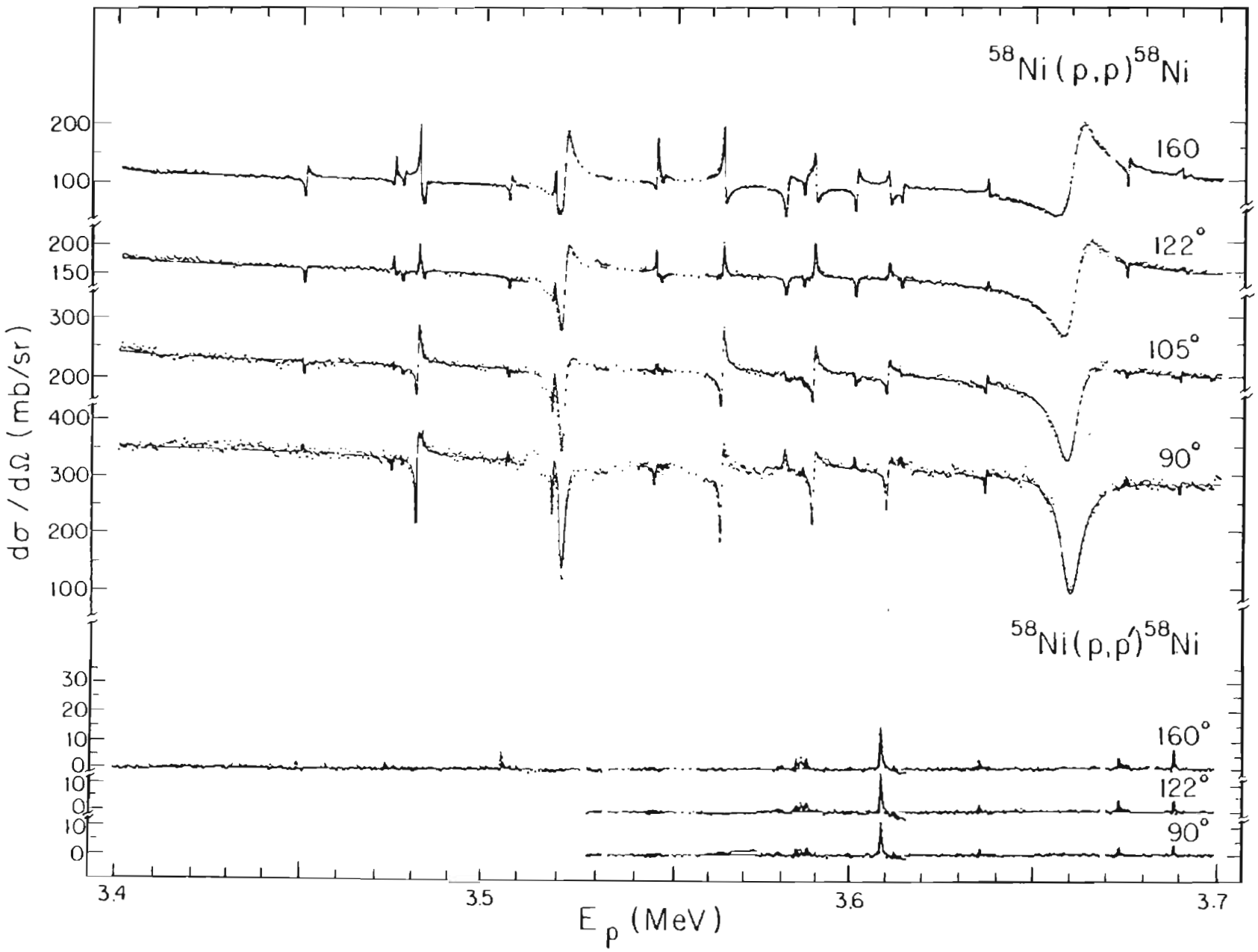
^{58}Ni(p,p)^{58}Ni
160
122°
105°
90°
^{58}Ni(p,p')^{58}Ni
160°
122°
90°
dσ / dΩ (mb/sr)
E$_p$ (MeV)
3.4
3.5
3.6
3.7

Figure 23. The ^{58}Ni(p,p) and ^{58}Ni(p,p') Differential Cross Sections from 3.70 to 4.00 MeV. The solid line represents a fit to the data.

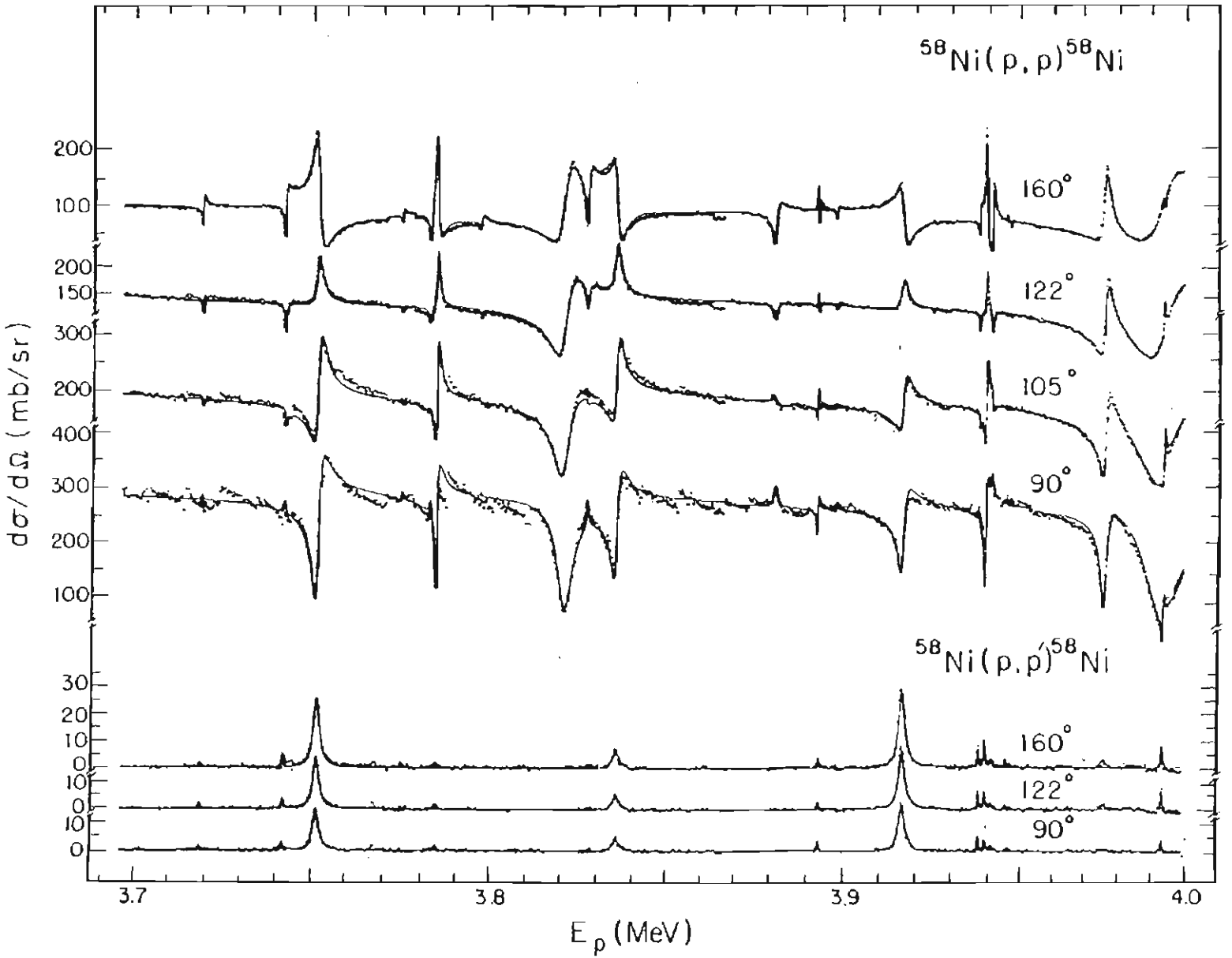
^{58}Ni(p,p)^{58}Ni
160°
122°
105°
90°
^{58}Ni(p,p')^{58}Ni
160°
122°
90°
dσ/dΩ (mb/sr)
E$_p$ (MeV)
3.7
3.8
3.9
4.0

Figure 24. The ^{58}Ni(p,p) and ^{58}Ni(p,p') Differential Cross Sections from 4.00 to 4.20 MeV. The solid line represents a fit to the data.

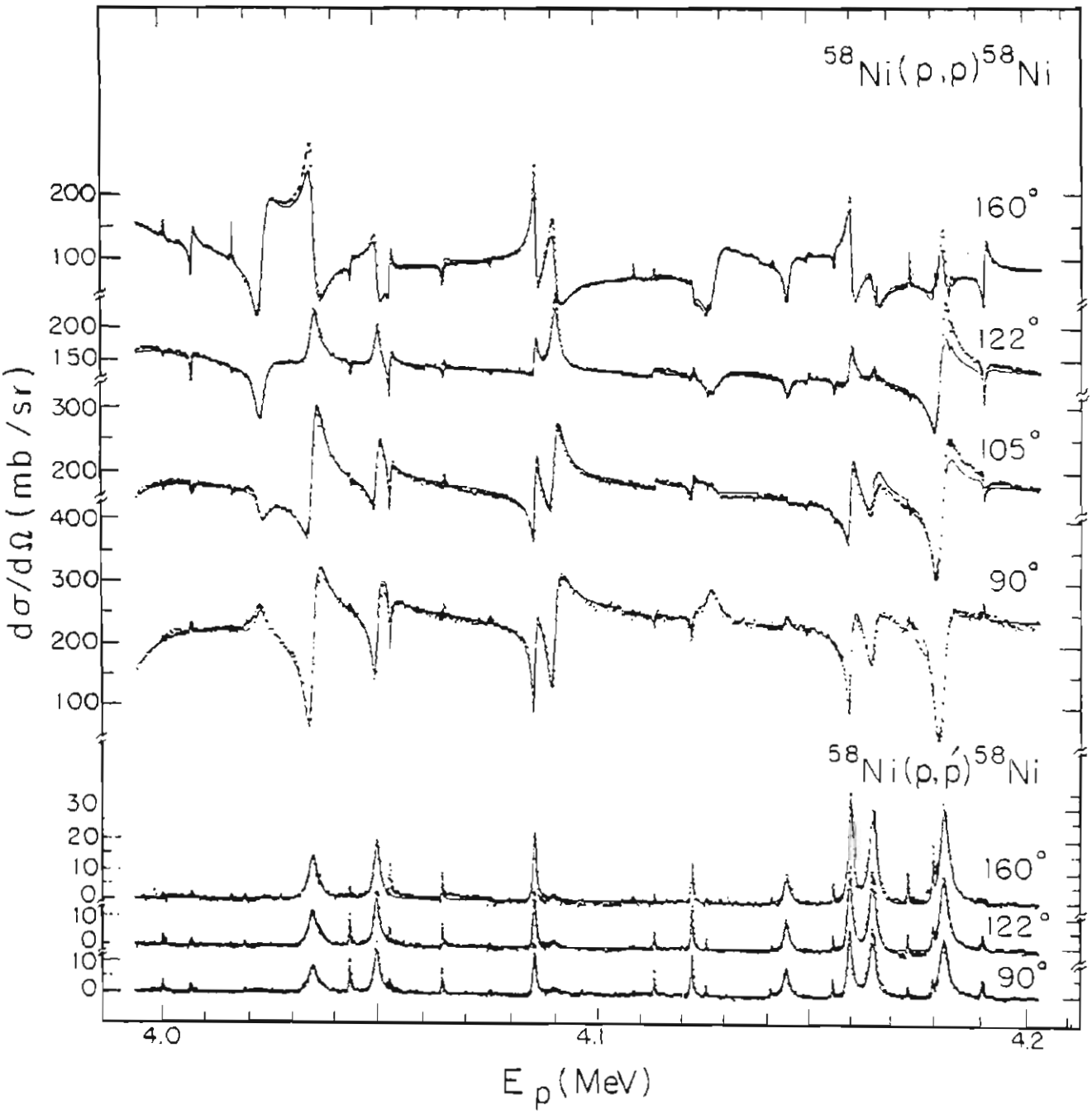
^{58}Ni(p,p)^{58}Ni
160°
122°
105°
90°
200
100
200
150
300
200
400
300
200
100
^{58}Ni(p,ṕ)^{58}Ni
160°
122°
90°
30
20
10
0
10
0
10
0
4.0
4.1
4.2
dσ/dΩ (mb/sr)
E p (MeV)

Figure 25. The $^{60}Ni(p,p)$ and $^{60}Ni(p,p')$ Differential Cross Sections from 2.95 to 3.20 MeV. The solid line represents a fit to the data.

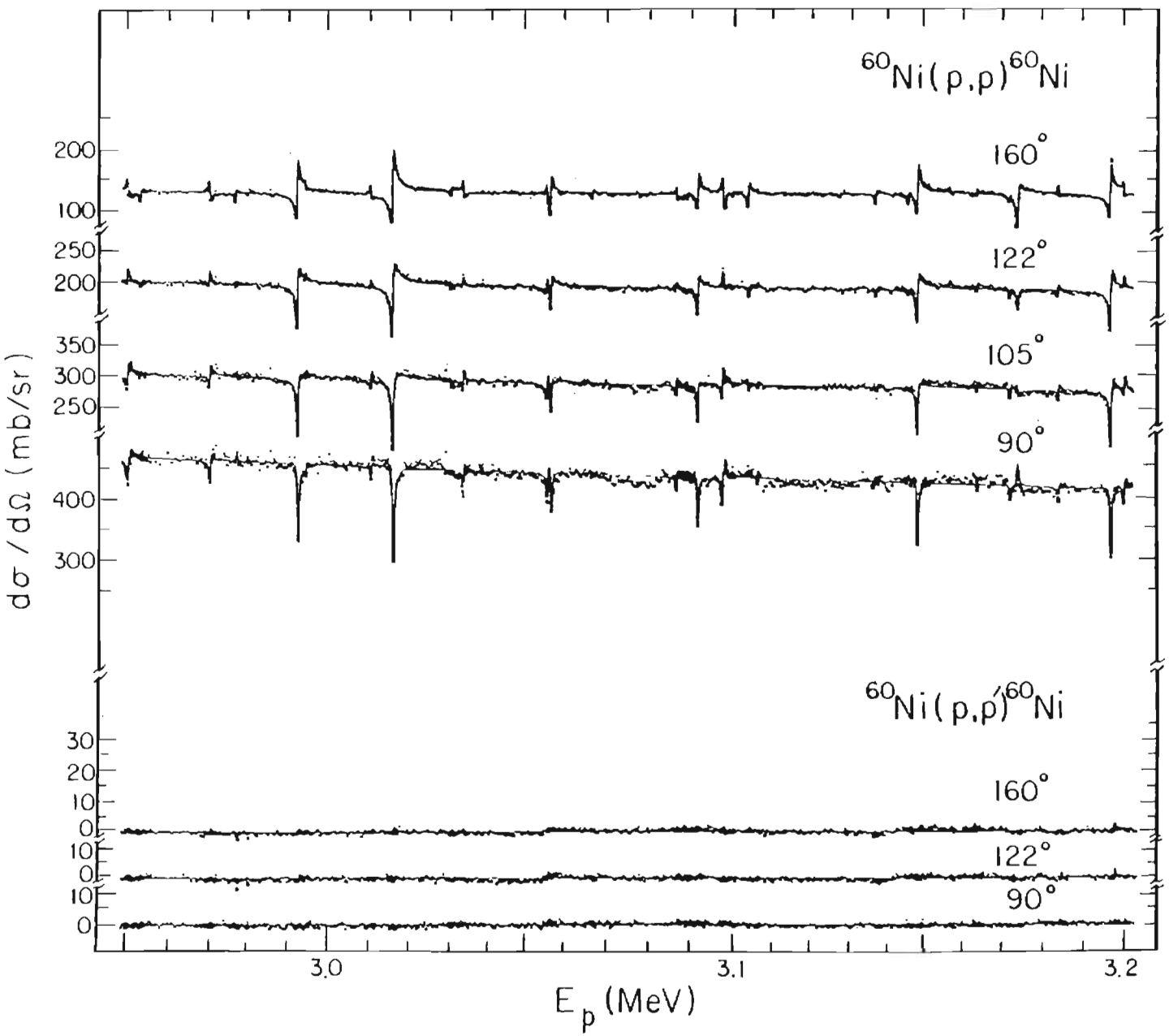
^{60}Ni(p,p)^{60}Ni
160°
122°
105°
90°
200
100
250
200
350
300
250
400
300
^{60}Ni(p,p')^{60}Ni
160°
122°
90°
30
20
10
0
10
0
10
0
dσ / dΩ (mb/sr)
3.0
3.1
3.2
E_p (MeV)

Figure 26. The $^{60}Ni(p,p)$ and $^{60}Ni(p,p')$ Differential Cross Sections from 3.20 to 3.45 MeV. The solid line represents a fit to the data.

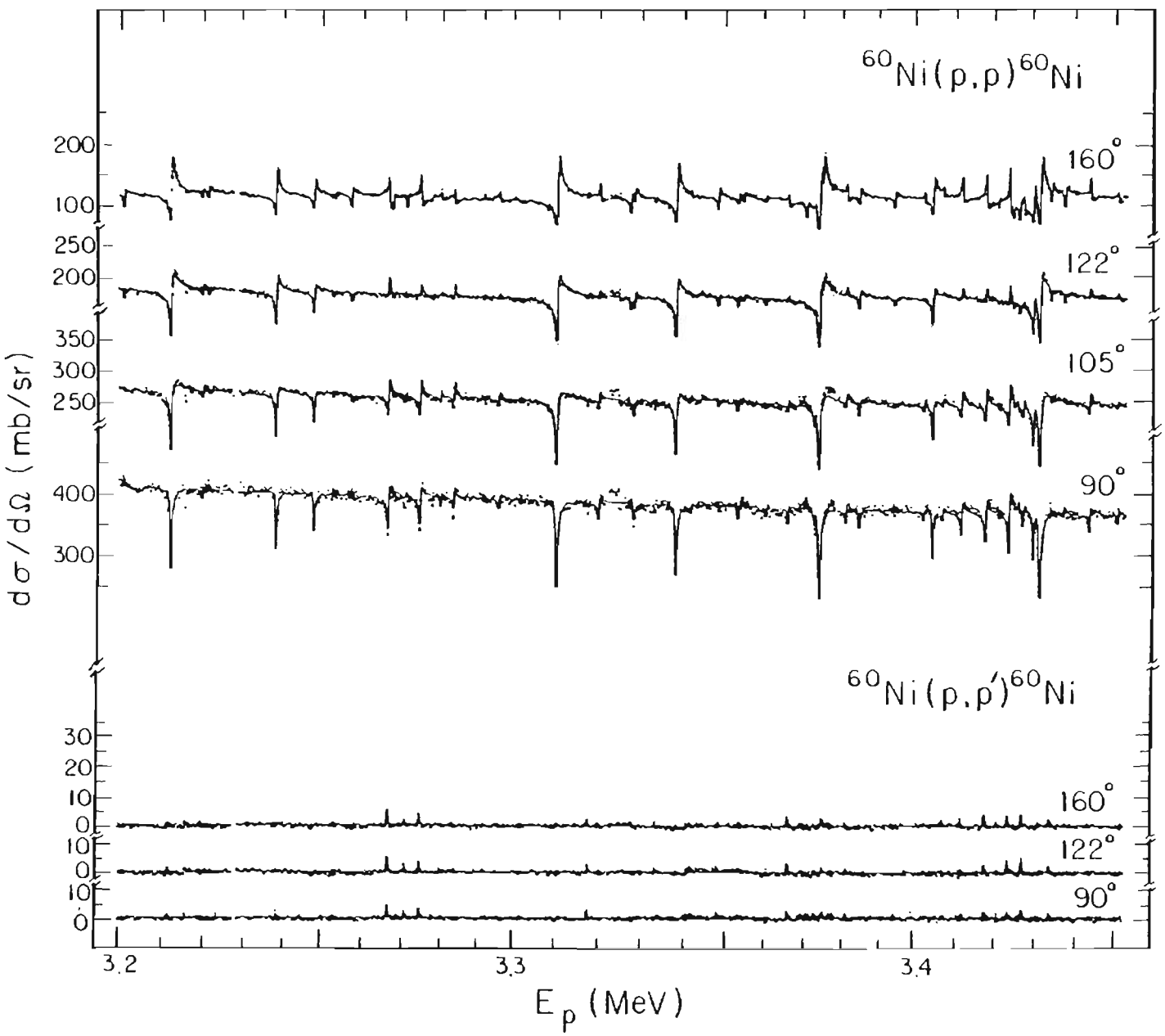
^{60}Ni(p,p)^{60}Ni
160°
122°
105°
90°
^{60}Ni(p,p')^{60}Ni
160°
122°
90°
dσ/dΩ (mb/sr)
E$_p$ (MeV)
3.2
3.3
3.4

the data and fits for ^{60}Ni(p,p) and ^{60}Ni(p,p').

The resonance parameters extracted from these data are listed in tables 4, 5, and 6, for the compound nuclei ^{55}Co, ^{59}Cu, and ^{61}Cu, respectively. In these tables Ep is the resonance energy (for the inelastic channels, orbital angular momentum and channel spin are listed instead), Γ is the laboratory width, and γ^2 is the reduced width. Due to statistical fluctuations in the data and to effects arising from the experimental resolution, there is an uncertainty in the assignment of laboratory widths; an estimate of this uncertainty is also listed. The resonance parameters are grouped by spin and parity and then ordered by resonance energy. It was possible to determine the ℓ-values of all of the resonances listed (other resonances can be seen in the data but are too small to analyze); it was not always possible to assign spins. Resonances which are marked with a star have uncertain spins. When the data gave no indication that one spin was more probable then the other, the following procedure was followed: if $\ell=1$, then J=3/2 was chosen; if $\ell=2$, then J=5/2 was chosen; if $\ell=3$, then J=5/2 was chosen; and if $\ell=4$, then J=9/2 was chosen.

The inelastic non-zero widths are also listed in tables 4, 5, and 6. Instead of listing a resonance energy, the exit orbital angular momentum and channel spin are listed. With s-wave resonances, the inelastic reduced widths were <u>assumed</u> to be equal since only the total

TABLE 4.

^{55}Co RESONANCE PARAMETERS

Ep (MeV)	Γ (eV)	γ^2 (keV)	Ep (MeV)	Γ (eV)	γ^2 (keV)
	1/2+		4.2767	1900 ± 500	3.20
			1,1.5	2300 ± 600	33.55
3.3814	145 ± 30	0.41	4.3164	2000 ± 300	3.24
3.5690	60 ± 13	0.13	4.3872	900 ± 90	1.36
2,1.5	16 ± 6	9.17	1,1.5	30 ± 10	0.34
2,2.5	16 ± 6	9.17	4.5223	1000 ± 300*	1.35
3.6806	3400 ± 200	6.39	1,1.5	70 ± 20	0.61
3.7232	310 ± 30	0.55			
3.7770	1000 ± 120	1.68		3/2−	
2,1.5	70 ± 20	18.34			
2,2.5	70 ± 20	18.34	3.2832	20 ± 10*	0.12
3.9015	1400 ± 150	2.06	3.2876	1400 ± 200	8.59
3.9890	17000 ±1700	22.96	3.3707	65 ± 15	0.35
4.0286	3500 ± 350	4.55	3.3920	450 ± 100	2.31
4.0867	19000 ±2000	23.41	1,1.5	105 ± 20	25.50
4.1207	29000 ±3000	34.66	1,2.5	22 ± 10	5.34
4.1809	2800 ± 280	3.18	3.4141	50 ± 10	0.25
4.2019	2500 ± 250	2.78	3.4426	110 ± 15	0.52
4.2295	800 ± 100	0.87	3.5026	220 ± 20	0.95
4.2868	70 ± 10	0.07	1,2.5	12 ± 3	1.83
2,1.5	12 ± 4	0.70	3.5668	475 ± 50	1.85
2,2.5	12 ± 4	0.70	3.5754	46 ± 5	0.18
4.3938	165 ± 17	0.16	1,1.5	11 ± 3	1.24
2,1.5	15 ± 4	0.67	1,2.5	4 ± 2	0.45
2,2.5	15 ± 4	0.67	3.6292	70 ± 15	0.25
4.4156	3550 ± 500	3.33	1,1.5	8 ± 3	0.74
2,1.5	80 ± 20	3.42	3.6639	120 ± 20	0.41
2,2.5	80 ± 20	3.42	1,1.5	2 ± 1	0.16
4.5273	5000 ± 700	4.32	1,2.5	10 ± 3	0.82
			3.7484	700 ± 70	2.13
	1/2−		3.8019	350 ± 50	0.99
			1,1.5	58 ± 10	2.99
3.2949	300 ± 100	1.82	3.8074	700 ± 70	1.97
3.3852	1100 ± 150	5.73	1,1.5	60 ± 10	3.04
3.4720	11000 ±1100	49.82	3.8851	500 ± 70	1.28
3.4928	4500 ± 450	19.73	1,1.5	5 ± 2	0.20
3.5653	80 ± 25	0.31	1,2.5	17 ± 4	0.68
3.6608	80 ± 15	0.27	3.9479	98 ± 15	0.23
3.8497	850 ± 80	2.27	1,1.5	38 ± 10	1.27
3.9041	500 ± 150	1.25	1,2.5	19 ± 8	0.64
1,1.5	35 ± 10	1.33	3.9692	170 ± 50	0.39
3.9442	120 ± 20*	0.29	4.0393	25 ± 10	0.05
1,1.5	10 ± 5	0.34	1,1.5	3 ± 3	0.08
4.0551	160 ± 20*	0.34	1,2.5	4 ± 3	0.10
1,1.5	64 ± 20	1.60	4.0530	180 ± 20	0.38
4.2208	4000 ± 400	7.11	1,1.5	41 ± 10	1.03
4.2642	4000 ± 700	6.81	1,2.5	4 ± 4	0.10

TABLE 4.

^{55}Co RESONANCE PARAMETERS (Continued)

Ep (MeV)	Γ (eV)	γ^2 (keV)	Ep (MeV)	Γ (eV)	γ^2 (keV)
4.1007	500 ± 70	1.01	4.0149	110 ± 20	0.73
1,1.5	26 ± 6	0.58	0,1.5	50 ± 15	0.65
1,2.5	9 ± 5	0.20	2,1.5	50 ± 15	6.13
4.1946	70 ± 20*	0.13	4.0623	450 ± 45	2.78
1,1.5	10 ± 3	0.18	0,1.5	18 ± 6	0.21
1,2.5	20 ± 5	0.35	4.1558	35 ± 10	0.19
4.2177	150 ± 15	0.27	0,1.5	5 ± 2	0.05
1,2.5	12 ± 5	0.20	2,2.5	7 ± 4	0.58
4.2500	1000 ± 150	1.73	4.2059	1100 ± 110	5.64
1,2.5	260 ± 40	4.03	0,1.5	220 ± 50	1.82
4.3039	1800 ± 200	2.95	2,2.5	60 ± 10	4.25
1,1.5	600 ± 150	8.23	4.2544	275 ± 30	1.33
1,2.5	400 ± 100	5.49	0,1.5	70 ± 15	0.52
4.3260	75 ± 20	0.12	4.2709	120 ± 60*	0.57
1,1.5	55 ± 10	0.72	0,1.5	300 ± 100	2.15
1,2.5	10 ± 5	0.13	4.3068	2600 ± 300	11.78
4.3520	550 ± 55	0.86	0,1.5	350 ± 70	2.33
4.3733	90 ± 9	0.14	4.3773	180 ± 18	0.75
4.4051	95 ± 15	0.14	4.4337	400 ± 50	1.56
1,1.5	85 ± 20	0.94	0,1.5	120 ± 30	0.62
1,2.5	30 ± 10	0.33	2,2.5	80 ± 20	3.28
4.4637	1500 ± 300	2.12	4.4643	200 ± 60*	0.75
1,1.5	10 ± 5	0.10	0,1.5	185 ± 50	0.91
1,2.5	160 ± 50	1.57	4.4693	900 ± 150*	3.38
4.5023	400 ± 50	0.55	0,1.5	200 ± 50	0.97
1,1.5	60 ± 20	0.54	2,1.5	200 ± 50	7.55
1,2.5	185 ± 50	1.68			
4.5098	100 ± 15	0.14		5/2+	
1,1.5	80 ± 20	0.71			
1,2.5	100 ± 25	0.89	3.3865	260 ± 30	4.79
			3.4186	950 ± 150	16.45
	3/2+		0,2.5	5 ± 2	0.46
			2,1.5	3 ± 2	3.36
3.4335	28 ± 8*	0.47	2,2.5	3 ± 2	3.36
3.4554	47 ± 10	0.76	3.5063	18 ± 5*	0.27
3.6507	180 ± 20	2.05	0,2.5	3 ± 1	0.19
0,1.5	5 ± 2	0.19	3.5826	80 ± 10	1.02
3.7556	20 ± 8	0.19	3.6443	195 ± 20	2.25
2,2.5	28 ± 8	7.92	0,2.5	18 ± 4	0.69
3.9417	45 ± 15*	0.33	3.6911	150 ± 20	1.60
0,1.5	20 ± 10	0.31	0,2.5	8 ± 3	0.26
2,1.5	5 ± 3	0.76	3.7277	6 ± 4*	0.06
3.9708	250 ± 70*	1.75	0,2.5	4 ± 3	0.12
0,1.5	122 ± 30	1.77	3.7487	365 ± 40	3.56
2,1.5	7 ± 7	0.98	0,2.5	12 ± 3	0.33
3.9974	400 ± 40	2.70	2,2.5	1 ± 1	0.29
0,1.5	10 ± 3	0.14			

TABLE 4.

^{55}Co RESONANCE PARAMETERS (Continued)

Ep (MeV)	Γ (eV)	γ^2 (keV)	Ep (MeV)	Γ (eV)	γ^2 (keV)
3.8062	500 ± 50	4.45	4.2920	60 ± 6	0.28
0,2.5	24 ± 5	0.55	0,2.5	22 ± 5	0.15
2,1.5	9 ± 3	2.13	2,1.5	4 ± 2	0.23
3.8183	775 ± 70	6.77	2,2.5	26 ± 5	1.50
0,2.5	24 ± 5	0.53	4.3043	170 ± 50	0.77
2,1.5	25 ± 5	5.69	0,2.5	55 ± 20	0.37
3.8610	20 ± 10	0.16	4.3154	300 ± 50	1.35
2,1.5	5 ± 2	0.99	0,2.5	110 ± 30	0.72
3.8892	23 ± 10*	0.18	2,1.5	25 ± 8	1.36
0,2.5	40 ± 15	0.72	2,2.5	125 ± 30	6.80
3.8922	180 ± 20	1.41	4.3593	150 ± 20	0.64
0,2.5	43 ± 10	0.77	0,2.5	9 ± 3	0.05
2,1.5	1 ± 1	0.18	4.3977	30 ± 10*	0.12
3.9192	380 ± 35	2.87	0,2.5	18 ± 5	0.10
0,2.5	20 ± 10	0.33	2,2.5	5 ± 3	0.22
2,1.5	2 ± 2	0.33	4.4130	130 ± 50*	0.52
2,2.5	35 ± 10	5.74	0,2.5	75 ± 15	0.41
3.9244	6 ± 5*	0.04	2,1.5	20 ± 10	0.86
3.9278	8 ± 6*	0.06	2,2.5	20 ± 10	0.86
3.9603	320 ± 30	2.28	4.4403	400 ± 100	1.55
0,2.5	3 ± 3	0.04	0,2.5	180 ± 20	0.93
2,1.5	32 ± 10	4.62	2,1.5	60 ± 30	2.42
4.0114	1200 ± 120	7.95	2,2.5	170 ± 60	6.85
0,2.5	60 ± 15	0.78	4.4449	110 ± 12	0.42
2,1.5	40 ± 15	4.99	2,1.5	15 ± 5	0.60
2,2.5	50 ± 15	6.19	2,2.5	15 ± 5	0.60
4.0727	700 ± 100	4.27	4.4741	20 ± 10*	0.07
0,2.5	40 ± 10	0.45	2,1.5	15 ± 7	0.56
2,1.5	25 ± 6	2.59	2,2.5	15 ± 7	0.56
2,2.5	20 ± 5	2.07	4.5031	100 ± 10	0.36
4.0833	650 ± 100	3.91	0,2.5	90 ± 20	0.41
0,2.5	120 ± 30	1.31	2,1.5	45 ± 15	1.57
2,1.5	120 ± 30	12.06			
2,2.5	120 ± 30	12.06		5/2−	
4.1350	5250 ± 500	29.50			
0,2.5	170 ± 25	1.65	3.7523	15 ± 4*	0.84
2,1.5	10 ± 8	0.87	1,1.5	14 ± 4	0.85
2,2.5	35 ± 10	3.05	1,2.5	6 ± 2	0.36
4.1499	180 ± 20	0.99	3.7567	32 ± 6*	1.78
0,2.5	12 ± 5	0.11	1,1.5	95 ± 20	5.67
2,1.5	17 ± 6	1.42	3.8295	39 ± 8*	1.90
2,2.5	18 ± 6	1.50	1,1.5	43 ± 6	2.03
4.1908	15 ± 8*	0.08	1,2.5	10 ± 3	0.47
0,2.5	25 ± 8	0.21	3.8396	14 ± 4*	0.67
4.2256	30 ± 10*	0.15	1,1.5	27 ± 4	1.24
0,2.5	30 ± 15	0.24	1,2.5	8 ± 2	0.37
4.2597	275 ± 50	1.32			
0,2.5	44 ± 15	0.32			

TABLE 4.

^{55}Co RESONANCE PARAMETERS (Continued)

Ep (MeV)	Γ (eV)	γ^2 (keV)
3.8597	16 ± 4*	0.74
1,1.5	7 ± 2	0.30
1,2.5	1 ± 1	0.04
4.0947	15 ± 5*	0.47
1,1.5	15 ± 5	0.34
1,2.5	3 ± 2	0.07
4.2565	18 ± 5	0.44
1,1.5	4 ± 2	0.06
1,2.5	22 ± 7	0.34
4.3430	70 ± 7	1.50
1,2.5	7 ± 3	0.09
4.4706	60 ± 30*	1.07
1,1.5	130 ± 50	1.25
4.5138	25 ± 10	0.42
1,1.5	20 ± 10	0.18
1,2.5	45 ± 15	0.40
	$9/2^+$	
3.4666	78 ± 6	82.17
2,2.5	20 ± 4	18.08
3.4763	6 ± 2*	6.18
2,2.5	4 ± 2	3.47
4.1151	10 ± 5*	2.66
4.2375	8 ± 7*	1.70
2,2.5	10 ± 3	0.66

The estimated accuracy of the resonance energies (Ep) is ±0.002 MeV.

Below the resonance energy are listed the exit orbital angular momentum and channel spin of inelastic channels with non-zero widths.

The resonances which are marked with an asterisk have uncertain spins.

TABLE 5.

^{59}Cu RESONANCE PARAMETERS

Ep (MeV)	Γ (eV)	γ^2 (keV)
	1/2+	
3.1502	5500 ± 500	32.11
3.3865	2200 ± 200	8.44
3.5215	1400 ± 140	4.35
3.6578	6300 ± 630	16.15
3.8211	5100 ± 500	10.57
3.9708	2000 ± 200	3.48
3.9870	11800 ±1200	20.15
4.0521	235 ± 25	0.37
4.1485	25 ± 15	0.04
4.1788	2300 ± 500	3.22
	1/2−	
3.1466	250 ± 25	2.87
3.2801	250 ± 25	2.20
3.3464	80 ± 8	0.62
3.3510	350 ± 35	2.69
3.4831	120 ± 12*	0.73
3.5481	50 ± 10*	0.27
3.5811	600 ± 60	3.11
3.5861	140 ± 15	0.72
1,1.5	10 ± 4	2.37
3.6121	130 ± 13	0.64
3.7840	800 ± 80	3.06
3.8277	700 ± 70	2.51
3.8792	900 ± 90	3.01
3.8962	70 ± 15	0.23
4.0643	140 ± 30*	0.37
1,1.5	75 ± 20	3.29
4.1266	3800 ± 380	9.33
4.1442	900 ± 90	2.17
1,1.5	400 ± 80	14.00
	3/2−	
3.1652	300 ± 30	3.32
3.2095	90 ± 9	0.91
3.2409	100 ± 10	0.95
3.3631	65 ± 7	0.49
3.4003	50 ± 5	0.35
3.4513	110 ± 11	0.71
3.4774	40 ± 8	0.25
3.5066	80 ± 8	0.47
1,1.5	1 ± 1	0.33
1,2.5	4 ± 2	1.34
3.6000	190 ± 19	0.96
3.6726	73 ± 8	0.33
1,1.5	2 ± 1	0.33
1,2.5	7 ± 2	1.17
3.7203	100 ± 15	0.42
1,2.5	3 ± 2	0.42
3.7432	310 ± 40	1.26
1,2.5	20 ± 5	2.55
3.7759	45 ± 5*	0.17
3.7983	60 ± 25*	0.22
3.8914	55 ± 10	0.18
1,1.5	2 ± 1	0.15
1,2.5	6 ± 2	0.45
3.9362	130 ± 20	0.40
1,2.5	28 ± 8	1.82
3.9399	450 ± 45	1.39
1,1.5	2 ± 1	0.13
1,2.5	9 ± 2	0.58
4.0064	145 ± 20	0.41
1,1.5	2 ± 1	0.10
1,2.5	7 ± 3	0.37
4.0224	2500 ± 200	6.96
4.0431	75 ± 8	0.20
1,1.5	30 ± 6	1.40
4.1253	30 ± 10	0.07
1,1.5	10 ± 4	0.37
4.1550	60 ± 10	0.14
1,1.5	7 ± 3	0.24
1,2.5	20 ± 4	0.68
4.1816	28 ± 10	0.06
4.1894	350 ± 40	0.80
1,1.5	20 ± 6	0.62
	3/2+	
3.2627	45 ± 5	1.50
3.5889	300 ± 30	5.17
0,1.5	10 ± 4	1.02
3.6086	180 ± 18	2.99
0,1.5	75 ± 10	7.10
2,1.5	3 ± 2	3.12
3.8357	1700 ± 170	19.05
0,1.5	90 ± 30	3.72
2,1.5	10 ± 4	4.16
3.9147	1400 ± 200	13.81
0,1.5	460 ± 100	14.71
2,1.5	95 ± 25	29.64

TABLE 5.

^{59}Cu RESONANCE PARAMETERS (Continued)

Ep (MeV)	Γ (eV)	γ^2 (keV)	Ep (MeV)	Γ (eV)	γ^2 (keV)
4.0492	1000 ± 150	8.04	4.0344	2000 ± 300	16.44
0,1.5	260 ± 50	5.59	0,2.5	80 ± 20	1.79
2,1.5	20 ± 10	3.98	2,1.5	25 ± 10	5.21
4.0902	1800 ± 180	13.64	2,2.5	60 ± 15	12.51
0,1.5	40 ± 10	0.77	4.0857	500 ± 50	3.81
4.1131	40 ± 15	0.29	0,2.5	80 ± 16	1.55
0,1.5	5 ± 4	0.09	2,1.5	4 ± 3	0.71
2,2.5	15 ± 6	2.44	2,2.5	20 ± 8	3.54
4.1220	100 ± 15	0.72	4.1589	750 ± 75	5.16
0,1.5	160 ± 20	2.82	0,2.5	150 ± 40	2.40
4.1643	900 ± 100	6.15	2,1.5	30 ± 10	4.25
0,1.5	440 ± 100	6.94	2,2.5	100 ± 20	14.17
2,1.5	180 ± 40	25.10			
4.1806	1100 ± 200	7.34		5/2−	
0,1.5	660 ± 200	9.99			
2,1.5	90 ± 20	11.96	3.9998	15 ± 4	0.70
			1,1.5	2 ± 1	0.11
	5/2+		1,2.5	5 ± 3	0.27
			4.0157	31 ± 10*	1.40
3.1365	70 ± 10	3.10	1,2.5	2 ± 1	0.10
3.3665	290 ± 29	7.72	4.1083	9 ± 2*	0.35
3.3885	120 ± 40*	3.05	1,1.5	1 ± 1	0.04
0,2.5	20 ± 10	4.97	4.1405	8 ± 4	0.29
3.4817	185 ± 19	3.90	1,1.5	3 ± 1	0.11
3.5190	80 ± 8	1.57	1,2.5	3 ± 1	0.11
3.5644	230 ± 23	4.14	4.1649	45 ± 10*	1.58
3.6350	40 ± 10*	0.63	1,1.5	10 ± 3	0.33
3.6875	18 ± 5*	0.26	4.1723	40 ± 10*	1.38
0,2.5	5 ± 2	0.35	1,1.5	17 ± 5	0.55
2,1.5	1 ± 1	0.75	4.1780	32 ± 10*	1.10
2,2.5	5 ± 2	3.73	1,1.5	17 ± 5	0.54
3.7523	1700 ± 200	21.91			
0,2.5	105 ± 20	5.79		9/2+	
2,1.5	44 ± 10	25.24			
2,2.5	115 ± 20	65.98	3.4750	15 ± 5*	20.27
3.7857	600 ± 60	7.31	2.2.5	1 ± 1	1.92
3.8910	65 ± 10	0.67	3.5464	35 ± 8*	39.69
3.9381	400 ± 40	3.80			
0,2.5	10 ± 3	0.30			
2,1.5	2 ± 1	0.58			
2,2.5	10 ± 3	2.88			
3.9877	200 ± 40	1.76			
0,2.5	10 ± 4	0.26			
2,1.5	2 ± 2	0.49			
2,2.5	6 ± 3	1.46			

See footnotes for table 4.

TABLE 6.

^{61}Cu RESONANCE PARAMETERS

Ep (MeV)	Γ (eV)	γ^2 (keV)	Ep (MeV)	Γ (eV)	γ^2 (keV)
	1/2+			3/2−	
2.9928	250 ± 30	1.93	3.0314	15 ± 5*	0.21
3.0167	400 ± 35	2.93	3.1058	55 ± 8	0.66
3.0567	115 ± 10	0.78	3.2246	20 ± 8	0.19
3.0932	110 ± 10	0.69	3.2594	45 ± 8	0.40
3.1479	180 ± 20	1.02	3.3299	50 ± 8	0.38
3.1710	20 ± 8	0.11	3.3516	50 ± 5	0.37
3.1959	270 ± 20	1.39	3.3778	65 ± 8	0.46
3.2150	350 ± 30	1.74	3.4341	55 ± 6	0.35
3.2229	22 ± 10	0.11	1,1.5	2 ± 1	0.52
3.2405	175 ± 20	0.83	1,2.5	4 ± 2	1.04
3.2501	95 ± 10	0.44			
3.3115	450 ± 40	1.89		3/2+	
3.3308	40 ± 5	0.16			
3.3413	280 ± 28	1.12	2.9503	55 ± 8	3.64
3.3567	25 ± 4	0.10	2.9710	65 ± 10*	4.08
3.3636	15 ± 5	0.06	3.0557	56 ± 15	2.84
3.3770	550 ± 50	2.08	3.0880	35 ± 10*	1.65
3.3863	65 ± 6	0.24	3.0994	80 ± 10	3.66
3.4046	145 ± 15	0.52	3.1992	45 ± 6	1.63
3.4297	165 ± 15	0.57	3.2688	115 ± 10	3.58
3.4314	500 ± 45	1.73	0,1.5	15 ± 5	3.58
			2,1.5	1 ± 1	2.81
	1/2−				
				5/2+	
2.9535	45 ± 15*	0.76			
2.9773	45 ± 15*	0.71	2.9509	12 ± 6*	0.79
3.1002	50 ± 10*	0.61	2.9949	11 ± 5*	0.65
3.1375	50 ± 10*	0.56	3.0112	23 ± 7*	1.30
3.1455	45 ± 8*	0.50	3.0347	28 ± 8*	1.50
3.1730	340 ± 35	3.54	3.1832	12 ± 6*	0.45
3.2033	60 ± 8	0.59	3.2769	60 ± 8	1.84
3.2698	50 ± 8	0.43	0,2.5	7 ± 3	1.61
3.2733	50 ± 8	0.43	3.2820	15 ± 4*	0.45
3.3089	25 ± 20*	0.20	3.2853	20 ± 8*	0.60
3.3580	30 ± 10*	0.22	3.2970	17 ± 8*	0.50
3.3737	70 ± 12	0.50	3.3222	25 ± 6*	0.69
3.3950	80 ± 30*	0.55	3.3449	6 ± 4	0.16
3.4209	35 ± 10*	0.23	3.3692	15 ± 4	0.38
3.4247	35 ± 10*	0.23	0,2.5	4 ± 1	0.60
3.4261	110 ± 12	0.71	2,1.5	1 ± 1	1.71
3.4375	90 ± 10	0.57	3.3759	20 ± 6*	0.50
			3.3831	30 ± 7*	0.73
			3.4025	17 ± 5*	0.40
			3.4072	15 ± 5*	0.35

TABLE 6.

^{61}Cu RESONANCE PARAMETERS (Continued)

Ep (MeV)	Γ (eV)	χ^2 (keV)
3.4119	60 ± 6	1.39
0,2.5	2 ± 1	0.25
3.4179	75 ± 8	1.71
0,2.5	4 ± 2	0.49
2,2.5	2 ± 1	2.72
3.4238	100 ± 10	2.26
0,2.5	4 ± 1	0.48
2,1.5	3 ± 1	3.98
3.4273	25 ± 5	0.56
0,2.5	4 ± 2	0.47
2,1.5	3 ± 1	3.91
3.4439	35 ± 6*	0.76
3.4508	10 ± 5*	0.21

See footnotes for table 4.

inelastic width can be determined from the data.

Brändle et al. recently have measured proton resonances in ^{55}Co (Brändle et al. 1975). A comparison of some of their resonance energies with those of the present experiment was shown in figure 15. Resonance parameters from their data agree with the present values except for the following differences. Their $(5/2^+)$ resonance at 3.4667 MeV, $1/2^+$ resonance at 4.0392 MeV, and $3/2^-$ resonance at 4.2372 MeV were found in the present experiment to be a $9/2^+$ resonance[1] at 3.4666 MeV, a $3/2^-$ resonance at 4.0393 MeV, and an $\ell=4$ resonance at 4.2375 MeV, respectively. The present experiment also gave spin assignments which did not agree with the tentative spin assignments of Brändle et al. for the small resonances at 3.4561, 4.0141, 4.2542, and 4.2907 MeV (resonance energies of Brändle et al.). Their $5/2^+$ resonance at 4.0615 MeV was determined, in the present experiment, to be a $3/2^+$ resonance at 4.0623 MeV. A $3/2^-$ resonance at 3.6654 MeV and a $(3/2^+)$ resonance at 3.6707 MeV were observed by Brändle et al.; they were not observed (well enough to analyze) in the present experiment. Ten resonances were observed in the present experiment (below 4.3 MeV) which Brändle et al. did not observe.

The $9/2^+$ isobaric analogue resonance (IAR) mentioned

---

1. This is the main fragment of an isobaric analogue resonance. A detailed discussion is presented in section IV A.

above has recently been observed by Martin et al. (1976) in the $^{54}Fe(p,\gamma)$ reaction. They quote the resonance energy as 3.468 ± 3 keV and estimate (from the (d,p) spectroscopic factor) that the elastic proton width is ~100 eV. In the present experiment, the measured proton width is (for both observed fragments of the IAR) 84 ± 8 eV; and the energy of the IAR is 3467.3 ± 2 keV.

Arai et al. recently have measured proton resonances in ^{59}Cu (Arai et al. 1976). A comparison of some of their resonance energies with those of the present experiment was shown in figure 15. The spin, parity, and elastic widths of all eight s-wave resonances observed by Arai et al. in the $^{58}Ni(p,p)$ reaction agree well with those of the present experiment, except for the small resonance they observed at 3.3900 MeV. In the present experiment this was found to be a d-wave resonance. The d-wave resonance parameters of Arai et al. agree with the present data except for the spins of two resonances and the elastic widths of four. Two g-wave resonances are observed in both experiments. In the present experiment, the observed elastic widths are one and a half times those of Arai et al. In both experiments 1 eV of inelastic width is observed on the first g-wave resonance. The present experiment revealed <u>no</u> inelastic decay on the second g-wave resonance whereas Arai et al. measured 10 eV of inelastic width. In general, the p-wave resonance parameters of Arai et al. agree poorly with the present

values.

Arai et al. also measured proton resonances in the ^{60}Ni(p,p) reaction. They did not publish s- or d-wave resonance parameters. Spins and widths of their p-wave resonances agree poorly with the present values. The resonance energies in the two experiments differ by about 2.5 keV.

In the present experiments the three sets of excitation functions that were measured overlapped those of Lindstrom (1971) and Browne (1970). Of the resonances Lindstrom observed in ^{54}Fe(p,p), the three with the highest resonance energies were also observed in the present experiment. Good agreement was obtained except for the resonance energies: Lindstrom's resonance energies were consistently 6.3 keV lower than those of the present experiment. Of the resonances Browne observed in ^{58}Ni(p,p), the five with highest resonance energies were also observed in the present experiment. Browne's resonance energies were consistently 7.4 keV lower than those of the present experiment. The $3/2^-$ doublet Browne observed at 3.158 and 3.159 MeV was observed in the present experiment as <u>one</u> $3/2^-$ resonance. Of the resonances Browne observed in ^{60}Ni(p,p), the four with the highest resonance energies were also observed in the present experiment. Browne's resonance energies were consistently 2.5 keV lower than those of the present experiment. The p-wave resonance Browne observed at 2.974 MeV was

not observed in the present experiment; the d-wave resonance observed at 2.9509 MeV in the present experiment was not observed by Browne.

CHAPTER IV

ANALYSIS

A. Isobaric Analogue Resonances

1. Background

Soon after the discovery of the neutron, Heisenberg (1932) suggested that the proton and neutron be considered two states of the same particle, the nucleon. The Pauli spin matrices ($\vec{\sigma}/2$) were adopted to describe the nucleon: the eigenvalue of the third component was +1/2 (-1/2) for a nucleon in the neutron (proton) state. This new variable was later named "isotopic spin" by Wigner (1937). The terms total isotopic spin, isobaric spin, and isospin are currently used interchangably.

The physical state of a system of A nucleons can be characterized by the projection T_3 of the total isospin $\vec{T}$ where

$$T_3 = (N-Z)/2$$

and

$$\vec{T} = \sum_{i=1}^{A} \vec{\sigma}_i / 2$$

with Z the number of protons, N the number of neutrons, and $\vec{\sigma}_i/2$ the isospin of the i^{Th} nucleon.

If the Hamiltonian of the system is charge independent, then the Hamiltonian commutes with $|\vec{T}|^2$ and the stationary states of the system can be labeled by T as well as T_3. This produces a multiplet of (2T + 1) degenerate states with T_3 ranging from -T to +T. The degeneracy among these states (isobaric analogue states) is removed by the effect of the Coulomb force and the neutron-proton mass difference. In 1937 Wigner proposed that if the energy associated with the Coulomb force were small compared to the energy associated with the nuclear force, then T should still be a good quantum number. For light nuclei this condition is true and isobaric multiplets of states are easily identified.

It was not until 1961 that Anderson and Wong discovered isobaric analogue states in medium and heavy weight nuclei through the (p,n) charge exchange reaction. The residual nucleus was left in a highly excited state (analogue state) whose quantum numbers differed from those of the target's ground state (parent state) only in having T_3 lower by one unit. The energy difference between the two states was equal to the Coulomb energy of a proton in the residual nucleus minus the neutron-proton mass difference.

Fox et al. (1964) discovered that isobaric analogue states also appear as resonances (isobaric analogue resonances or IAR) in elastic scattering. Figure 27 shows an energy level diagram of the relationship between an IAR and its parent state. T_o is the isospin of the target, ${}_Z A_N$. Since the low-lying states of most stable nuclei have $T = T_3$ and have relatively pure isospin (Bohr and Mottelson, 1969), the isospin of the parent and daughter nuclei are $T_o + 1/2$ and $T_o - 1/2$ respectively. The isospin of the IAR is, of course, $T_o + 1/2$; that of the background resonances is $T_o - 1/2$.

In 1964 Richard et al. observed an IAR in ^{92}Mo(p,p) which appeared to be composed of several resonances. This fragmentation into many resonances was first explained by Robson (1965) in terms of the mixing of the analogue-state strength through the Coulomb interaction with background resonances of the same spin and parity. Robson also predicted an asymmetric distribution of the fine-structure widths about the analogue state energy.

The fine structure of an analogue state was first fully resolved at Duke University (Keyworth et al. 1966) through high-resolution elastic scattering of protons on ^{40}Ar. Two fragmented analogue states were observed; both had asymmetric fine-structure distributions. This discovery led to the systematic study of analogue states at Triangle Universities Nuclear Laboratories via proton elastic

Figure 27. Energy Level Diagram Showing the Relationship Between an Isobaric Analogue Resonance(IAR) and its Parent State. (T_0 is the isospin of the target, ${}_Z A_N$.)

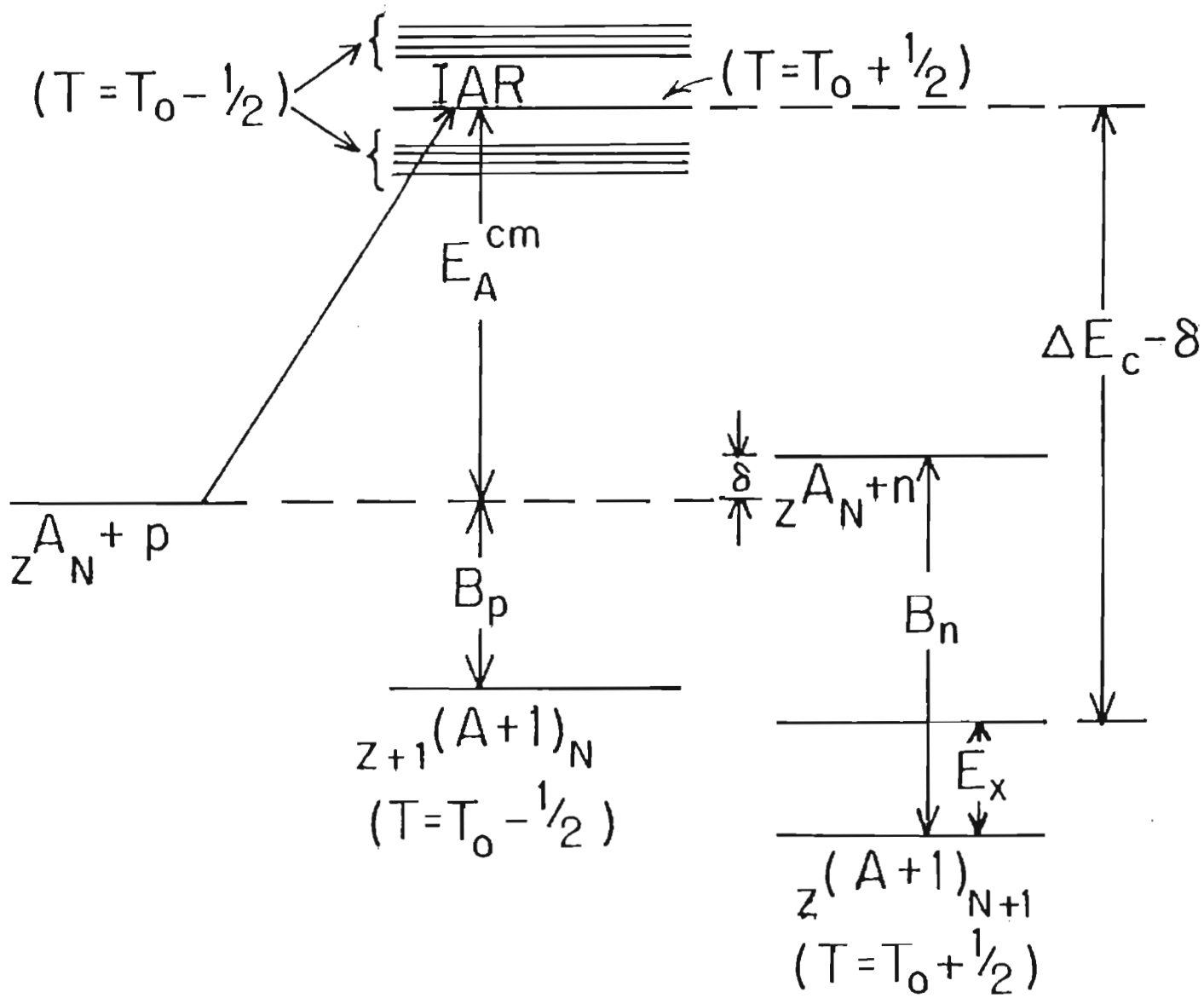

δ = neutron proton mass difference

scattering with proton energies of 1 - 3 MeV.

One of the primary purposes of the present experiment is to examine the analogue states observed in ^{54}Fe(p,p) and ^{58}Ni(p,p) at proton energies above 3 MeV (no analogue states were observed in the ^{60}Ni(p,p) data). In the rest of section III A, the identification and analysis of these analogue states is discussed.

2. Identification of IAR

a. General

The identification of an IAR is made by comparing the properties of the parent state with those of the resonance or resonances in question. The parent and analogue energies differ by the Coulomb energy of the proton (ΔE_c) minus the neutron-proton mass difference (δ). As shown in figure 27, the center of mass kinetic energy (E_A^{CM}) of the IAR is related to the excitation energy of the parent state (E_x) by

$$E_A^{CM} = \Delta E_c - B_N + E_x \qquad (1)$$

where B_N is the binding energy of the last neutron in the parent nucleus.

Studies of the parent nucleus via the (d,p) reaction provide spectroscopic factors, S_{dp}, of many of the parent states. A spectroscopic factor, S_p, can also be obtained

from the properties of an IAR:

$$S_p = (\Gamma_A / \Gamma_{sp})(2T_0 + 1) \qquad (2)$$

where T_0 is the isospin of the target, Γ_A is the elastic proton width of the analoque, and Γ_{sp} is the elastic width of a single particle resonance of the same spin, parity, and resonance energy as the IAR. Theories of IAR predict that S_{dp} and S_p are approximately the same, and the approximate equality of S_{dp} and S_p has been observed in numerous experiments. Agreement of S_{dp} and S_p is thus vital in identifying IAR.

The complexity of the compound nucleus gives rise to resonances whose positions and widths are distributed in a random manner (see section IV B). An IAR may share its strength with these "background" states. This process is an example of "line broadening" in nuclear physics (Lane 1969). Since the analogue states in this experiment consisted of at most a few resonances, the energy E_A was determined from a weighted average:

$$E_A = \left(\sum_{i=1}^{N} \Gamma_i E_i\right)\left(\sum_{i=1}^{N} \Gamma_i\right)^{-1} \qquad (3)$$

where Γ_i and E_i are the width and energy of the i^{th} fragment of the IAR and N is the number of fragments. The width of each IAR was calculated by

$$\Gamma_A = \sum_{i=1}^{N} \Gamma_i - N\langle\Gamma\rangle \qquad (4)$$

where $\langle\Gamma\rangle$ is the estimated local average width per

background resonance.

To aid in the identification of the IAR, properties of the relevant levels of the parent nucleus were listed (tables 7 and 8). The Coulomb energy for a well-known isobaric pair was used to approximately determine the expected laboratory energy of the analogues. Where parent state spectroscopic factors were available, expected analogue reduced widths (γ^2_{calc}) were estimated with equation 2. These widths were plotted as a function of the expected laboratory energy (levels with unknown spectroscopic factors are plotted as dashed lines). This plot of possible parent states was compared with cumulative sum plots of reduced widths of resonances observed in the present experiment. Figures 28 to 41 show these plots for the levels of different spin and parity observed in ^{55}Co and ^{59}Cu. A detailed discussion of each figure is given below.

b. ^{55}Co

Table 7 lists the adopted level properties of ^{55}Fe. Figure 28 shows the cumulative sum plots of $1/2^+$ resonances in ^{55}Co and the possible $1/2^+$ levels in ^{55}Fe. The resonances below 3.2832 MeV are from Lindstrom (1970); those above 4.5273 MeV are from Brändle et al. (1975). (In the following discussion, unless otherwise specified, all resonance energies are the proton laboratory energies, and

Table 7.

Adopted Level Scheme of ^{55}Fe

E_x[1] (MeV)	J^π[2]	S_{dp}[3]	E_x[1] (MeV)	J^π[2]	S_{dp}[3]
2.050	$3/2^-$	0.08	3.709[4]		
2.153	$5/2^-$	0.16	3.722[4]		
2.212			3.791	$1/2^-$	0.05
2.470	$3/2^-$	0.15	3.814	$\ell=4$ [6]	7.40[6]
2.545			3.860[4]		
2.589	$(5/2^-)$	0.05	3.904	$\ell=1$ [6]	0.07[6]
2.818			3.960[4]		
2.881			4.028	$(5/2^-)$	0.06
2.940	$(\ell=1)$ [4]	0.07[5]	4.057[4]		
2.987			4.123		
3.029	$3/2^-$	0.03	4.273		
3.076[4]			4.372[7]		
3.117			4.387[7]		
3.311[4]			4.450[8]	$1/2^+$ [8]	
3.362			4.466	$5/2^+$	0.13
3.431[4]			4.495	$\ell=1$ [4]	0.06[5]
3.469			4.538	$\ell=1$ [6]	0.09[6]
3.551	$3/2^-$	0.11	4.636[7]		
3.599[4]			4.658[7]		
3.661[4]			4.673[7]		
			4.711	$5/2^+$	0.04

1. Excitation energies are from Auble and Rapaport (1970) unless otherwise noted. (These states are shown in figures 28 to 34 and are plotted at $E_p=E_x-0.263$ MeV.)
2. Spins and parities are from Kocher and Haeberli (1972) unless otherwise noted. Parentheses indicate uncertain assignments.
3. Spectroscopic factors are from Kocher and Haeberli (1972) unless otherwise noted. If only ℓ is known, then the number quoted is $(2J+1)S$.
4. Sperduto and Rapaport (1961)
5. Sperduto and Rapaport (1961). Since only $(2J+1)\gamma$ was given, $(2J+1)S$ was estimated by normalizing to the 3.923 MeV level of Fulmer and McCarthy where both $(2J+1)S$ and $(2J+1)\gamma$ were given.
6. Fulmer and McCarthy (1963)
7. Sperduto and Buechner (1964)
8. Sherr et al. (1965)

Figure 28. Cumulative Sums of the Elastic and Inelastic Reduced Widths of $1/2^+$ Levels in ^{55}Co. Possible parent states are indicated at the bottom. Dashed lines indicate levels with unknown spectroscopic factors. A discussion of this figure is contained in the text.

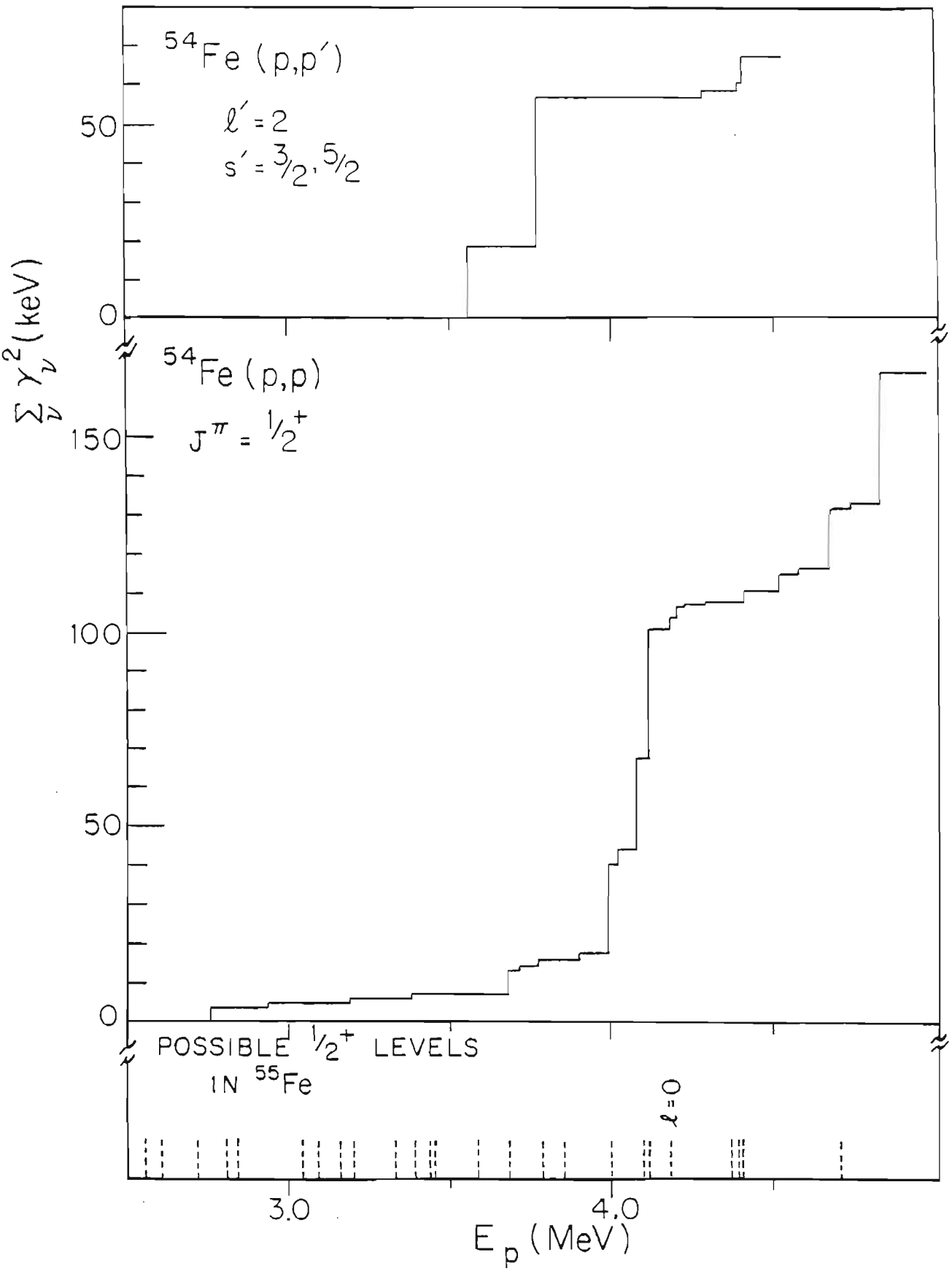
^{54}Fe (p,p′)
ℓ′ = 2
s′ = 3/2, 5/2
50
0
^{54}Fe (p,p)
$J^\pi = 1/2^+$
150
100
50
0
$\sum_\nu \gamma_\nu^2$ (keV)
POSSIBLE $1/2^+$ LEVELS
IN ^{55}Fe
ℓ = 0
3.0
4.0
E_p (MeV)

all parent state energies are the excitation energies.)

The $1/2^+$ strength is dominated by a cluster of resonances near E_p = 4.08 MeV. Brändle et al. (1975) identify this cluster as the analogue of the ℓ=0 level at 4.45 MeV in ^{55}Fe. Several questions arise concerning the indentification of this s-wave structure as an IAR. These questions are discussed in section IV C; the evidence suggests that this structure is not an analogue state but is probably a (2p - 1h) doorway state. Nevertheless, Coulomb energies and spectroscopic factors were determined and are presented in sections IV A 3 and IV A 4, respectively.

Figure 29 shows the cumulative sum plots of $1/2^-$ resonances in ^{55}Co and the possible $1/2^-$ levels in ^{55}Fe. The resonances below 3.2832 MeV are from Lindstrom (1970)[1]. The two $1/2^-$ resonances at 3.4720 and 3.4982 MeV are identified as the IAR associated with the $1/2^-$ parent state at 3.791 MeV excitation energy. Energies and spectroscopic factors are consistent and will be presented later.

No other analogue states can be positively identified in the present $1/2^-$ or $3/2^-$ data of ^{55}Co. However, several other parent states are known, and several anomalously large elastic and inelastic widths are apparent in the cumulative sum plots (figures 29 and 30). One possible

---

1. A resonance at 2.7509 MeV was misassigned as $1/2^-$. This resonance is considered a $3/2^-$ with width γ^2 = 5.89 keV throughout the present analysis.

Figure 29. Cumulative Sums of the Elastic and Inelastic Reduced Widths of $1/2^-$ Levels in ^{55}Co. Possible parent states are indicated at the bottom. Dashed lines indicate levels with unknown spectroscopic factors. A discussion of this figure is contained in the text.

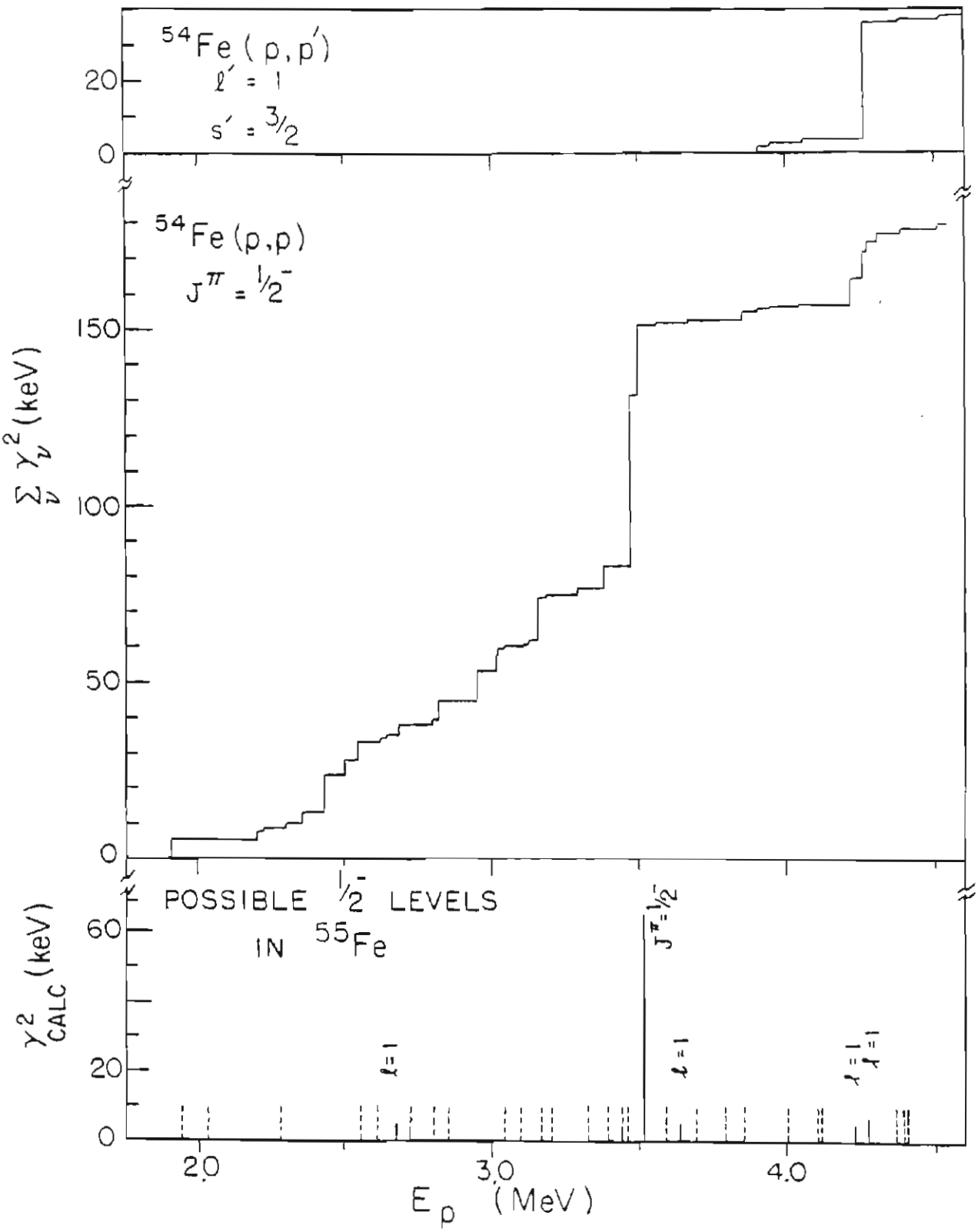
^{54}Fe (p, p′)
ℓ′ = 1
s′ = 3/2
^{54}Fe (p,p)
$J^\pi = 1/2^-$
$\sum_\nu \gamma_\nu^2$ (keV)
POSSIBLE $1/2^-$ LEVELS
IN ^{55}Fe
γ^2_{CALC} (keV)
$J^\pi = 1/2^-$
ℓ=1
ℓ=1
ℓ=1
ℓ=1
E_p (MeV)

explanation of these data is presented in the next few pages.

Strengths and energies are consistent if the $1/2^-$ resonance at 2.6854 MeV is identified as the analogue of the ^{55}Fe level at 2.940 MeV. Unfortunately the average reduced width is too large and a positive identification cannot be made.

No $1/2^-$ resonances were observed in the region where an analogue of the $\ell=1$ state at 3.904 MeV is expected.

The $\ell=1$ states located at 4.495 and 4.538 MeV in ^{55}Fe may be the parents of the 4.2208 and 4.2642 MeV resonances, respectively. This is very tentative because of the close proximity of the strong $1/2^-$ resonance at 4.2767, and the $3/2^-$ resonances at 4.2500 and 4.3039 MeV. A study of the excitation energies and inelastic strengths (see below) suggests that the $1/2^-$ resonance at 4.2767 and the $3/2^-$ resonance at 4.3039 are also IAR.

Figure 30 shows the cumulative sum plots of $3/2^-$ resonances in ^{55}Co and possible $3/2^-$ levels in ^{55}Fe. The resonances below 3.2832 MeV are from the results of Lindstrom (1970) (see footnote on previous page). In this earlier work, four IAR were identified below 3.3 MeV; they are apparent in figure 30.

No $3/2^-$ resonance is observed which can be identified as the analogue of the $\ell=1$ parent state at 3.904 MeV. (Recall that no $1/2^-$ resonance was observed either.) The

Figure 30. Cumulative Sums of the Elastic and Inelastic Reduced Widths of $3/2^-$ Levels in ^{55}Co. Possible parent states are indicated at the bottom. Dashed lines indicate levels with unknown spectroscopic factors. A discussion of this figure is contained in the text.

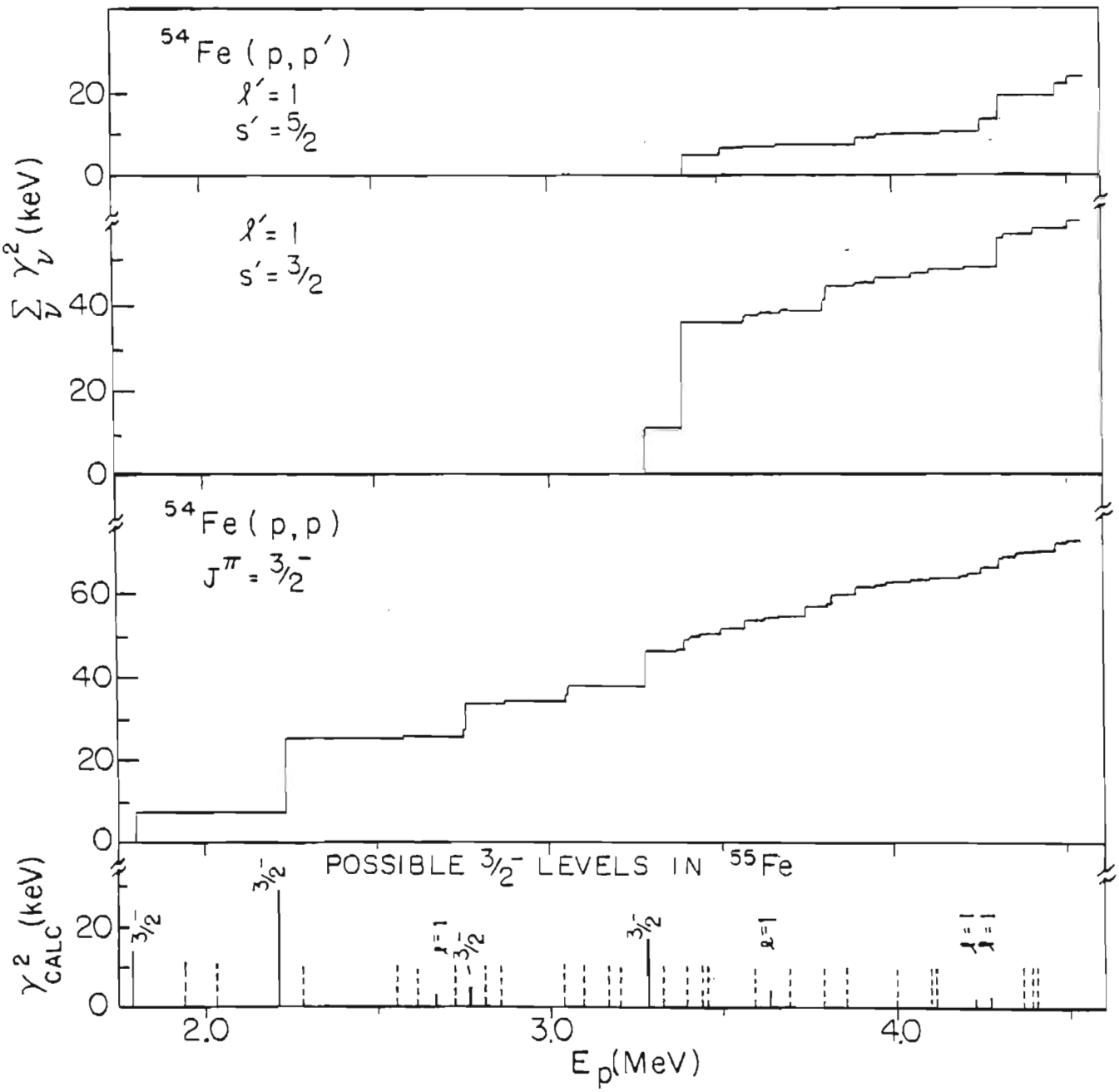
^{54}Fe (p, p′)
ℓ′ = 1
s′ = 5/2
ℓ′ = 1
s′ = 3/2
^{54}Fe (p, p)
$J^{\pi} = 3/2^-$
$\sum_\nu \gamma_\nu^2$ (keV)
POSSIBLE $3/2^-$ LEVELS IN ^{55}Fe
γ^2_{CALC} (keV)
E_p(MeV)

expected IAR width (γ^2_{calc}) would suggest that $\gamma^2 \sim \langle \gamma^2 \rangle$ and thus the IAR could be lost in the background.

The cumulative sum plots of inelastic reduced widths of $\ell = 1$ resonances (figures 29 and 30) show several resonances with large inelastic widths. Of course, large inelastic widths can occur by chance. The likelihood of the larger observed resonances occurring by chance was examined (see section IV B 2): it is improbable that reduced widths larger than $\sim$3 keV occur by chance. Except for the $3/2^-$ IAR at 3.2876 MeV the $\ell = 1$ resonances with large inelastic widths do not appear to be IAR. However, some IAR are observed strongly in the (p,p') reaction and weakly, or not at all, in the (p,p) or (d,p) reactions (e.g., Jones, Lane, and Morrison 1964). Assuming a single particle state and the "weak coupling" picture[1], there is a state whose excitation is above that of the single particle state by just the core excitation energy (ΔE_χ); a large component of the wave function of this state is a single particle coupled to an excited core configuration. This single particle $\otimes$ excited core configuration leads to a strong inelastic-proton decay of the corresponding analogue state. Although the lower p-wave states in ^{55}Fe are certainly not pure single particle states, states with reasonably large

1. See Temmer (1969) for an extensive discussion. Several references to experiments which confirm the existence of the phenomenon are given there.

spectroscopic factors have been observed as IAR in ^{55}Co.

For ^{54}Fe the first excited state (2^+) has an energy of 1.4077 MeV. Thus IAR with large inelastic widths might be found at an energy 1.4 MeV higher than the IAR which have been observed in the elastic channel. Assuming Lindstron's $1/2^-$ resonance at 2.6854 MeV is the analogue of the parent at 2.940 MeV, then Lindstrom's p-wave analogues are at proton energies of 1.8017, 2.2431, 2.6854, and 2.7509 MeV. The p-wave resonances with large inelastic widths have proton energies of 3.3920, 3.8019, 3.8074, 4.2767, and 4.3039 MeV. Assuming the resonances at 3.8019 and 3.8074 MeV are two fragments of an IAR at E_A = 3.8056, the four resonances with large inelastic widths are located 1.561, 1.534, 1.562, and 1.525 MeV above the four IAR (corrected to center of mass). The approximate equality of these separation energies suggests that the resonances with large inelastic widths are indeed analogue states. However, even if these resonances are analogue states, the parent states do not necessarily have large single particle spectroscopic factors and thus may be very difficult to identify. The non-stripping states of ^{55}Fe at 3.661 and 4.057 MeV yield reasonable values for the Coulomb energies if these states are identified as the parents of the resonances at 3.3920 and 3.8019 MeV, respectively; the Coulomb energies are listed in section IV A 3.

This discussion is presented merely as a possible

explanation of the anomalously large inelastic strength. Since the original low-lying parent states are already complicated, the applicability of the weak coupling picture is in doubt. Even though these assignments are obviously quite tentative, spectroscopic factors and Coulomb energies were determined and are presented in section IV A 4 and IV A 5.

Figure 31 shows the cumulative sum plots of $3/2^+$ resonances in ^{55}Co and the possible $3/2^+$ levels in ^{55}Fe. No $3/2^+$ analogues are identified for ^{55}Co.

Figure 32 shows the cumulative sum plots of $5/2^+$ resonances in ^{55}Co and the possible $5/2^+$ levels in ^{55}Fe. The two $5/2^+$ resonances at 4.1350 and 4.1499 MeV are considered fragments of the IAR of the parent state at 4.466 MeV. No IAR was observed for the parent at 4.711 MeV. The analogue may be beyond the energy range of this experiment.

Figure 33 shows the cumulative sum plots of $5/2^-$ (and $7/2^-$) resonances and the possible $\ell=3$ levels in ^{55}Fe. The analogue of the $\ell=3$ parent state at 4.028 MeV is evident in the figure. Since the estimated reduced width (γ^2_{calc}) is very nearly equal to the sum of the elastic reduced widths of the resonances at 3.7523, 3.7567, 3.8295, 3.8369, and 3.8597 MeV and since no other resonances are observed nearby, it is assumed that all five resonances are part of the analogue state. For each fragment the s' = 3/2

Figure 31. Cumulative Sums of the Elastic and Inelastic Reduced Widths of $3/2^+$ Levels in ^{55}Co. Possible parent states are indicated at the bottom. Dashed lines indicate levels with unknown spectroscopic factors. A discussion of this figure is contained in the text.

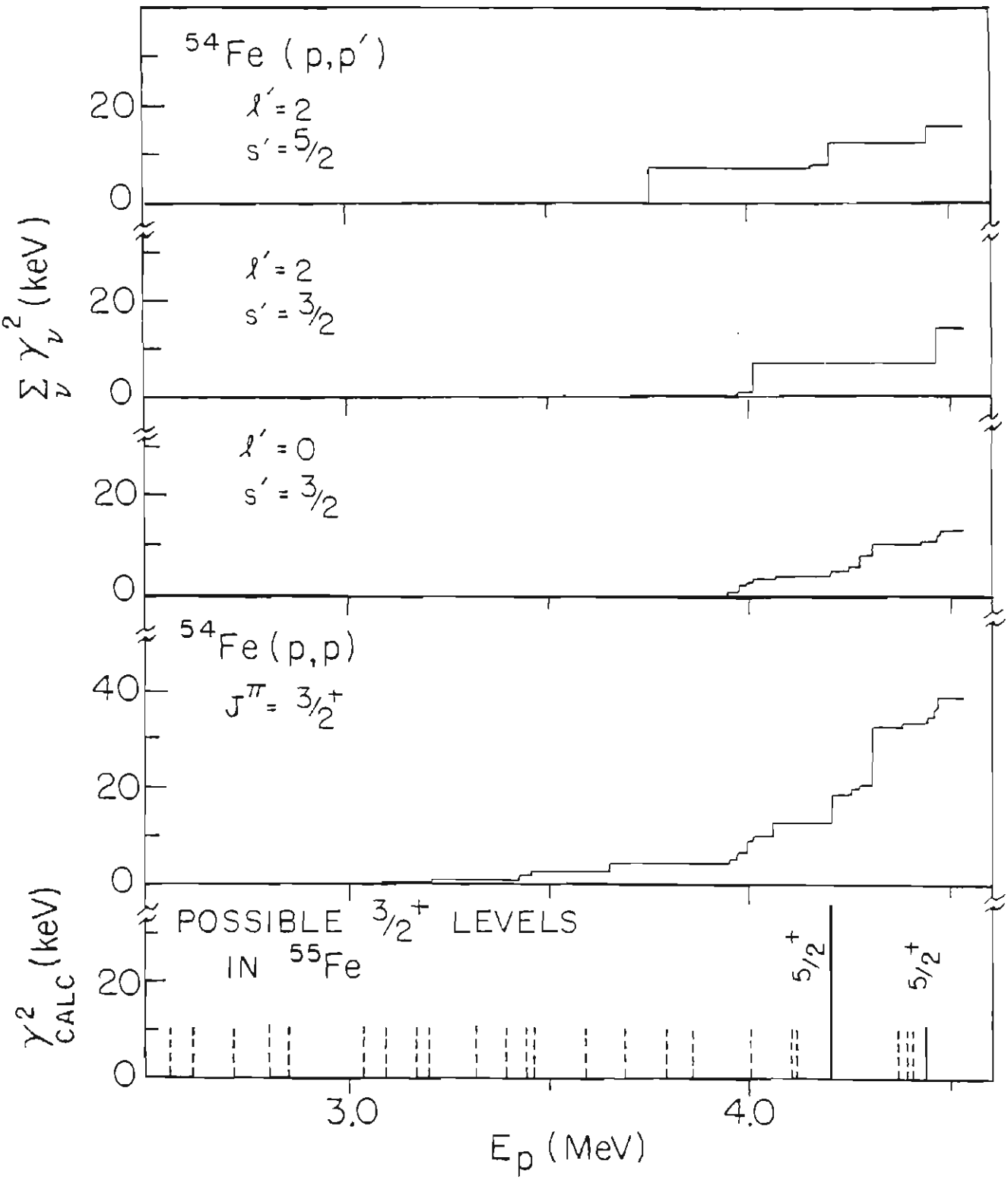
^{54}Fe (p,p′)
ℓ′ = 2
s′ = 5/2
ℓ′ = 2
s′ = 3/2
ℓ′ = 0
s′ = 3/2
^{54}Fe (p,p)
J^{π} = 3/2^{+}
POSSIBLE 3/2^{+} LEVELS
IN ^{55}Fe
5/2^{+}
5/2^{+}
$\sum_{\nu} \gamma_{\nu}^{2}$ (keV)
γ^{2}_{CALC} (keV)
0
20
40
3.0
4.0
E_p (MeV)

Figure 32. Cumulative Sums of the Elastic and Inelastic Reduced Widths of $5/2^+$ Levels in ^{55}Co. Possible parent states are indicated at the bottom. Dashed lines indicate levels with unknown spectroscopic factors. A discussion of this figure is contained in the text.

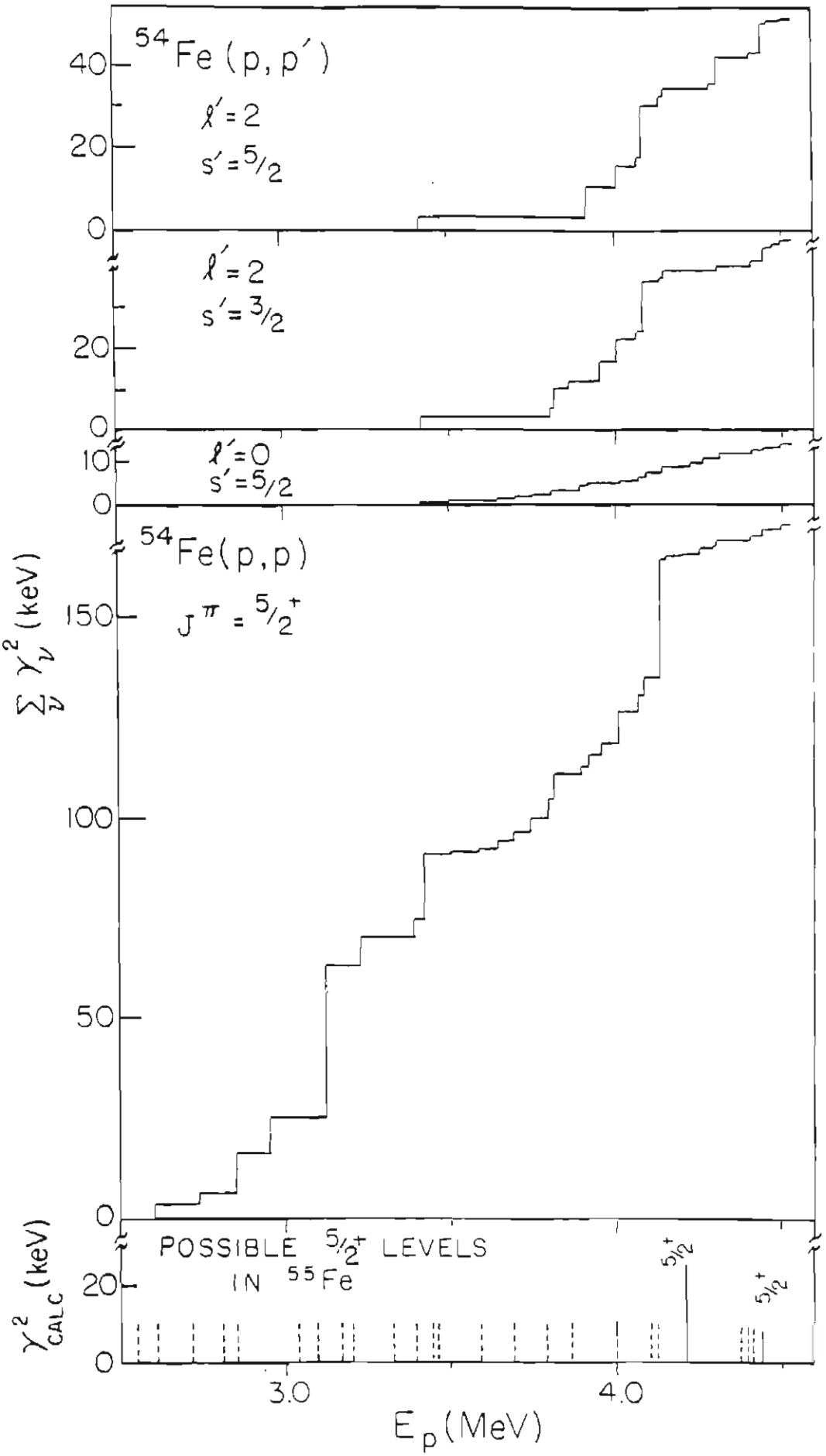
^{54}Fe (p, p′)
ℓ′ = 2
s′ = 5/2
ℓ′ = 2
s′ = 3/2
ℓ′ = 0
s′ = 5/2
^{54}Fe(p,p)
$J^{\pi} = 5/2^{+}$
$\sum_{\nu} \gamma_{\nu}^{2}$ (keV)
POSSIBLE $5/2^{+}$ LEVELS
IN ^{55}Fe
$5/2^{+}$
$5/2^{+}$
γ^{2}_{CALC} (keV)
E_p (MeV)

Figure 33. Cumulative Sums of the Elastic and Inelastic Reduced Widths of $5/2^-$ (and $7/2^-$) Levels in ^{55}Co. Possible parent states are indicated at the bottom. Dashed lines indicate levels with unknown spectroscopic factors. A discussion of this figure is contained in the text.

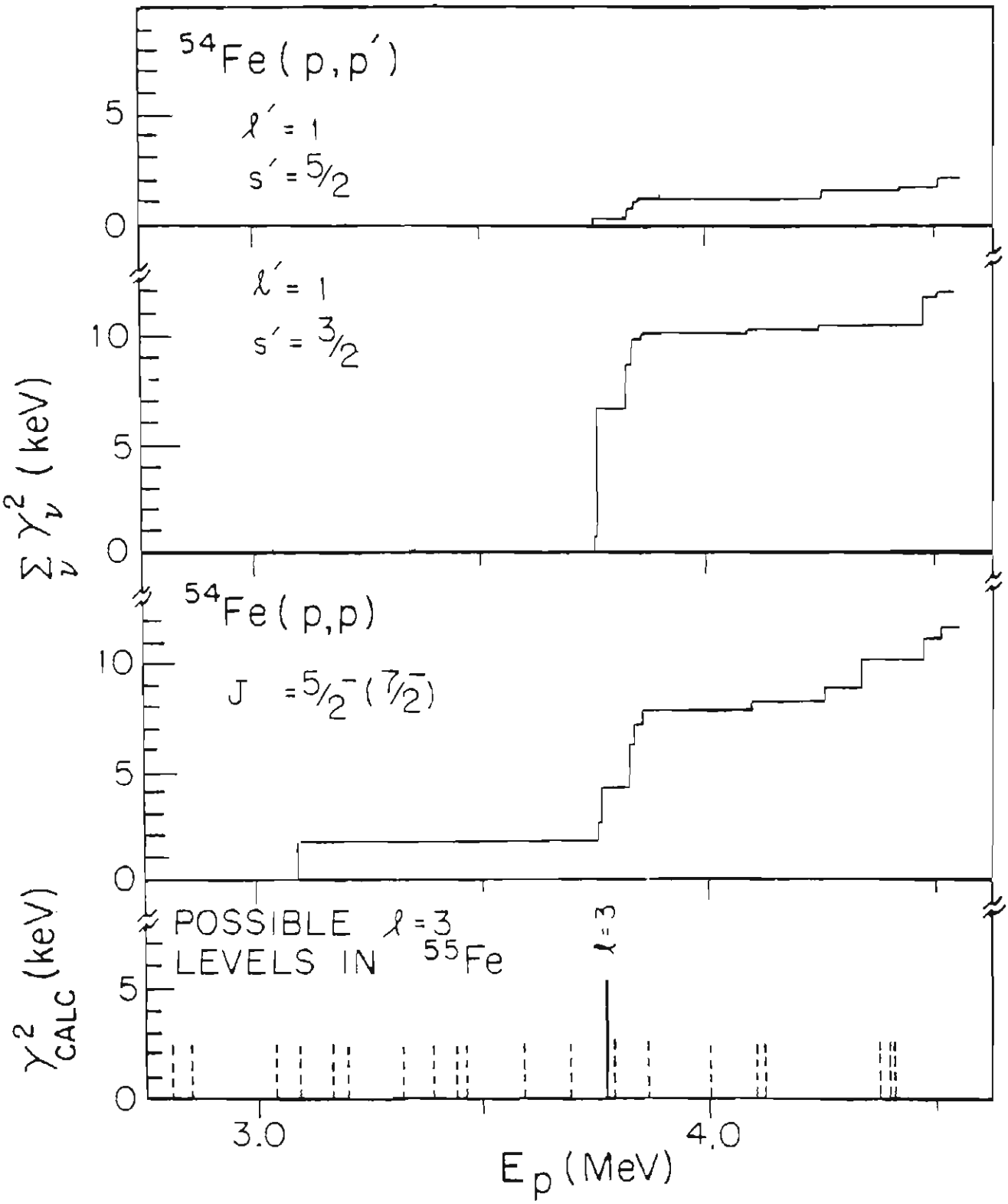
^{54}Fe (p, p′)
ℓ′ = 1
s′ = 5/2
ℓ′ = 1
s′ = 3/2
$\sum_\nu \gamma_\nu^2$ (keV)
^{54}Fe (p, p)
J = 5/2⁻ (7/2⁻)
POSSIBLE ℓ = 3
LEVELS IN ^{55}Fe
ℓ=3
γ^2_{CALC} (keV)
3.0
4.0
E_p (MeV)

reduced width is consistently larger than the s' = 5/2 width. Although this could be true of a $5/2^-$ IAR, it would necessarily be true of a $7/2^-$ IAR that was misassigned as a $J^\pi = 5/2^-$ (i.e., the inelastic angular distributions were all high at 160° and low at 90°, suggesting, but not requiring, that the resonances have $J^\pi = 7/2^-$). On the other hand Kocher and Haeberli (1972) tentatively assign the parent state spin as $5/2^-$. The $5/2^-$ spin assignment is tentatively adopted but should be considered suspect.

Figure 34 shows the cumulative sum plots of $9/2^+$ (and $7/2^+$) resonances and the possible $\ell=4$ levels in ^{55}Fe. The two $9/2^+$ resonances at 3.4666 and 3.4763 MeV are identified as fragments of the analogue of the $\ell=4$ parent state at 3.814 MeV.

c. ^{59}Cu

The adopted level properties of ^{59}Ni are listed in table 8. Figure 35 shows the cumulative sum plots of $1/2^+$ resonances in ^{59}Cu and the possible $1/2^+$ levels in ^{59}Ni. (In all of the cumulative sum plots for ^{59}Cu the data for resonances below 3.1285 MeV are from Browne (1970).) One IAR is expected but the average reduced width of the background resonances is much larger than the estimated reduced width (γ^2_{calc}) and the IAR cannot be identified.

Figure 36 shows the cumulative sum plots of $1/2^-$

Figure 34. Cumulative Sums of the Elastic and Inelastic Reduced Widths of $9/2^+$ (and $7/2^+$) Levels in ^{55}Co. Possible parent states are indicated at the bottom. Dashed lines indicate levels with unknown spectroscopic factors. A discussion of this figure is contained in the text.

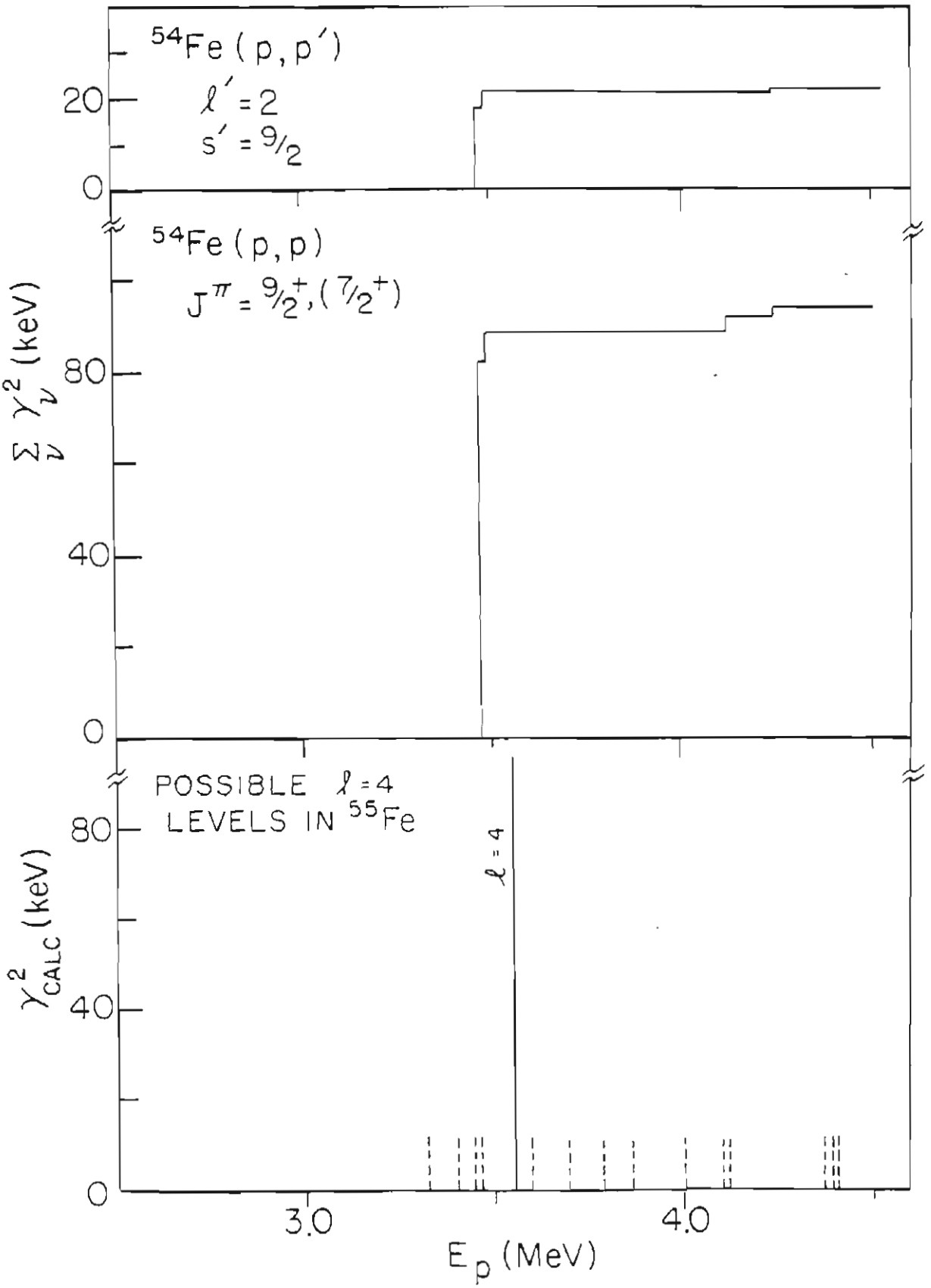
^{54}Fe (p, p′)
$\ell' = 2$
$s' = 9/2$
20
0
^{54}Fe (p, p)
$J^\pi = 9/2^+, (7/2^+)$
$\sum_\nu \gamma_\nu^2$ (keV)
80
40
0
POSSIBLE $\ell = 4$
LEVELS IN ^{55}Fe
$\ell = 4$
γ^2_{CALC} (keV)
80
40
0
3.0
4.0
E_p (MeV)

Table 8.

Adopted Level scheme of ^{59}Ni

E_x[1] (MeV)	J^π[2]	S_{dp}[3]	E_x[1] (MeV)	J^π[2]	S_{dp}[3]
1.303	$1/2^-$	0.230	3.127		
1.339			3.179	$3/2^-$ [7]	0.016[6]
1.680			3.297		
1.687	$5/2^-$	0.110	3.308		
1.735	(ℓ=1) [4]	0.031[4]	3.324		
1.746			3.340		
1.778			3.377	ℓ=2 [4]	0.011[4]
1.949	$7/2^-$ [5]		3.389		
2.413	ℓ=2 [6]	0.104[6]	3.419	$1/2^+$ [4]	0.023[4]
2.421	$3/2^-$ [7]	0.008[4]	3.447		
2.533	ℓ=1 [8]		3.463	$3/2^-$	0.031
2.630	$7/2^-$ [5]	0.038[4]	3.463	ℓ=3 [9]	
2.630	(ℓ=1) [6]	0.067[6]	3.515[6]		
2.705	$7/2^-$ [5]		3.531[6]		
2.900	$3/2^-$ [7]	0.002	3.544[6]	$5/2^+$	0.023
3.036	$1/2^-$ [5]	0.016[4]	3.573[6]	ℓ=1 [6]	0.025[6]
3.047	ℓ=3 [5]		3.600[6]		
3.062	$9/2^+$ [8]	0.470			

1. Excitation energies are from Vervier (1968) unless otherwise noted. (These states are shown in figures 35 to 41 and are plotted at $E_p = E_x + 0.559$ MeV.)
2. Spins and parities are from Aymar et al. (1973) unless otherwise noted. Parentheses indicate uncertain assignments.
3. Spectroscopic factors are from Aymar et al. (1973) unless otherwise noted. If only ℓ is known, then the value quoted is $(2J + 1)S$.
4. Fulmer et al. (1964)
5. Chowdhury and Gupta (1973)
6. Cosman et al. (1966)
7. Stecher-Rasmussen et al. (1972)
8. Vervier (1968)
9. Dalton et al. (1961)

Figure 35. Cumulative Sums of the Elastic and Inelastic Reduced Widths of $1/2^+$ Levels in ^{59}Cu. Possible parent states are indicated at the bottom. Dashed lines indicate levels with unknown spectroscopic factors. A discussion of this figure is contained in the text.

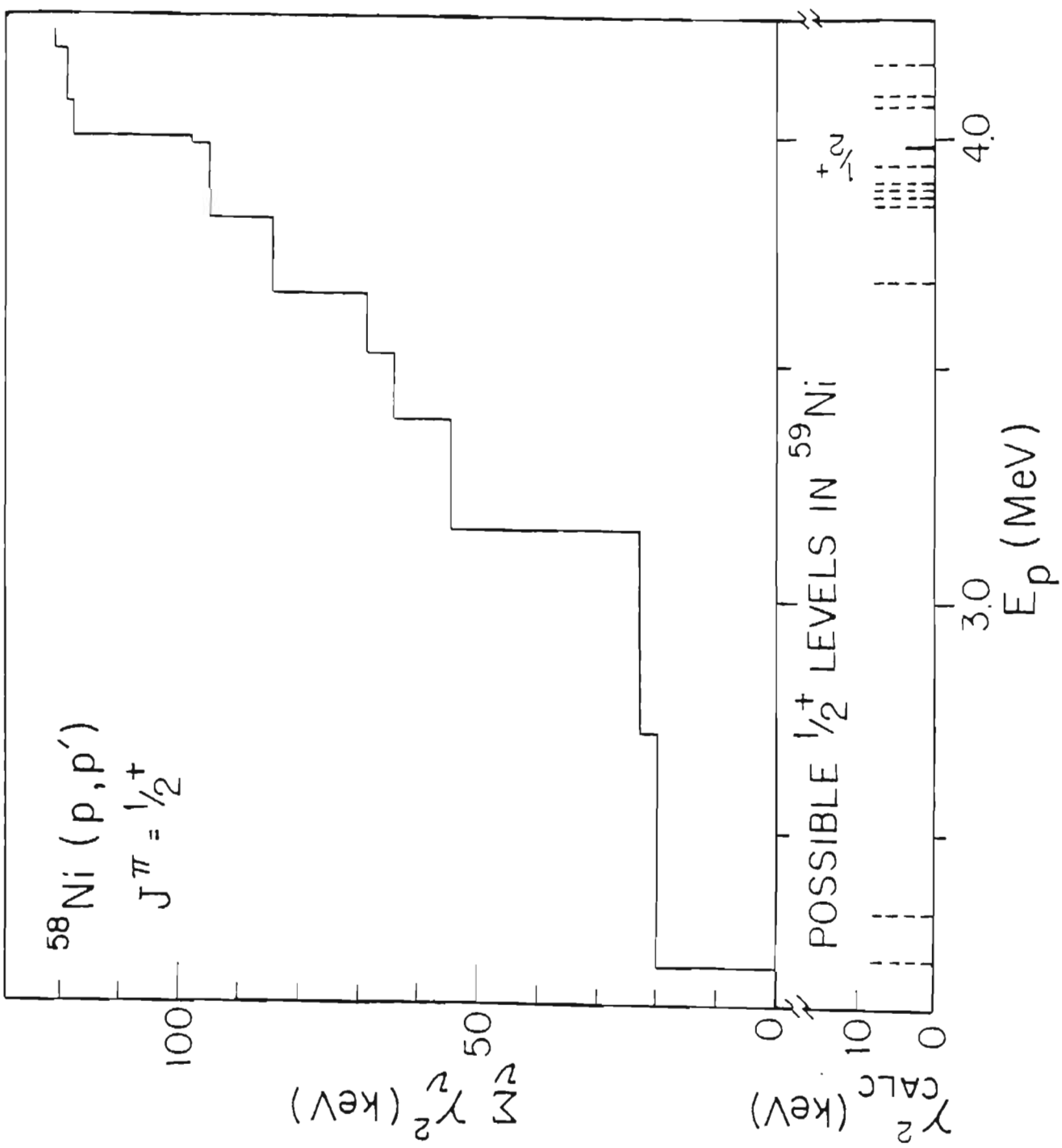
^{58}Ni (p,p′)
$J^\pi = 1/2^+$
$\sum \chi^2_\nu$ (keV)
χ^2_{CALC} (keV)
POSSIBLE $1/2^+$ LEVELS IN ^{59}Ni
E_p (MeV)
100
50
0
10
0
3.0
4.0

resonances in ^{59}Cu and possible $1/2^-$ levels in ^{59}Ni. The resonance at 1.841 MeV has been identified by Browne (1970) as the analogue of the state in ^{59}Ni at 1.303 MeV. Two other IAR are tentatively identified at 3.5811 and 4.1266 MeV; the corresponding parents are the $1/2^-$ state at 3.036 MeV and the $\ell=1$ state at 3.573 MeV.

Figure 37 shows the cumulative sum plots of $3/2^-$ resonances in ^{59}Cu and possible $3/2^-$ levels in ^{59}Ni. The resonance at 3.7432 MeV is tentatively identified as the analogue of the $3/2^-$ state in ^{59}Ni at 3.179 MeV. The resonance at 4.0224 MeV is certainly the analogue of the $3/2^-$ in ^{59}Cu at 3.463 MeV.

Figures 38 and 39 show the cumulative sum plots of $3/2^+$ and $5/2^+$ resonances, respectively, in ^{59}Cu. Several $\ell=2$ parent states are shown. The expected IAR strengths (γ^2_{calc}) are much less than the average reduced width of the background resonances for both the $3/2^+$ and $5/2^+$ resonances, and no analogues can be identified.

Figure 40 shows the cumulative sum plots of $5/2^-$ (and $7/2^-$) resonances in ^{59}Cu. The two $5/2^-$ resonances at 3.9998 and 4.0157 MeV are tentatively identified as the analogue of the $\ell=3$ state at 3.463 MeV. Positive identification is not claimed since apparently only one group of experimentalists (Dalton et al., 1961) have observed the parent state, and the parent spectroscopic factor is unknown. The appreciable f-wave strength near 4.17 MeV is

Figure 36. Cumulative Sums of the Elastic and Inelastic Reduced Widths of $1/2^-$ Levels in ^{59}Cu. Possible parent states are indicated at the bottom. Dashed lines indicate levels with unknown spectroscopic factors. A discussion of this figure is contained in the text.

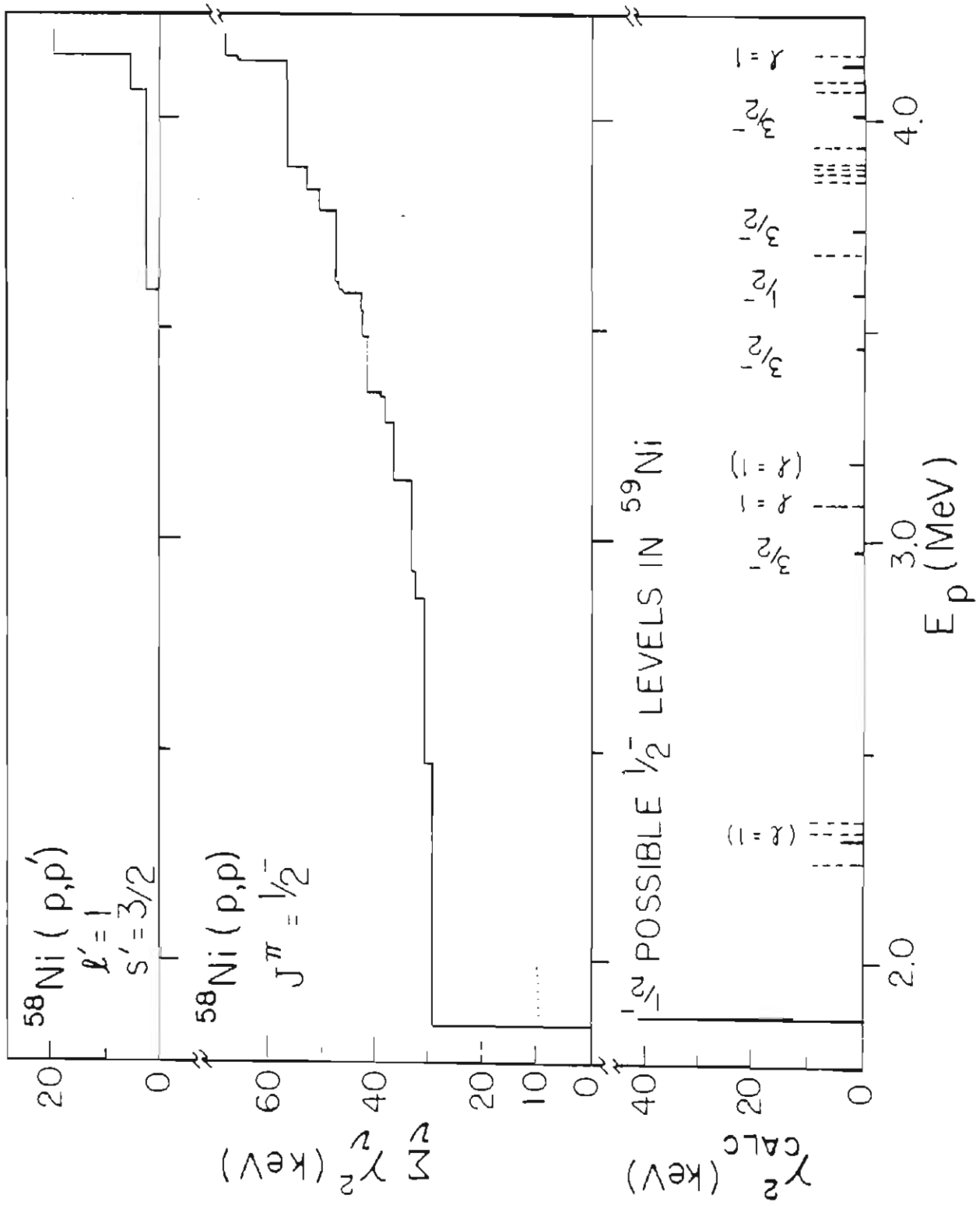
^{58}Ni (p,p′)
ℓ′ = 1
s′ = 3/2
^{58}Ni (p,p)
$J^{\pi} = 1/2^-$
γ^2_{VM} (keV)
γ^2_{CALC} (keV)
POSSIBLE $1/2^-$ LEVELS IN ^{59}Ni
$3/2^-$
$1/2^-$
$3/2^-$
$3/2^-$
$\lambda = 1$
$(\lambda = 1)$
E_p (MeV)
2.0
3.0
4.0

Figure 37. Cumulative Sums of the Elastic and Inelastic Reduced Widths of $3/2^-$ Levels in ^{59}Cu. Possible parent states are indicated at the bottom. Dashed lines indicate levels with unknown spectroscopic factors. A discussion of this figure is contained in the text.

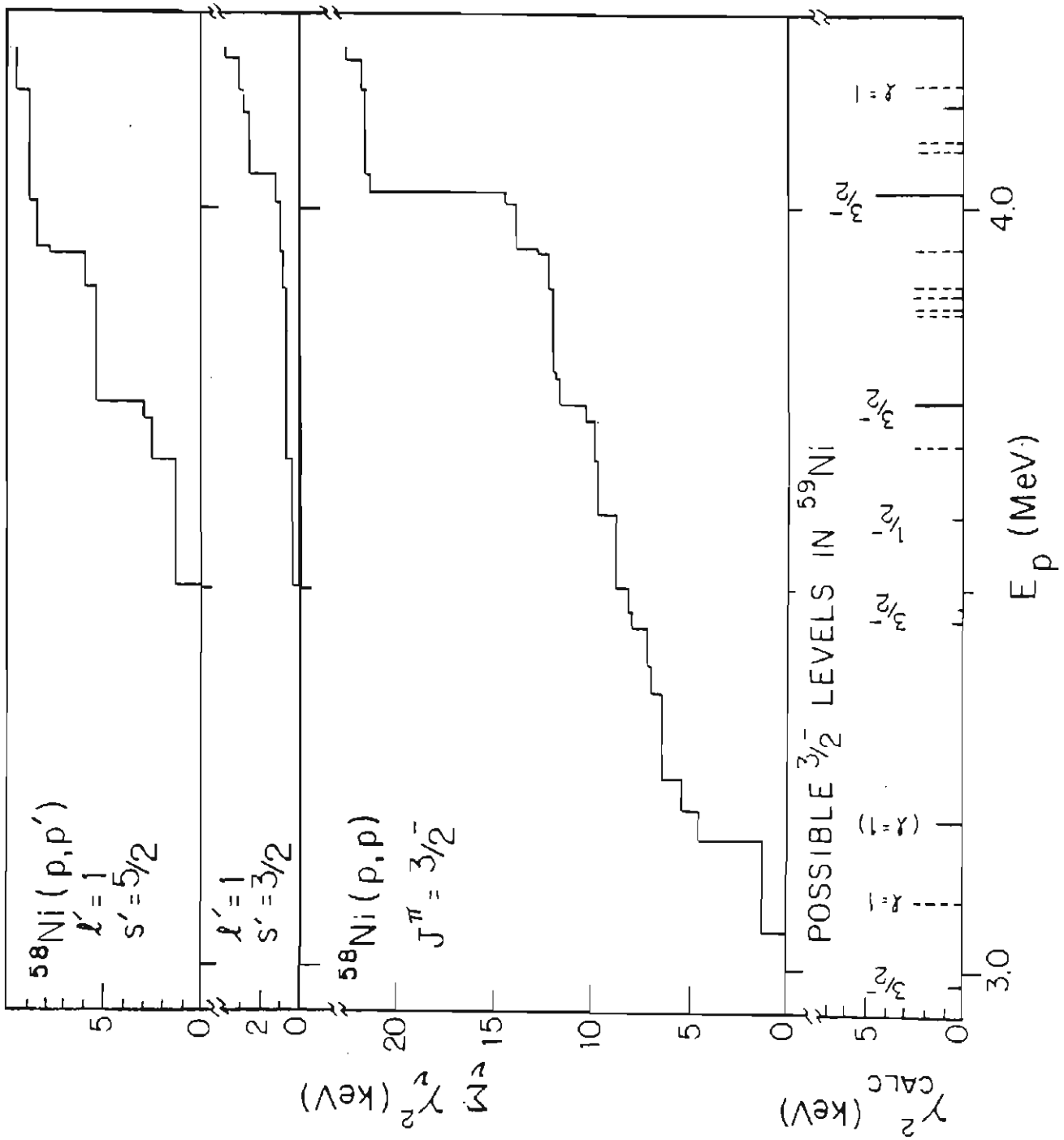
58Ni (p,p′)
ℓ′ = 1
s′ = 5/2
ℓ′ = 1
s′ = 3/2
58Ni (p,p)
Jπ = 3/2−
POSSIBLE 3/2− LEVELS IN 59Ni
(λ = 1)
λ = 1
3/2−
1/2−
3/2−
λ = 1
3/2−
Ep (MeV)
3.0
4.0
χ²calc (keV)
Σν χ²ν (keV)
0
5
0
2
0
20
15
10
5
0
5
0

Figure 38. Cumulative Sums of the Elastic and Inelastic Reduced Widths of $3/2^+$ Levels in ^{59}Cu. Possible parent states are indicated at the bottom. Dashed lines indicate levels with unknown spectroscopic factors. A discussion of this figure is contained in the text.

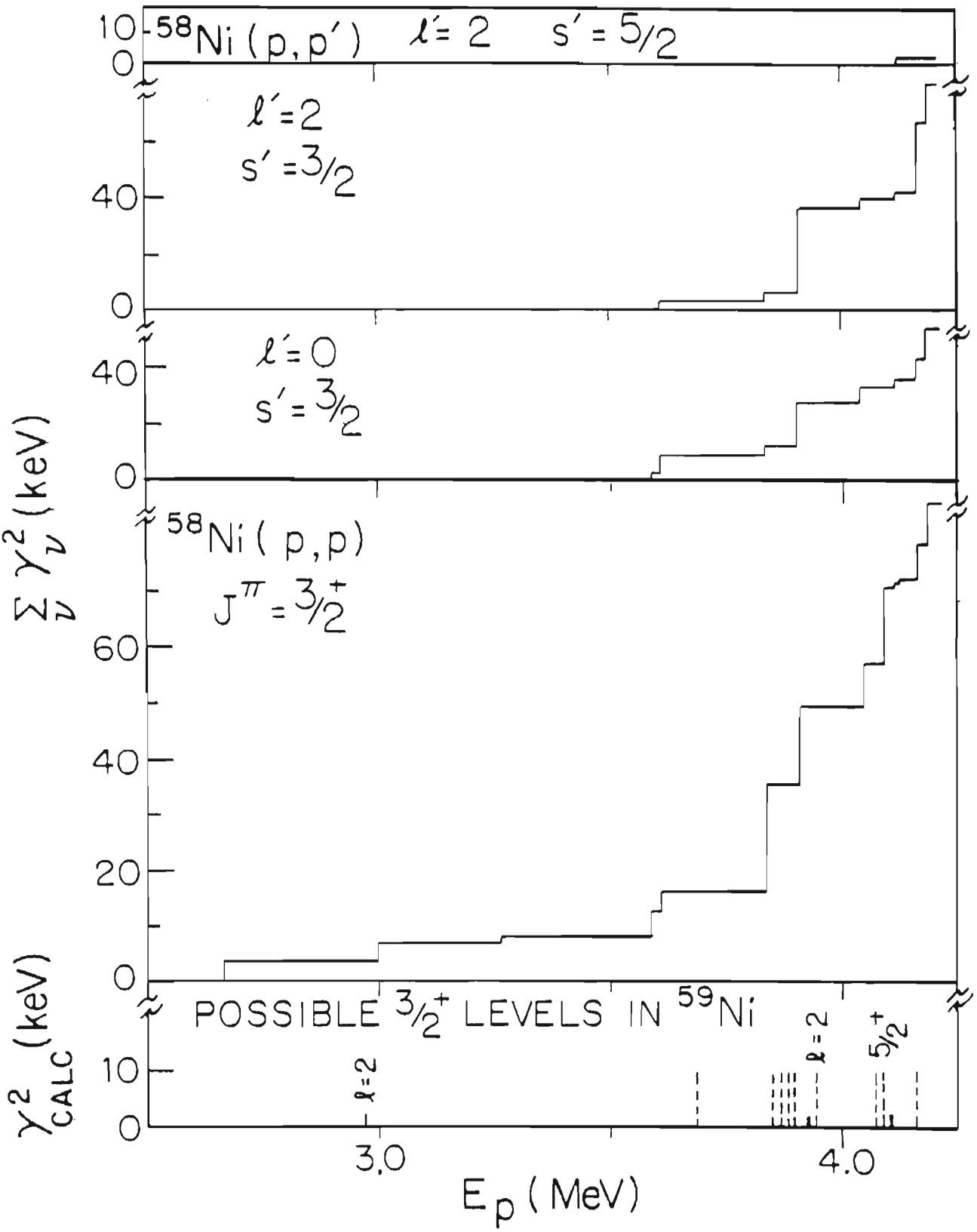
^{58}Ni (p,p′) $\ell'=2$ $s'=5/2$
$\ell'=2$
$s'=3/2$
$\ell'=0$
$s'=3/2$
^{58}Ni (p,p)
$J^\pi=3/2^+$
$\sum_\nu \gamma_\nu^2$ (keV)
γ^2_{CALC} (keV)
POSSIBLE $3/2^+$ LEVELS IN ^{59}Ni
$\ell=2$
$\ell=2$
$5/2^+$
E_p (MeV)

Figure 39. Cumulative Sums of the Elastic and Inelastic Reduced Widths of $5/2^+$ Levels in ^{59}Cu. Possible parent states are indicated at the bottom. Dashed lines indicate levels with unknown spectroscopic factors. A discussion of this figure is contained in the text.

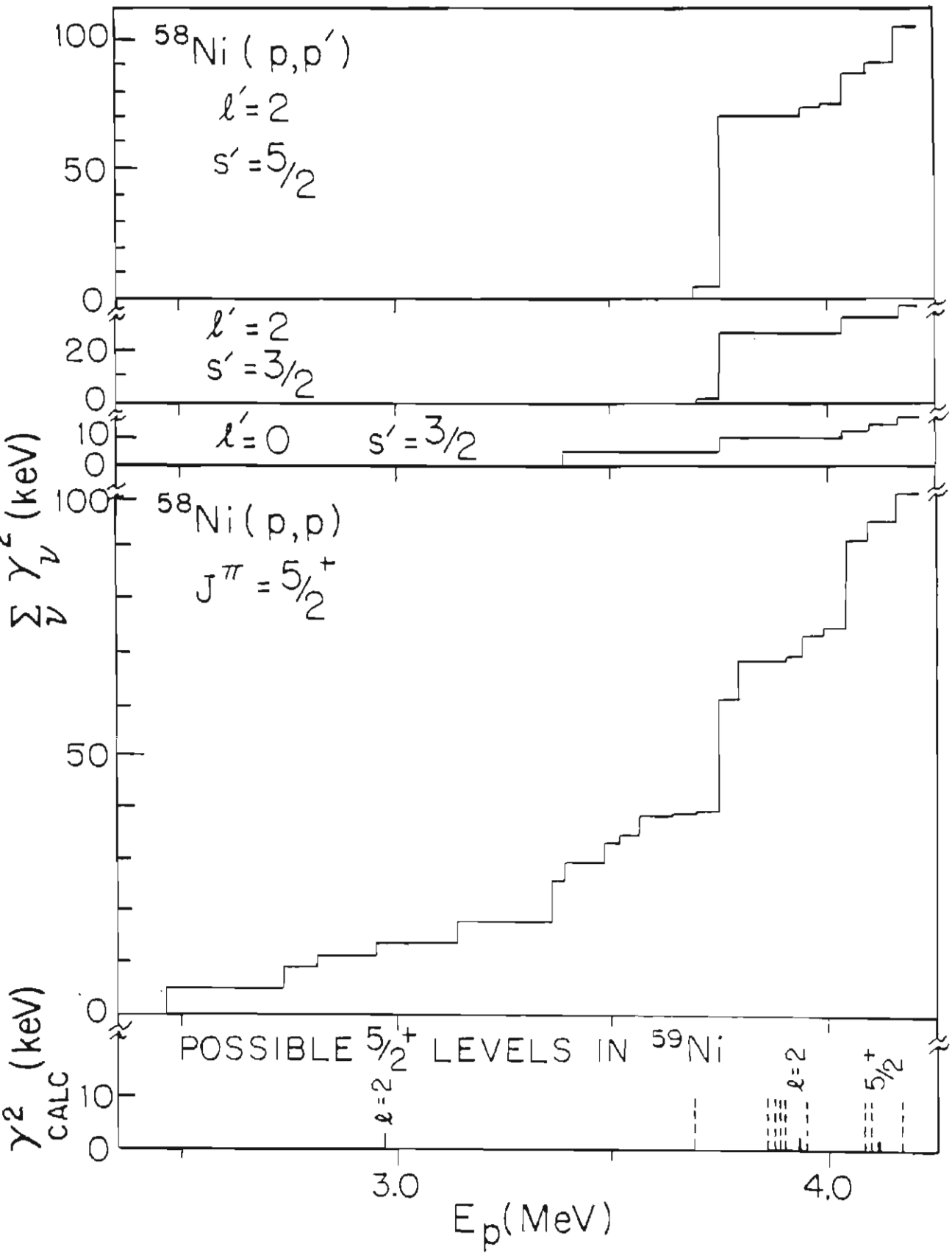
^{58}Ni (p,p′)
ℓ′=2
s′=5/2
ℓ′=2
s′=3/2
ℓ′=0
s′=3/2
^{58}Ni(p,p)
$J^{\pi}=5/2^{+}$
$\sum_{\nu}\gamma_{\nu}^{2}$ (keV)
γ^{2}_{CALC} (keV)
POSSIBLE $5/2^{+}$ LEVELS IN ^{59}Ni
ℓ=2
ℓ=2
$5/2^{+}$
E_p(MeV)

Figure 41. Cumulative Sums of the Elastic and Inelastic Reduced Widths of $9/2^+$ (and $7/2^+$) Levels in ^{59}Cu. Possible parent states are indicated at the bottom. Dashed lines indicate levels with unknown spectroscopic factors. A discussion of this figure is contained in the text.

Figure 40. Cumulative Sums of the Elastic and Inelastic Reduced Widths of $5/2^-$ (and $7/2^-$) Levels in ^{59}Cu. Possible parent states are indicated at the bottom. Dashed lines indicate levels with unknown spectroscopic factors. A discussion of this figure is contained in the text.

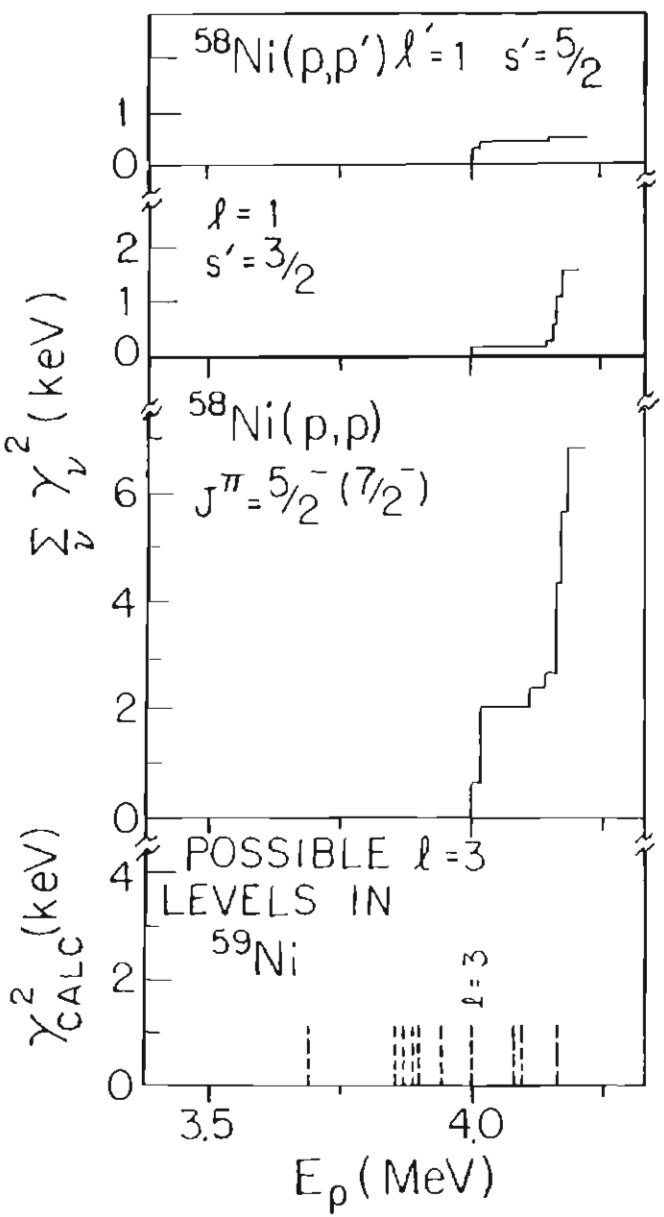
^{58}Ni(p,p') $\ell'=1$ $s'=5/2$
$\ell=1$
$s'=3/2$
^{58}Ni(p,p)
$J^{\pi}=5/2^{-}(7/2^{-})$
POSSIBLE $\ell=3$
LEVELS IN
^{59}Ni
$\ell=3$
$\sum_{\nu}\gamma_{\nu}^{2}$ (keV)
γ^{2}_{CALC} (keV)
E_p (MeV)

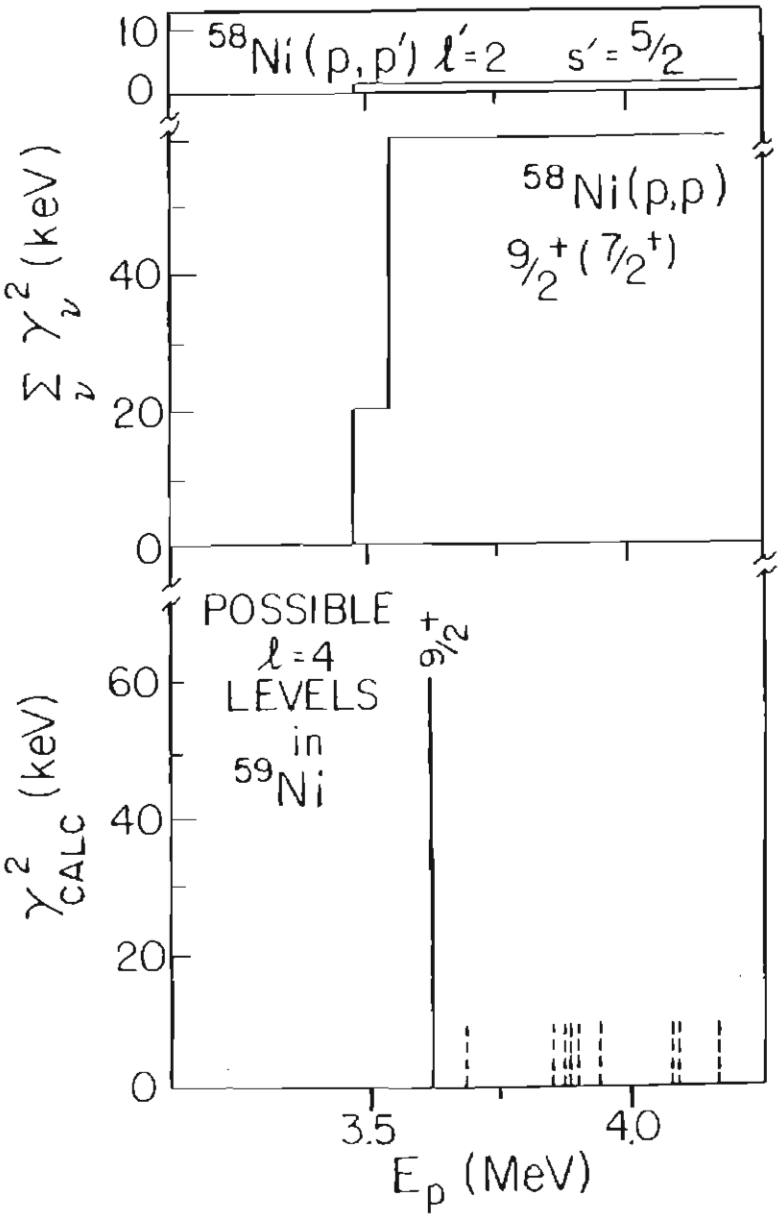
^{58}Ni(p,p') $\ell'=2$ $s'=5/2$
^{58}Ni(p,p)
$9/2^{+}(7/2^{+})$
POSSIBLE
$\ell=4$
LEVELS
in
^{59}Ni
$9/2^{+}$
$\sum_{\nu}\gamma_{\nu}^{2}$ (keV)
γ^{2}_{CALC} (keV)
E_p (MeV)

not understood.

Figure 41 shows the cumulative sum plots of $9/2^+$ (and $7/2^+$) resonances in ^{59}Cu and possible $\ell=4$ states in ^{59}Ni. The two $\ell=4$ resonances at 3.4750 and 3.5464 MeV are presumed to be fragments of the IAR whose parent is at 3.062 MeV excitation energy.

Table 9 summarizes the analogue state identifications. Coulomb energies and spectroscopic factors are discussed in section IV A 3 and IV A 4.

3. Coulomb Energies

Equation 1 was used to calculate Coulomb displacement energies for the IAR identified in section IV A 2. The results are shown in table 10. References for the excitation energies shown are given in tables 7 and 8. Uncertainties given for the energies of the IAR were estimated including the energy measurement uncertainty of ±2 keV, uncertainties in assigning individual resonance energies, and (most important for some fragmented IAR) uncertainties in the relative strengths of the fragments. In table 10 Δ is a measure of the Coulomb energy deviation from that of the ground state. (Ground state Coulomb energies are from Courtney and Fox (1975).)

The Coulomb energies obtained by Brändle et al. (1975) and Arai et al. (1976) agree within uncertainties with

Table 9.

IAR Identified in ^{55}Co and ^{59}Cu

^{55}Co			^{59}Cu		
E_x (MeV)	E_A (MeV)	J^π	E_x (MeV)	E_A (MeV)	J^π
3.661	(3.3920)	$3/2^-$	3.036	(3.5811)	$1/2^-$
3.791	3.4780	$1/2^-$	3.062	3.5223	$(9/2)^+$
3.814	3.8016	$9/2^+$	3.193	(3.7432)	$3/2^-$
4.028	3.8016	$(5/2)^-$	3.463	(4.0104)	$5/2^-$
4.057	(3.8056)	$3/2^-$	3.463	4.0224	$3/2^-$
4.450	(4.0763)	$1/2^+$	3.573	(4.1266)	$1/2^-$
4.466	4.1354	$5/2^+$			
4.495	(4.2208)	$1/2^-$			
4.538	(4.2642)	$1/2^-$			
	(4.2767)	$1/2^-$			
	(4.3039)	$3/2^-$			

E_A was determined for each IAR with equation 3. Parentheses around E_A indicate that the identification is tentative. Parentheses around J^π indicate that, although the ℓ-value was well established, the spin is uncertain.

Table 10.

Coulomb Displacement Energies

^{55}Cu

E_x (a) (MeV)	E_A (b) (MeV)		J^π	$\Delta E_c^{Present}$ (MeV)		Δ(c) (keV)	ΔE_c (d) (MeV)
3.661	(3.392)	(2)	$3/2^-$	8.968	(12)	5	
3.814	3.467	(2)	$9/2^+$	8.889	(12)	84	
3.791	3.478	(4)	$1/2^-$	8.922	(12)	51	8.917
4.028	3.802	(10)	$(5/2)^-$	9.003	(15)	-30	
4.057	(3.806)	(3)	$3/2^-$	8.978	(12)	-5	
4.450	(4.076)	(15)	$1/2^+$	8.851	(19)	122	8.842
4.466	4.135	(3)	$5/2^+$	8.893	(12)	80	8.892
4.495	(4.221)	(3)	$1/2^-$	8.948	(12)	25	
4.538	(4.264)	(3)	$1/2^-$	8.947	(12)	26	

^{59}Cu

E_x (a) (MeV)	E_A (b) (MeV)		J^π	$\Delta E_c^{Present}$ (MeV)		Δ(c) (keV)	ΔE_c (e) (MeV)
3.036	(3.581)	(2)	$1/2^-$	9.488	(12)	-7	
3.062	3.522	(20)	$(9/2)^+$	9.404	(23)	77	9.407
3.179	(3.743)	(2)	$3/2^-$	9.504	(12)	-23	
3.463	(4.010)	(5)	$5/2^-$	9.483	(13)	-2	
3.463	4.022	(2)	$3/2^-$	9.494	(12)	-13	9.413
3.573	(4.127)	(2)	$1/2^-$	9.487	(12)	-6	

Isobaric Pair	B_N (f) (MeV)		ΔE_c^{Gnd} (g) (MeV)		$\Delta E_c^{Gnd} / Z/A^{1/3}$
^{55}Fe - ^{55}Co	9.299	(6)	8.973	(6)	1.312
^{59}Ni - ^{59}Cu	9.003	(6)	9.481	(19)	1.318

(a) For references see tables 7 and 8. Uncertainties are ±10 keV.
(b) Parentheses around E_A indicate a tentative assignment. The integers in parentheses are energy uncertainties in keV.
(c) $\Delta \equiv \Delta E_c^{Gnd} - \Delta E_c$.
(d) Brändle et al. (1975)
(e) Arai et al. (1976)
(f) Neutron binding energies are from Maples et al. (1966).
(g) Ground state Coulomb energies are from Courtney and Fox (1975).

those of the present experiments with one exception: the Coulomb energies associated with the parent state at 3.463 MeV in ^{59}Cu. Arai et al. assigned their $3/2^-$ resonance at 3.933 MeV proton energy as the IAR. Their maximum energy was insufficient to observe the $3/2^-$ resonance at 4.022 MeV which we claim is the IAR. Comparison of the spectroscopic factors strongly supports the present assignment.

4. Spectroscopic Factors

Spectroscopic factors were obtained with equation 2. Single particle strengths (Γ_{sp}) were calculated with the computer program Hans (Harney 1969). The code Hans calculates Γ_{sp} by means of the R-matrix method of Thompson, Adams, and Robson (1968) (TAR); the shell-model method of Zaidi and Darmodjo (1967) and Harney (1967) (ZDH); and the shell-model method of Mekjian and MacDonald (1968)) (MM). The neutron potential (U_N) is automatically adjusted to produce a level in the parent with the correct binding energy. The proton single particle width is then determined for a proton potential (U_p) which is lower than U_N by the symmetry potential, $((2T_o + 1)/2)(125/A)$ (MeV)).

The results of these calculations are listed in table 11, with n the number of nodes in the wave function, ℓ the proton orbital angular momentum, and 2J twice the

total angular momentum. The widths calculated by the different methods (TAR, ZDH, and MM) agree quite well; the shell model values are about 5 - 10% larger. Moses (1970) estimates the uncertainties in the widths due to uncertainties in the model parameters to be about ±15.

Agreement of inelastic single particle widths calculated by the different methods is good; the values obtained with the shell model methods are again 5 - 10% larger than those determined with the R-matrix method. These values are listed in table 12. In these calculations the proton energies were obtained by subtracting the energy of the first excited state of the target (corrected to a laboratory energy) from the incident proton energy; the neutron binding energy was also obtained by subtracting the energy of the first excited state of the target from the neutron binding energy of the parent state; and the ℓ-value was that of the exiting proton. The other parameters and procedures were the same as with the calculation of elastic single particle widths.

In table 13 are listed the number of fragments N included for each IAR, the sum of these N widths $\Sigma\Gamma_i$, the average width per resonance $\langle\Gamma\rangle$ of the background resonances, and the proton spectroscopic factors obtained with these different elastic single particle widths.

In table 14 the elastic spectroscopic factors are

Table 11.

Elastic Single Particle Widths

^{55}Co

E_x (MeV)	E_A (MeV)	n ℓ 2J	$-U_N$ (MeV)	$\sqrt{sp/(2T_o+1)}$ (keV) TAR	ZDH	MM
3.661	3.392	2 1 3	45.654	31.4	33.7	33.9
3.814	3.467	1 4 9	55.978	0.12	0.11	0.11
3.791	3.478	2 1 1	48.838	33.3	39.3	39.5
4.028	3.802	1 3 5	49.191	1.78	2.25	2.27
4.057	3.806	2 1 3	44.935	55.1	57.5	57.8
4.450	4.076	3 0 1	65.391	142.8	80.2	81.0
4.466	4.135	2 2 5	61.139	36.5	31.5	31.5
4.495	4.221	2 1 1	47.516	85.0	92.5	93.1
4.538	4.264	2 1 1	47.513	85.1	92.6	93.3
	4.277	2 1 1	47.516	86.3	92.9	93.5
	4.304	2 1 3	43.869	91.1	97.9	98.3

^{59}Cu

E_x (MeV)	E_A (MeV)	n ℓ 2J	$-U_N$ (MeV)	$\sqrt{sp/(2T_o+1)}$ (keV) TAR	ZDH	MM
3.036	3.581	2 1 1	47.803	26.0	30.3	30.5
3.062	3.522	1 4 9	54.248	0.10	0.08	0.09
3.179	3.743	2 1 3	44.283	34.7	37.6	37.9
3.463	4.010	1 3 5	47.524	1.75	2.19	2.20
3.463	4.022	2 1 3	43.803	50.3	53.2	53.5
3.573	4.127	2 1 1	46.882	54.6	60.3	60.7

$U_N - U_p = ((2T_o + 1)/2)(125/A) = \begin{cases} 3.472 \text{ MeV for } ^{55}Co \\ 3.233 \text{ MeV for } ^{59}Cu \end{cases}$

$R_1 = R_3 = R_c = \begin{cases} 4.725 \text{ fm. for } ^{55}Co \\ 4.839 \text{ fm. for } ^{59}Cu \end{cases}$

$a_1 = a_2 = 0.67$ fm. $\qquad V_{so} = -8.0$ MeV

Table 12.

Inelastic Single Particle Widths

^{55}Co

E_x (MeV)	E_A (MeV)	n ℓ' 2J	$-U_N$ (MeV)	$\sqrt{S_p/(2T_o+1)}$ (keV) TAR	ZDH	MM
3.661	3.392	2 1 3	48.112	0.71	0.84	0.84
3.814	3.467	2 2 9	70.920	0.21	0.22	0.22
4.028	3.802	2 1 5	50.876	3.00	3.52	3.55
4.057	3.806	2 1 3	47.428	3.27	3.71	3.75
	4.277	2 1 1	50.004	10.5	12.4	12.5
	4.304	2 1 3	46.415	11.9	14.0	14.1

^{59}Cu

E_x (MeV)	E_A (MeV)	n ℓ' 2J	$-U_N$ (MeV)	$\sqrt{S_p/(2T_o+1)}$ (keV) TAR	ZDH	MM
3.062	3.522	2 2 9	68.995	0.10	0.11	0.12
3.179	3.743	2 1 3	46.770	1.17	1.36	1.38
3.463	4.010	2 1 5	49.522	2.61	3.25	3.26

$$U_N - U_p = ((2T_o + 1)/2)(125/A) = \begin{cases} 3.472 \text{ MeV for } ^{55}Co \\ 3.233 \text{ MeV for } ^{59}Cu \end{cases}$$

$$R_1 = R_3 = R_c = \begin{cases} 4.725 \text{ fm. for } ^{55}Co \\ 4.839 \text{ fm. for } ^{59}Cu \end{cases}$$

$a_1 = a_2 = 0.67$ fm. $\qquad V_{so} = -8.0$ MeV

Table 13.

Elastic Proton Spectroscopic Factors

^{55}Co

E_A (MeV)	n	ℓ	2J	N	$\Sigma\Gamma_i$ (keV)	$\langle\Gamma\rangle$ (keV)	S_p TAR	ZDH	HM
3.392	2	1	3	1	0.450	0.12	0.011	0.010	0.010
3.467	1	4	9	2	0.084	0.00	0.677	0.758	0.750
3.478	2	1	1	2	15.500	0.37	0.443	0.376	0.374
3.802	1	3	5	5	0.116	0.00	0.065	0.052	0.051
3.806	2	1	3	2	1.050	0.23	0.011	0.010	0.010
4.076	3	0	1	4	68.500	1.60	0.435	0.774	0.767
4.135	2	2	5	2	5.430	0.39	0.127	0.148	0.148
4.221	2	1	1	1	4.000	0.93	0.037	0.034	0.034
4.264	2	1	1	1	4.000	0.98	0.036	0.033	0.033
4.277	2	1	1	1	1.900	0.99	0.011	0.010	0.010
4.304	2	1	3	1	1.800	0.39	0.015	0.014	0.014

^{59}Cu

E_A (MeV)	n	ℓ	2J	N	$\Sigma\Gamma_i$ (keV)	$\langle\Gamma\rangle$ (keV)	S_p TAR	ZDH	HM
3.581	2	1	1	1	0.600	0.30	0.012	0.010	0.010
3.522	1	4	9	2	0.050	0.00	0.521	0.595	0.588
3.743	2	1	3	1	0.310	0.15	0.005	0.004	0.004
4.010	1	3	5	2	0.046	0.00	0.026	0.021	0.021
4.022	2	1	3	1	2.500	0.22	0.045	0.043	0.043
4.127	2	1	1	1	3.800	0.64	0.058	0.052	0.052

n: number of nodes
N: number of IAR fragments
$\langle\Gamma\rangle$: average laboratory width of background resonances at the energy of the IAR. $\langle\Gamma\rangle$ was obtained from the expression $\langle\Gamma\rangle = 2P(E_A)\langle\gamma^2\rangle$.

Table 14.

Comparison of Spectroscopic Factors

^{55}Co

E_A (MeV)	J^π	S_{dp} (a)	(b)	(c)	(d)	S_p TAR	ZDH	(e)
3.392	$3/2^-$					0.010	0.009	
3.467	$9/2^+$		0.740			0.677	0.758	
3.478	$1/2^-$		0.700	0.460	0.500	0.443	0.376	0.35
3.802	$5/2^-$		0.056		0.060	0.065	0.052	
3.806	$3/2^-$					0.011	0.010	
4.076	$1/2^+$					0.435	0.774	0.21
4.135	$5/2^+$		0.170		0.130	0.127	0.148	0.08
4.221	$1/2^-$	0.032				0.037	0.034	
4.267	$1/2^-$		0.045			0.036	0.033	
4.277	$1/2^-$					0.011	0.010	
4.304	$3/2^-$					0.015	0.014	

^{59}Cu

E_A (MeV)	J^π	S_{dp} (f)	(g)	(h)	(i)	S_p TAR	ZDH	(j)
3.581	$1/2^-$		0.016	0.035		0.012	0.010	
3.522	$9/2^+$	0.790	0.750	1.060	0.474	0.521	0.595	0.451
3.740	$3/2^-$	0.011	0.008	0.016		0.005	0.004	
4.010	$5/2^-$					0.026	0.021	
4.022	$3/2^-$	0.038	0.038	0.035	0.031	0.045	0.043	0.004
4.127	$1/2^-$			0.013		0.058	0.052	

(a) Sperduto and Rapaport (1961)
(b) Fulmer and McCarthy (1963)
(c) Bochin et al. (1964)
(d) Kocher and Haeberli (1972)
(e) Brändle et al. (1975)
(f) Cohen et al. (1972)
(g) Fulmer et al. (1964)
(h) Cosman et al. (1966)
(i) Aymar et al. (1973)
(j) Arai et al. (1976)

compared with those obtained in (d,p) experiments[1] and in other proton scattering experiments. The agreement between S_p (TAR) and S_{dp} for the ^{55}Fe - ^{55}Co pair is excellent. The agreement between S_p(TAR) and S_{dp} for the ^{59}Ni - ^{59}Cu pair is good except for the $1/2^-$ resonance at 4.1266 MeV. The large value of S_p for this IAR is not understood; there was, however, a disagreement among several (d,p) studies concerning the ℓ-value of an adjacent level near 3.544 MeV excitation. Aymar et al. (1973) assigned $5/2^+$ to this level while Fulmer et al. (1964) made an $\ell=2$ assignment and Cosman et al. (1966) adopted an $\ell=1$ assignment with $(2J+1)\,S_{dp} = 0.117$. In the level scheme adopted in this work (see table 8), the $\ell=2$ assignment was chosen. If this state were actually the parent of the $1/2^-$ resonance at 4.127 MeV proton energy, then the spectroscopic factor $S_{dp} = 0.117/2 = 0.059$ agrees with that observed. This discussion illustrates how tentative most of the analogue assignments are for states with small spectroscopic factors.

Brändle et al. obtained the value $S_p = 0.35$ for the analogue of the $1/2^-$ parent state at 3.791 MeV, but included only one of the two fragments of the IAR. Including both fragments they obtain $S_p = 0.44$ in perfect agreement with the present value. The other two spectroscopic factors

---

1. The (d,p) work of Maxwell and Parkinson (1964) was omitted due to a systematic trend — their values of S_{dp} were half as large as those from several other (d,p) experiments.

Table 15.

Inelastic Proton Spectroscopic Factors

^{55}Co

E_A (MeV)	n ℓ' 2J	N	$\Sigma\Gamma_i$ (keV)	$\langle\Gamma\rangle$ (keV)	S_p TAR	S_p ZDH
3.392	2 1 3	1	0.127	0.003	0.175	0.148
3.467	2 2 9	2	0.024	0.000	0.114	0.109
3.802	2 1 5	5	0.211	0.000	0.070	0.060
3.806	2 1 3	2	0.118	0.025	0.021	0.018
4.277	2 1 1	1	2.300	0.055	0.214	0.181
4.304	2 1 3	1	1.000	0.095	0.076	0.065

^{59}Cu

E_A (MeV)	n ℓ' 2J	N	$\Sigma\Gamma_i$ (keV)	$\langle\Gamma\rangle$ (keV)	S_p TAR	S_p ZDH
3.522	2 2 9	2	0.001	0.000	0.010	0.009
3.743	2 1 3	1	0.020	0.008	0.010	0.009
4.010	2 1 5	2	0.009	0.000	0.003	0.003

n: number of nodes
N: number of IAR fragments

cf cases remarkably good agreement was found. These analyses and results are discussed in the following sections.

2. Width Distributions

The distribution of reduced widths of compound states in ^{55}Co and ^{59}Cu were compared with the distribution of Porter and Thomas (1956):

$$P(Y) = (2\pi Y)^{-1} \exp(-Y/2)$$

where

$$Y = \gamma^2/\langle\gamma^2\rangle$$

The Porter-Thomas distribution assumes the average reduced width $\langle\gamma^2\rangle$ is constant. An energy dependence of $\langle\gamma^2\rangle$ could be caused by isobaric analogue resonances (IAR), other types of doorway states, or even the giant resonances themselves. In the following analysis, the only correction employed is the omission of analogue states.

The distribution of elastic reduced widths for resonances of each spin and parity were plotted in the form of histograms and compared with the corresponding Porter-Thomas distribution. The number of widths N and the average reduced width $\langle\gamma^2\rangle$ that were adopted for each Porter-Thomas distribution were obtained from the corresponding sequence of observed widths. This procedure gives the correct distribution if N is large and the widths are selected in an unbiased manner. In fact, laboratory widths less than

$\sim$ 8 eV were not observed and the number of observed widths is small.

In spite of these difficulties, the Porter-Thomas distribution appears to agree quite well with the histograms except for small values of Y. This is shown in figures 42 and 43 for ^{55}Co and ^{59}Cu, respectively. The Porter-Thomas distribution is multiplied by $\sqrt{Y}$ and plotted on a log-log scale in order to emphasize the effect of the missing small widths. Since the penetrability is energy dependent, the minimum observable reduced width varies with excitation energy. The values of Y corresponding to these various minimum observable reduced widths are shown on each plot as the range of Y values between the arrows. The effect of these missing small widths is apparent in the figures.

Numerical comparison of the area under the distribution and the area under the histogram give an estimate of the number of missed widths. The results of this comparison (over the range Y = 0.0 to 0.05) are listed in table 16. The estimate of the total number of resonances N is the sum of the observed resonances plus the estimate of those unobserved. The uncertainty ΔN is the number of unobserved resonances plus the number of observed resonances with tentative assignments (when this rule gave $\Delta N < 2$, $\Delta N = 2$ was adopted). The IAR were omitted in obtaining the average reduced width $\langle \gamma^2 \rangle$. The corrected average reduced width $\langle \gamma^2_c \rangle$ was obtained by adding to the sequence of N widths,

Figure 42. Reduced Width Distributions for ^{55}Co. The smooth curves are Porter-Thomas distributions. Each histogram and distribution was "normalized" by dividing the number of reduced widths per unit Y by the total number of widths of the sequence (and multiplying by 100 to give a percent). The two arrows connected by a dashed line indicate the values of Y corresponding to the minimum observable reduced width (assuming $\Gamma_{minimum}$ = 8 eV) at the lowest and highest proton energy.

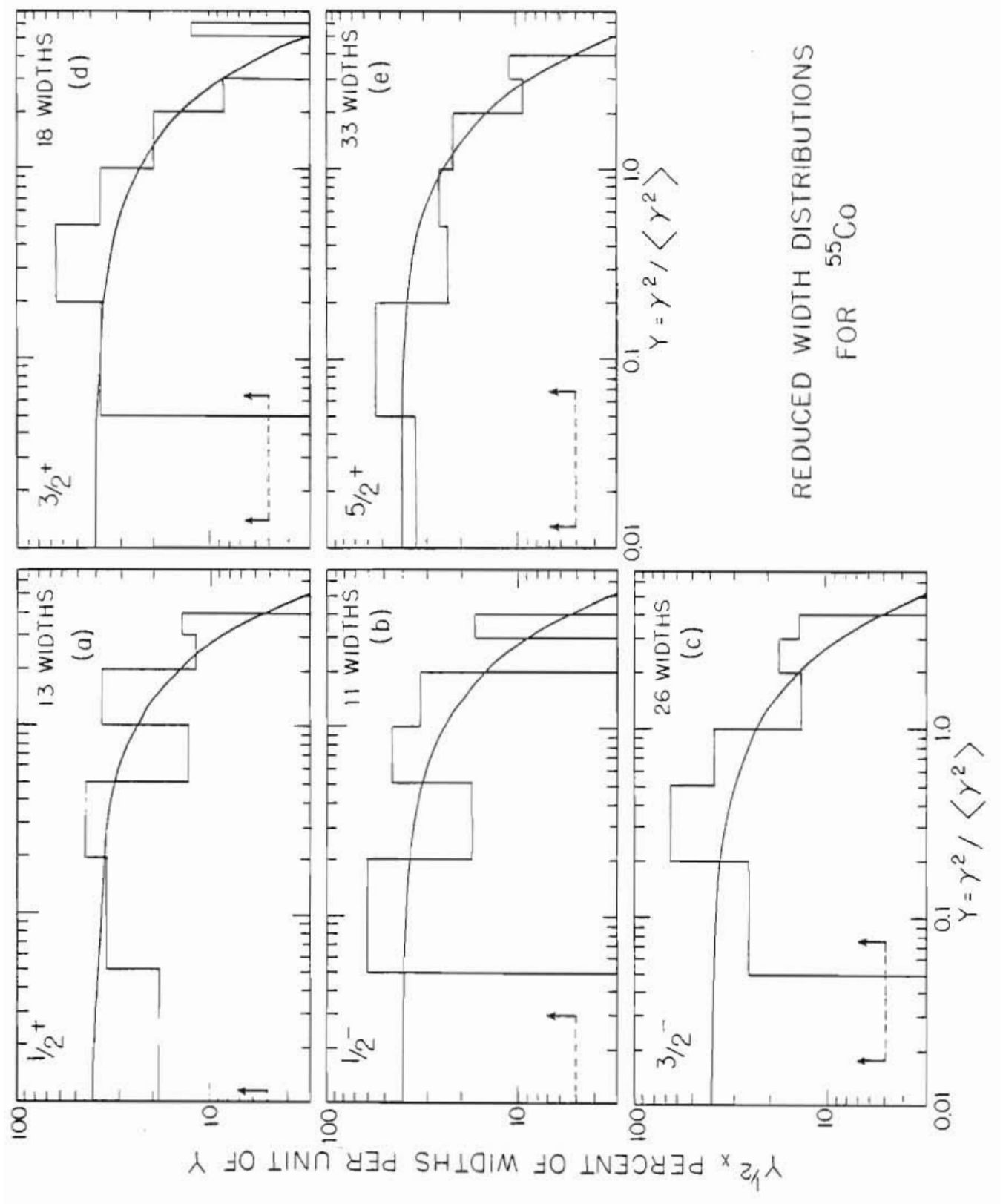
REDUCED WIDTH DISTRIBUTIONS
FOR ^{55}Co
$\gamma^2_{\frac{1}{2}}$ x PERCENT OF WIDTHS PER UNIT OF γ
$Y = \gamma^2 / \langle \gamma^2 \rangle$
$1/2^+$
13 WIDTHS
(a)
$1/2^-$
11 WIDTHS
(b)
$3/2^-$
26 WIDTHS
(c)
$3/2^+$
18 WIDTHS
(d)
$5/2^+$
33 WIDTHS
(e)
100
10
0.01
0.1
1.0

Figure 43. Reduced Width Distributions for ^{59}Cu. The smooth curves are Porter-Thomas distributions. Each histogram and distribution was "normalized" by dividing the number of reduced widths per unit Y by the total number of widths of the sequence (and multiplying by 100 to give a percent). The two arrows connected by a dashed line indicate the values of Y corresponding to the minimum observable reduced width (assuming $\Gamma_{minimum}$ = 8 eV) at the lowest and highest proton energy.

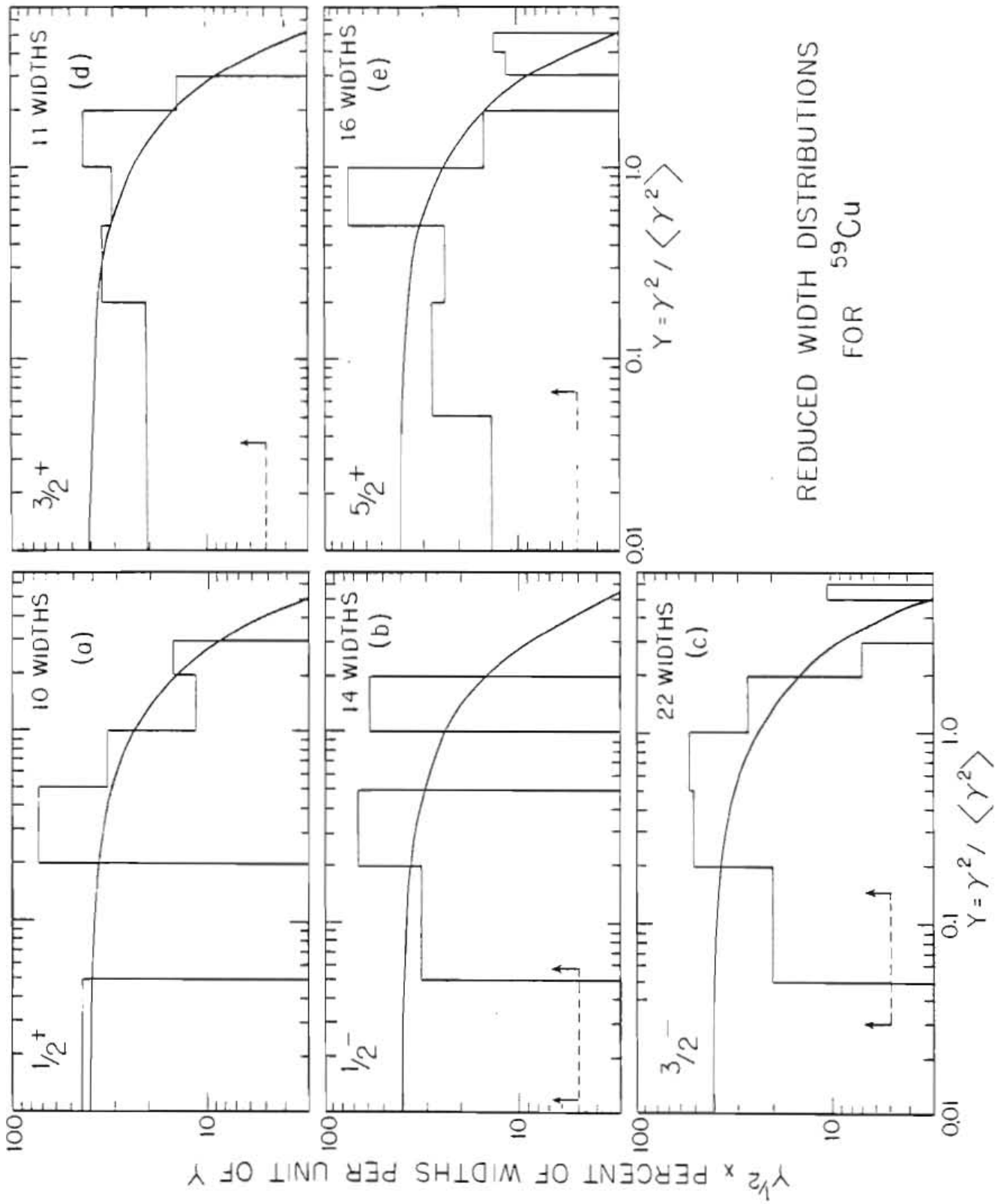
REDUCED WIDTH DISTRIBUTIONS
FOR ^{59}Cu
$\gamma_{1/2}$ x PERCENT OF WIDTHS PER UNIT OF γ
$Y = \gamma^2 / \langle \gamma^2 \rangle$
$1/2^+$
10 WIDTHS
(a)
$1/2^-$
14 WIDTHS
(b)
$3/2^-$
22 WIDTHS
(c)
$3/2^+$
11 WIDTHS
(d)
$5/2^+$
16 WIDTHS
(e)
100
10
0.01
0.1
1.0

Table 16.

Width Distributions

^{55}Co

J^π	N	N_u	N_{IAR}	N_T	ΔN	$\langle \gamma^2 \rangle$ (keV)	$\langle \gamma_c^2 \rangle$ (keV)
$1/2^+$	13	1	4	18	2	2.00	1.85
$1/2^-$	11	2	5	18	5	1.66	1.41
$3/2^-$	26	4	3	33	6	0.64	0.55
$3/2^+$	18	3	0	21	9	2.10	1.80
$5/2^+$	33	0	2	35	10	2.18	2.18

^{59}Cu

J^π	N	N_u	N_{IAR}	N_T	ΔN	$\langle \gamma^2 \rangle$ (keV)	$\langle \gamma_c^2 \rangle$ (keV)
$1/2^+$	10	0	0	10	2	9.89	9.89
$1/2^-$	14	2	2	18	5	1.58	1.38
$3/2^-$	22	4	2	28	6	0.60	0.51
$3/2^+$	11	1	0	12	2	7.16	6.57
$5/2^+$	16	2	0	18	5	5.33	4.75

N : number of observed resonances (excluding IAR).

N_u : estimated number of unobserved resonances.

N_{IAR} : number of resonances identified as IAR.

N_T : total number of resonances.

ΔN : uncertainty in number of levels (see text for discussion).

$\langle \gamma^2 \rangle$: average reduced width for the N resonances.

$\langle \gamma_c^2 \rangle$: average reduced width corrected for missing levels.

N_ω widths each having $\gamma^2 = 0.017\langle\gamma^2\rangle$. The value 0.017 is the weighted average value of Y in the range Y = 0.0 to 0.05.

3. Level Densities

Bethe (1936, 1937) showed that the Fermi gas model of the nucleus predicts that the level density ρ is proportional to $\exp(2\sqrt{aE})$, where E is the excitation energy. This form for the density seems to be valid at high excitation energies but not at low energies. The function exp(E/T) does seem to be descriptive of nuclear level densities at lower excitation energies. Gilbert and Cameron (1965) proposed that the two functions be joined tangentially at some excitation energy E_χ and they gave prescriptions for obtaining E_χ. Their values of E_χ for ^{55}Co and ^{59}Cu are 6.527 and 6.312 MeV, respectively. These are lower than the excitation energies of the present experiment. Accordingly, the calculated level densities presented in this section were obtained with Gilbert and Cameron's equation 4 which has the $\exp(2\sqrt{aU})$ energy dependence (U = excitation energy - constant). Since all of the parameters of this equation were prescribed by Gilbert and Cameron, only the excitation energy and spin were varied to obtain the calculated densities presented in this section.

The experimental level density was obtained from

$\rho = (N - 1) / \Delta E$, where N is the number of levels of a given spin and parity and ΔE is the energy interval in which they were observed. The results of the present experiment are listed in table 17.

Small unobserved levels and misassigned levels cause errors in the number of levels N. Estimates of these errors were obtained from the width distribution analysis of the previous section. The corrected level density ρ_c (also listed in table 17) was obtained with the corrected number of levels N_T listed in table 16. The corrected densities ρ_c are at most 17% higher than the uncorrected values ρ; the smallness of the correction arises from the large average reduced width per resonance and corresponding small fraction of unobserved resonances. The density ρ_c is uncertain because of both the uncertainty in measuring N_T (ΔN) and because of the statistical uncertainty in obtaining the true average density from $N_T - 1$ spacings. (The statistical uncertainty of N_T is the standard deviation of the Wigner distribution: $\sqrt{0.273 N_T}$ (Lynn, 1968).) The square root of the sum of the squares of these two uncertainties divided by ΔE is the uncertainty $\Delta \rho_c$ listed in table 17.

The densities are expected to be independent of parity and to increase smoothly with spin (for spin $\leq 5/2$). The results in table 17 indicate that the density of the even parity states is consistently lower than that of the odd parity states. This is illustrated in figure 44 where

Table 17.

Level Densities

^{55}Co

J^{π}	N	ΔE	ρ	ρ_c	$\Delta\rho_c$
$1/2^+$	17	1.146	14.0	14.8	2.6
$1/2^-$	16	1.239	12.1	13.7	4.4
$3/2^-$	29	1.215	23.0	26.3	5.8
$3/2^+$	18	1.036	16.4	19.3	9.0
$5/2^+$	35	1.117	30.4	30.4	9.4

^{59}Cu

J^{π}	N	ΔE	ρ	ρ_c	$\Delta\rho_c$
$1/2^+$	10	1.029	8.7	8.7	2.5
$1/2^-$	16	0.998	15.0	17.0	5.5
$3/2^-$	24	1.024	22.5	26.4	6.5
$3/2^+$	11	0.918	10.9	12.0	2.9
$5/2^+$	16	1.022	14.7	16.6	5.4

N : number of observed resonances.

ΔE : difference between the maximum and minimum resonance energy (in MeV).

ρ : level density.

ρ_c : level density corrected for missing levels.

Densities are in units of levels per MeV.

Figure 44. Spin and Parity Dependence of Level Densities in ^{55}Co and ^{59}Cu. The solid lines represent the Gilbert and Cameron predictions. The average excitation energies were 8.892 and 7.013 MeV for ^{55}Co and ^{59}Cu, respectively (corresponding proton energies were 3.905 and 3.655 MeV, respectively).

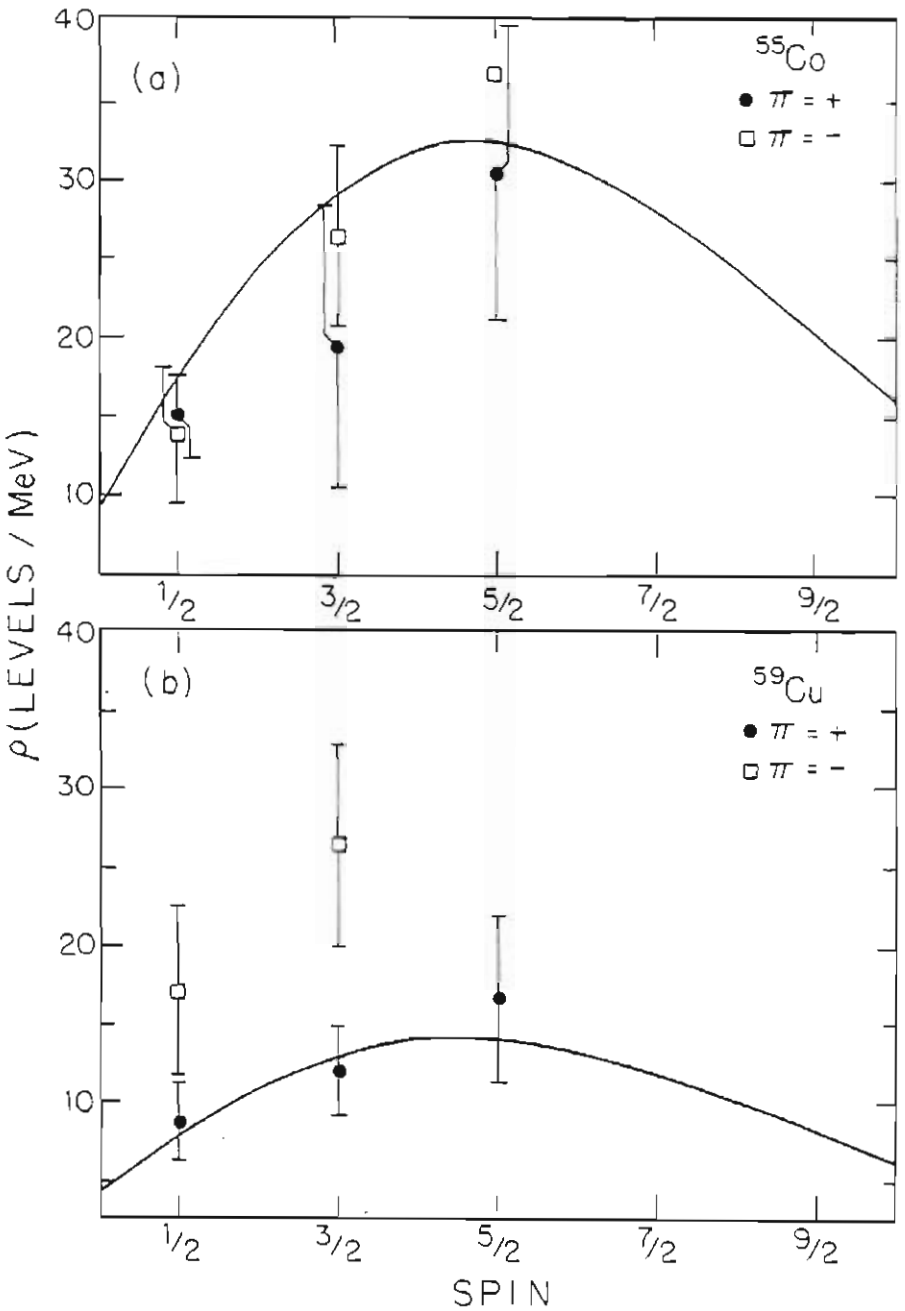
40
30
20
10
(a)
^{55}Co
● π = +
□ π = −
1/2
3/2
5/2
7/2
9/2
(b)
^{59}Cu
ρ(LEVELS / MeV)
SPIN

the densities ρ_c and uncertainties $\Delta\rho_c$ are plotted. The $5/2^-$ point for ^{55}Co was obtained from the five fragments of the IAR located at E_A = 3.802 MeV. The curves in figure 44 were calculated with Gilbert and Cameron's formulae with excitation energies of 8.892 and 7.013 MeV for ^{55}Co and ^{59}Cu, respectively. The usual statistical assumption of equal number of positive and negative parity states of the same spin (Gilbert and Cameron 1965) is obviously not valid at these excitation energies in ^{55}Co and ^{59}Cu. The magnitudes of the predicted densities agree well with those observed (the densities of the odd parity states in ^{59}Cu appear to be too large by a factor of two); the rates at which the predicted densities increase with spin also agree reasonably well with those observed.

To examine the energy dependence of the level densities, the resonances were grouped according to ℓ-value. This eliminated errors in estimates of the level densities due to misassigned spins, and reduced statistical errors by increasing the number of observed levels in each sequence. Each sequence of levels was divided into three or four smaller sequences having, as nearly as possible, the same number of levels. For example, the seventeen $1/2^+$ levels of ^{55}Co were divided into three smaller sequences: the first small sequence consisted of the first six levels, the second small sequence consisted of the second six levels, and the third small sequence consisted of the last

five levels. "Local average densities" were then obtained from the smaller sequences. These local average level densities are shown in figure 45 plotted at the average proton energy of the smaller sequence. The lower error bar is $\sqrt{0.273N}\,/\,\Delta E$, where N is the number of spacings and ΔE is now the energy interval from which the local density was obtained. The value $\sqrt{0.273N}\,/\,\Delta E$ is the statistical uncertainty of obtaining the true average density from a finite number of spacings. Missing levels also contribute to the uncertainty of the experimental level densities but can only increase the local level density above the measured value. The upper error bar includes the statistical uncertainty and an uncertainty which indicates the change in the density if several small resonances are added. The estimates of the number of missed levels were obtained from the earlier width distribution analysis.

The solid lines in figure 45 represent the Gilbert and Cameron predictions. The magnitudes of the predicted level densities again agree with the observed densities. The most obvious discrepancy is that the observed densities of odd parity states in ^{59}Cu are twice the predicted densities. The rate of increase with energy of the predicted densities seems to agree reasonably well with those observed; the density of even parity states of ^{59}Cu appear to increase more rapidly than predicted. The lack of

Figure 45. Energy Dependence of Level Densities in ^{55}Co and ^{59}Cu. The solid lines represent the Gilbert and Cameron predictions. (E_p = 4 MeV corresponds to excitation energies of 8.985 and 7.352 MeV for ^{55}Co and ^{59}Cu, respectively.)

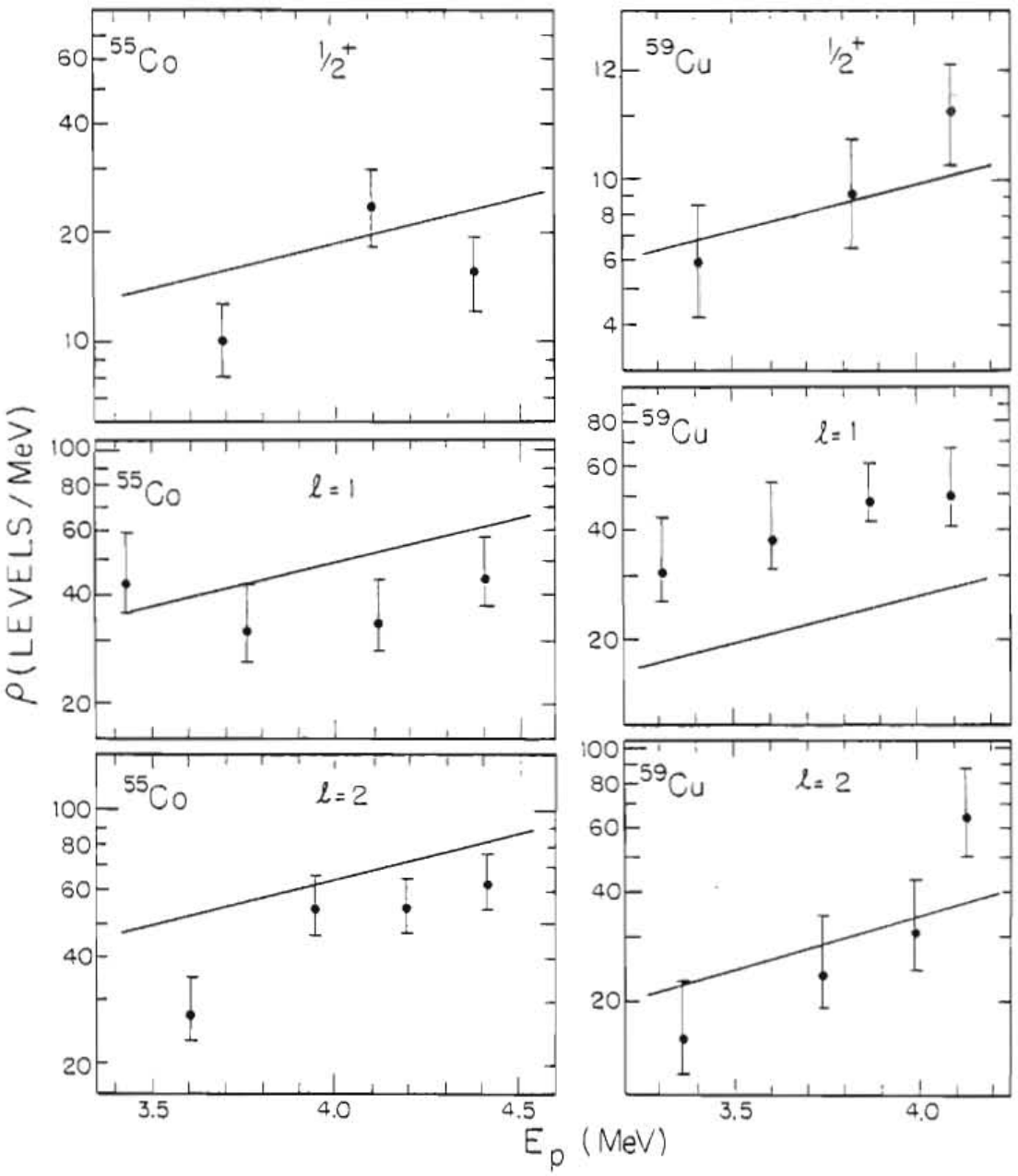
^{55}Co
$1/2^+$
^{59}Cu
$1/2^+$
^{55}Co
$\ell = 1$
^{59}Cu
$\ell = 1$
^{55}Co
$\ell = 2$
^{59}Cu
$\ell = 2$
ρ(LEVELS / MeV)
E_p (MeV)

detailed agreement could be due to the relatively simple structure of these nuclei. Gilbert and Cameron point out that their model is not expected to be valid for nuclei which have N or Z near a magic number (^{55}Co: N = 28, Z = 27; ^{59}Cu: N = 30, Z = 29).

C. Strength Functions

The proton strength function is $\langle \gamma^2 \rangle / \langle D \rangle$, where $\langle \gamma^2 \rangle$ is the average reduced width per resonance and $\langle D \rangle$ is the average spacing between resonances. Strength functions are listed in table 18 for ^{55}Co and ^{59}Cu. The average reduced width $\langle \gamma^2 \rangle$ is from table 16. The total number of resonances N and the level density ρ are from table 17. Since $\langle D \rangle = \rho^{-1}$, the strength function is $\langle \gamma^2 \rangle \rho$. The uncertainty Δ S.F. is from the statistical uncertainty in the average reduced width, $\sqrt{2/N}\ \langle \gamma^2 \rangle$ (Lynn, 1968).

Table 19 gives <u>lower limits</u> of the strength functions of the ^{60}Ni(p,p) data. Due to the small average widths of the resonances, a large fraction of the resonances were unobserved. In addition, more of the resonances have questionable spin assignments. For these reasons the resonances were grouped according to ℓ-value. The strength function was determined from

$$S.F. = \left(\sum_{i=1}^{N} \frac{\gamma_i^2}{N} \right) \left(\frac{\Delta E}{N-1} \right)^{-1}$$

Table 18.

Strength Functions for ^{55}Co and ^{59}Cu

^{55}Co

J^{π}	S.F.^{c}	S.F.	ΔS.F.
$1/2^{+}$	0.027	0.028	0.012
$1/2^{-}$	0.019	0.020	0.009
$3/2^{-}$	0.014	0.015	0.005
$3/2^{+}$	0.035	0.034	0.014
$5/2^{+}$	0.066	0.066	0.016

^{59}Cu

J^{π}	S.F.^{c}	S.F.	ΔS.F.
$1/2^{+}$	0.086	0.086	0.038
$1/2^{-}$	0.023	0.024	0.010
$3/2^{-}$	0.013	0.014	0.005
$3/2^{+}$	0.079	0.078	0.037
$5/2^{+}$	0.079	0.078	0.032

Table 19.

Strength Function for ^{61}Cu

ℓ	$\Sigma\gamma_i$(keV)	N	ΔE (MeV)	S.F.	ΔS.F.
0	20.44	21	0.439	0.044	0.014
1	14.36	25	0.484	0.028	0.008
2	39.26	29	0.501	0.076	0.020

S.F.^{c} : strength function corrected for missing levels. S.F.^{c} was obtained from S.F.$^{c} = \langle\gamma_c^2\rangle\rho_c$ where $\langle\gamma_c^2\rangle$ and ρ_c were obtained from tables 16 and 17, respectively.

where γ_i^2 is the reduced width of the i^{th} resonance, N is the number of resonances, and ΔE is the energy difference between the proton energies of the highest and lowest resonance.

Outlaw (1974) summarized the proton strength function data obtained in this laboratory. For $1/2^+$ states near mass 54 typical values of the strength function are 0.06; the ^{54}Fe value is anomalously low -- S.F. $\sim$0.01. This value was obtained from the three $1/2^+$ resonances observed by Lindstrom (1970) below 3.29 MeV. In the present experiment several large s-wave resonances were observed near 4 MeV in ^{54}Fe(p,p); these widths were omitted in determining the strength function since the large resonances could be fragments of an isobaric analogue resonance (IAR) (see section IV A). The resulting strength function value of 0.027 is still only about half as large as that expected from systematics. Including these large resonances and Lindstrom's $1/2^+$ resonances gives S.F. = 0.063 which does agree with the expected value of 0.06.

The assignment of these large s-wave resonances as an analogue state also leads to several other problems. The only possible parent state was observed by <u>one</u> group of experimenters in a <u>pick-up</u> reaction, and no spectroscopic factor was obtained. The Coulomb energy seems a little low, and, for an analogue state, the "spreading width" of the structure seems rather large (Brändle et al. (1975) obtained

75 keV for the spreading width). In the present experiment, a spectroscopic factor of 0.4 was obtained; such a strong analogue state is expected to be seen easily in the ^{54}Fe (d,p) reaction. Inspection of the ^{54}Fe(d,p) spectra of Sperduto and Buechner (1963) and of Maxwell and Parkinson (1964) reveals no such level (or contaminant) near the expected excitation energy.

An alternate explanation is that this cluster of large s-wave resonances is some other type of intermediate structure. The simplest possibility is a (2p - 1h) doorway state. The single particle state may distribute its strength to such doorway states which in turn enhance the background states (Lane 1969). That is, the single particle giant resonance can deposit its strength in clusters, leaving regions in the spectrum which have anomalously low strength function values.

If the s-wave structure in ^{54}Fe(p,p) were such a doorway state, then the small strength function obtained from Lindstrom's data is understandable: the local s-wave strength is concentrated in the doorway state. Although (2p - 1h) doorway states have been observed in this mass region (Elwyn and Monahan 1968, Ikegami and Emery 1964), and there are good reasons for assuming that this s-wave structure is such a doorway state, positive identification must be withheld until suitable calculations are performed.

CHAPTER V

SUMMARY

The energy range of an electrostatic-analyzer homogenizer system has been extended by the introduction of a molecular dissociator which operated on the diatomic hydrogen ions from a Van de Graaff accelerator. Energy resolutions of 300 - 400 eV with solid targets have been obtained routinely up to proton energies of 4.5 MeV with an electrostatic analyzer originally limited to measuring proton energies below 2.7 MeV. Improvements to the Van de Graaff accelerator are expected to permit this system to operate as high as 5 or 6 MeV.

Proton elastic and inelastic scattering excitation functions were measured for ^{54}Fe (E_p = 3.28 to 4.53 MeV), ^{58}Ni (E_p = 3.11 to 4.20 MeV), and ^{60}Ni (E_p = 2.95 to 3.45 MeV). The excitation functions were measured at 160°, 122°, 105°, and 90° for the elastically scattered protons and 160°, 122°, and 90° for the inelastically scattered

protons. The data were fit with an R-matrix code; and resonance parameters were extracted for 131 resonances in ^{55}Co, 86 resonances in ^{59}Cu, and 75 resonances in ^{61}Cu.

Four isobaric analogue resonances (IAR) were positively identified in ^{55}Co and seven were tentatively identified. Two IAR were positively identified in ^{59}Cu and four were tentatively identified. Coulomb energies and spectroscopic factors were calculated. Spins, parities, and spectroscopic factors of the IAR are in excellent agreement with those of the parent states; Coulomb energies agreed well with that of the ground state for both ^{55}Co and ^{59}Cu.

A statistical analysis of the reduced widths was performed on several species of levels of ^{55}Co and ^{59}Cu. The width distributions agreed reasonably well with the Porter-Thomas distribution. The spin and energy dependence of level densities in ^{55}Co and ^{59}Cu were investigated. Level densities calculated with the formula of Gilbert and Cameron were compared with the observed level densities.

Proton strength functions were determined for each spin and parity with $\ell<3$ for ^{55}Co and ^{59}Cu, and for $\ell=0,1$, and 2 for ^{61}Cu. The anomalous behavior of the proton s-wave strength function of ^{55}Co was examined.

It is hoped that more experiments will be performed with the high resolution system that has been developed. In particular, it would be interesting to extend measurements of ^{58}Ni(p,p) to higher energies in order to see if the

s-wave and d-wave strength functions continue to increase rapidly. It would also be of value in understanding the s-wave strength function in ^{54}Fe(p,p) if appropriate doorway state calculations were performed.

APPENDIX

SYSTEMATIC ENERGY-MEASUREMENT ERRORS

As discussed in Chapter II, energies were obtained by accurately measuring the voltage between the plates of the ESA. The voltage divider used to measure this voltage (see figure 6) was adjusted so that the voltage read on the differential voltmeter (DVM) was the energy of the reaction. The calibration was performed at the threshold of the $^{13}C(p,n)$ reaction at 3.2357 MeV; afterwards, the reaction energy was assumed to be that read on the DVM. This procedure gives energies which are accurate within $\sim 0.5\%$. The resonance energies were further adjusted to compensate for energy measurement errors caused by the system design and by relativistic effects. In this appendix an expression for these corrections is derived, and measurements which were performed to test the validity of this expression are presented.

An absolute energy measurement with a cylindrical electrostatic analyzer requires a detailed knowledge of the geometrical parameters of the analyzer as well as a knowledge of the plate voltages and of the magnetic field between the plates (e.g., Herb 1949). In the present system, energies are measured from a calibration energy. For this reason, the following discussion omits several higher order effects which are thought either to be negligible or to cancel in the calibration process (for example,

cylindrical corrections to the voltage between the plates cancel completely).

If the particle follows an ideal circular path through the ESA, then relativistic classical mechanics yields[1]

$$eE = \left(\frac{m}{\sqrt{1-v^2/c^2}}\right)\frac{v^2}{r} = \frac{2T}{r}\left(\frac{1+\gamma}{1+2\gamma}\right) \qquad (1)$$

where

E ≡ electric field,

T ≡ kinetic energy,

r ≡ radius of curvature,

$\gamma \equiv T/1880$ (T in MeV).

Inside a cylindrical ESA, the field can be shown to be related to the plate voltages as follows:

$$E = \frac{V_A}{r \ln\left[(r+d/2)/(r-d/2)\right]} \qquad (2)$$

where

V_O ≡ voltage of the outer plate,

V_I ≡ voltage on the inner plate,

$V_A \equiv V_O - V_I$,

r ≡ average radius of curvature

(r (outer plate) + r (inner plate))/2,

d ≡ plate separation

(r (outer plate) - r (inner plate)).

---

1. e.g., Herb et al. (1949)

Equations 1 and 2 yield

$$T = \frac{e}{2} V_A \alpha \tag{3}$$

where

$$\alpha = \left(\frac{1 + 2\gamma}{1 + \gamma}\right)\left(\ln\left(\frac{r + d/2}{r - d/2}\right)\right)^{-1}. \tag{4}$$

The kinetic energy of the particles inside the analyzer (T) is different from that outside (T_o) since the ideal path is not at ground potential. If V(r) is the potential, then

$$T = T_o - eV(r) . \tag{5}$$

Inside a cylindrical ESA this potential is

$$V(r) = V_o - \beta V_A \tag{6}$$

where

$$\beta \equiv \frac{\ln(1 + d/(2r))}{\ln\left[(1 + d/(2r))/(1 - d/(2r))\right]} . \tag{7}$$

In the dissociation process, the energy of the protons is affected by the voltage of the dissociator (V_D):

$$T_o = \frac{e}{2}\left(V_V + V_D\right) \tag{8}$$

where

$V_V \equiv$ voltage of the Van de Graaff.

Finally, the energy of the reaction (T_R) is affected

by the voltage of the target (V_T):

$$T_R = eV_V - eV_T . \tag{9}$$

From these expressions the reaction energy (T_R) may be obtained in terms of the other system parameters[1]:

$$T_R = eV_A(\alpha - 2\beta) - eV_S \tag{10}$$

where

$$V_S \equiv V_T + V_D - 2V_0 \equiv \text{"system voltage"}. \tag{11}$$

V_A is measured with a voltage divider network (see figure 6) such that

$$V_A = k V_{DVM} \tag{12}$$

where

k = ratio of the resistances,

V_{DVM} = voltage read on the differential voltmeter.

"k" is adjusted so that at the calibration energy

$$T_R^c = 10^6 e V_{DVM}^c \tag{13}$$

(the "c" indicates the value at calibration).

---

1. Equation 10 is not explicitly solved for T_R in terms of the other system parameters since α is dependendent on T_R. In the nonrelativistic limit, $\alpha \rightarrow 1$; and this implicit dependence of T_R on itself disappears. Moreover, in the derivation of equation 28, it is shown that that this implicit dependence disappears even for a first order calculation of the relativistic contribution to the energy-measurement error.

Measured energies (T_{RM}) are then read from the DVM:

$$T_{RM} \equiv 10^6 e V_{DVM} . \tag{14}$$

The difference between the "real" energy (T_R) and that measured (T_{RM}) is the error($\mathcal{E}$):

$$\mathcal{E} \equiv T_R - T_{RM} . \tag{15}$$

Equations 10 to 15 give

$$\mathcal{E} = ek V_{DVM} (\alpha - 2\beta) - eV_S - \frac{V_{DVM}}{V_{DVM}^c} \left(ek V_{DVM}^c (\alpha^c - 2\beta) - e V_S^c \right), \tag{16}$$

or simplifying,

$$\mathcal{E} = \frac{T_{RM}}{10^6} k (\alpha - \alpha^c) + \frac{T_{RM}}{T_{RM}^c} e V_S^c - e V_S . \tag{17}$$

(Note that terms involving β, the parameter characterizing the cylindrical correction to the voltage between the plates, dropped out.) If relativistic effects are neglected $\gamma \to 0$ and the first term in equation 17 vanishes. If the system potential V_S were zero, then the second term would be zero.

We therefore define the relativistic and system errors as

$$\mathcal{E} \equiv \frac{k T_{RM}}{10^6} (\alpha - \alpha^c) \tag{18}$$

and

$$\mathcal{E}_S \equiv e \left(\frac{T_{RM}}{T_{RM}^c} V_S^c - V_S \right), \tag{19}$$

respectively, with $\mathcal{E} = \mathcal{E}_R + \mathcal{E}_S$. (20)

To simplify $\mathcal{E}_R$ recall from equation 3 and equation 12 that

$$T = \frac{e}{2} V_A \alpha = \frac{ke}{2} V_{DVM} \alpha \frac{k\alpha}{2} \frac{T_{RM}}{10^6} \tag{21}$$

therefore

$$\mathcal{E}_R = \frac{2T}{\alpha} (\alpha - \alpha^c). \tag{22}$$

Expanding $(1+2\gamma)/(1+\gamma)$ in a Taylor's series gives:

$$\mathcal{E}_R = 2T \left(\frac{(1+\gamma-\gamma^2+\cdots) - (1+\gamma^c-(\gamma^c)^2+\cdots)}{(1+\gamma-\gamma^2+\cdots)} \right) \tag{23}$$

and since

$$\gamma = \frac{T \text{ (in MeV)}}{1880} \sim \frac{1}{500}, \tag{24}$$

then

$$\mathcal{E}_R \approx 2T(\gamma - \gamma^c) = 2T(\text{MeV}) \frac{(T-T^c)}{1880}. \tag{25}$$

Equation 25 gives a good approximation of $\mathcal{E}_R$ except that values of T are not readily available. T_{RM} is the quantity measured; in the following it will be shown that when calculating $\mathcal{E}_R$ with equation 25, T can be replaced by $T_{RM}/2$. With equations 5, 6, 8, 9, 12, 14, and 15, one obtains

$$T = \frac{T_{RM}}{2} \left(1 + \frac{\beta k}{10^6}\right) + \left(\mathcal{E} + \frac{eV_s}{2}\right). \tag{26}$$

Since in this system $d/2r \sim 1/262$ and $k \sim 72{,}000$, then $\beta \sim 1/2$ and $(\beta k/10^6) << 1$. Therefore, to a good approximation

$$T \approx \frac{T_{RM}}{2} + \mathcal{E} + \frac{eV_s}{2}. \tag{27}$$

Moreover, $T_{RM} \sim 4$ MeV, $\mathcal{E} < 50$ keV, and $eV_S < 50$ keV; thus $T \approx T_{RM}/2$. With equation 25 and $T = T_{RM}/2$, the final form of the relativistic error is obtained[1]:

$$\mathcal{E} \approx T_{RM}\,(MeV)\,\frac{(T_{RM} - T_{RM}^{c})}{3760}\,, \tag{28}$$

and the total error is

$$\mathcal{E} = T_{RM}\,(MeV)\,\frac{(T_{RM} - T_{RM}^{c})}{3760} + \left(\frac{T_{RM}}{T_{RM}^{c}}\; eV_S^{c} - eV_S\right). \tag{29}$$

As a test of this equation, the $^{13}C(p,n)$ and $^{7}Li(p,n)$ threshold energies were measured with several outer plate voltages. Figure 46 shows the measured threshold energies for various values of V_0. The solid lines are calculated from equation 29 with $T_{RM}^{c} = 3.2357$ MeV and $V_0 = 14.96$ kV. The difference between the experimental result and the calculation for the $^{7}Li(p,n)$ threshold is about 1.6 keV. Since the energy[2] diffenence is 3.2357–1.8806 = 1.3551 MeV, the correction equation yields energies which are in fair agreement with the data.

As another test of the correction equation, the resonance energies (which were corrected by equation 30) of several well identified levels were compared to the corresponding energies independently measured by Brandle et al.

---

1. Replacing T by $T_{RM}/2$ was not well justified since the <u>difference</u>, $T - T^{c}$, is a factor in equation 25. For this reason equation 28 is not a good approximation of $\mathcal{E}_R$ for small values of $T - T^{c}$; in this case however, the relativistic error, $\mathcal{E}_R$, is insignificantly small (<100 eV).
2. Threshold values are from Marion (1966).

Figure 46. Measured Values of $^{13}C(p,n)$ (upper) and $^{7}Li(p,n)$ (lower) Threshold Energies for Various Voltages on the Outer Plate of the ESA. The solid lines were obtained from equation 30 with a calibration energy and outer plate voltage of 3.2357 MeV and 14.96 kV.

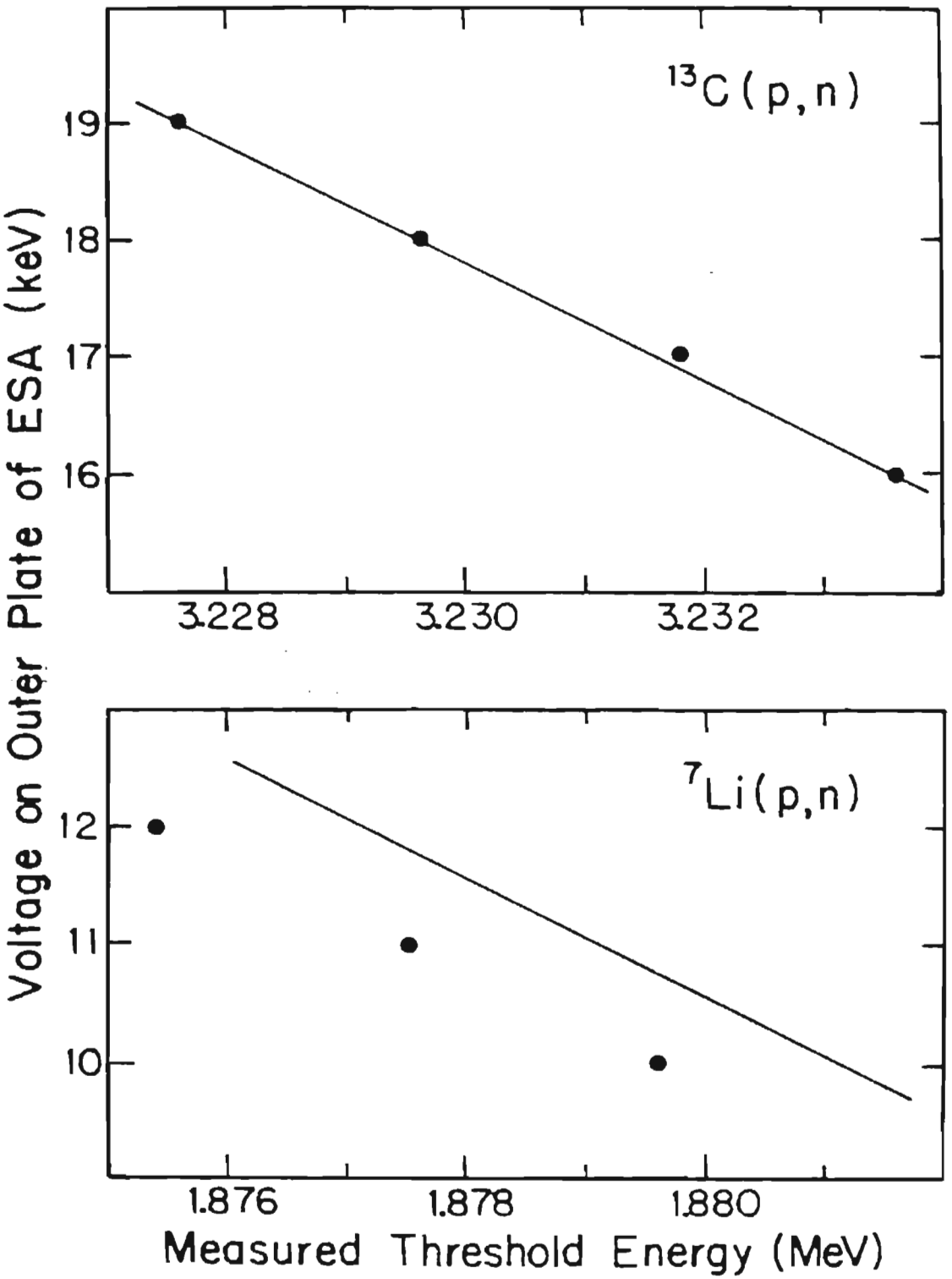
$^{13}C(p,n)$
19
18
17
16
3.228
3.230
3.232
$^{7}Li(p,n)$
12
11
10
1.876
1.878
1.880
Voltage on Outer Plate of ESA (keV)
Measured Threshold Energy (MeV)

(1975) and Arai et al. (1976). Figure 15 shows the difference between the present resonance energies and those of Brändle and Arai, plotted as a functon of energy. Excellent agreement is found except for the discontinuities at 3.4 and 3.9 MeV in ^{58}Ni(p,p). A reexamination of the present measurements suggests that the observed energy shifts are not caused by the present experiment: in order to improve the data, many measurements were repeated. The resonance energies which were measured near these discontinuties on these different occasions were in agreement with each other and in disagreement with Arai et al.

There are several possible errors which have not been discussed. Herb (1949) measured the magnetic field between the plates of the ESA and included this in making absolute energy measurements. With Herb's values for the magnetic field, the energy error incurred in going from a calibration energy of 3.2 MeV to a measured energy of 4.2 MeV was estimated as only 250 eV. There is an energy loss for the average proton in the dissociation process. This loss should be on the order of two hundred eV or less and was neglected. There are also several ways that the proton beam and the molecular beam can have different energies. A study of these possibilities suggests that the energies would not differ by more than a few hundred eV. Perhaps the biggest error would arise in the positioning of the entrance and exit slits of the ESA and in the non-zero thicknesses of

these slits. It is estimated that these errors could contribute to an uncertainty of V_S of ±3 kV. This in turn leads to an uncertainty in the calculated values of $\mathcal{E}$ which is magnified as the energy span is increased. Such an effect could account for the 1.6 keV discrepancy shown in figure 46.

REFERENCES

LIST OF REFERENCES

J. A. Aymer, H. R. Hiddleston, S. E. Darden, and A. A. Rollefson, Nucl. Phys. A207 (1973) 596.

E. Arai, M. Ogawa, and H. Sato, Nucl. Phys. A256 (1976) 127.

B. L. Auble and J. Rapaport, Nuclear Data Sheets, Vol. 3, ed. K. Way (Academic Press, New York, 1970) p. B3-3, B4-1.

H. A. Bethe, Phys. Rev. 50 (1936) 332.

H. A. Bethe, Rev. Mod. Phys. 9 (1937) 69.

J. M. Blatt and V. F. Weisskopf, Theoretical Nuclear Physics, (John Wiley and Sons, New York, 1952) p. 156.

V. P. Bochin, K. I. Zherebtsova, V. S. Zolotarev, V. A. Komarov, L. V. Krasnov, V. F. Litvin, Y. A. Nemilov, B. G. Novatsky, S. Piskorzh, Nucl. Phys. 51 (1964) 161.

N. Bohr, Nature 137 (1936) 344.

A. Bohr and B. R. Mottelson, Nuclear Structure, Vol. 1, (W. A. Benjamin, Inc., New York, 1969) p. 171.

H. Brändle, V. Meyer, and M. Salzmann, Nucl. Phys. A249 (1975) 269.

G. Breit and E. Wigner, Phys. Rev. 49 (1936) 54.

J. C. Browne, H.W. Newson, E. G. Bilpuch, and G. E. Mitchell, Nucl. Phys. A153 (1970) 481.

M. S. Chowdhury and H. M. Sen Gupta, Nucl. Phys. A205 (1973) 454.

B. L. Cohen, R. H. Fulmer, A. L. McCarthy, Phys. Rev. 126 (1962) 698.

T. G. Dzubay, E. G. Bilpuch, F. O. Purser, J. D. Moses, H. W. Newson, and G. E. Mitchell, Nucl. Instrum. Methods 101 (1972) 407.

A. J. Elwyn and J. E. Monahan, Phys. Rev. Lett. 20 (1968) 119.

H. Feshbach, A. K. Kerman, and R. H. Lemmer, Ann. Phys. (N. Y.) 41 (1967) 230.

F. L. Friedman and V. F. Weisskopf, Niels Bohr and the Development of Physics, (Pergamon Press, London, 1955).

R. H. Fulmer, and A. L. McCarthy, Phys. Rev. 131 (1963) 2133.

D. G. Gerke, "$C^{12}(d,p)C^{13}$: Distorted Wave Born Approximation Analysis of Proton Angular Distribution and Proton-Gamma Angular Correlation", unpublished Ph.D. dissertation, Duke University (1963).

A. Gilbert and A. G. W. Cameron, Can. J. Phys. 43 (1965) 1446.

L. R. Hafstad and M. A. Tuve, Phys. Rev. 47 (1935) 506.

H. L. Harney, unpublished computer code (1969).

W. Heisenberg, Z. Phys. 77 (1932) 1.

R. G. Herb, S. C. Snowdon, and O. Sala, Phys. Rev. 75 (1948) 246.

H. Ikegami and G. T. Emery, Phys. Rev. Lett. 13 (1964) 26.

G. A. Jones, A. M. Lane, and G. C. Morrison, Phys. Lett. 11 (1964) 329.

P. L. Kapur and R. Peierls, Proc. R. Soc. Lond. A166 (1938) 277.

G. A. Keyworth, "A High Resolution Study of Isobaric Analogue States in ^{41}K and ^{23}Na, unpublished Ph.D. dissertation, Duke University (1968).

A. M. Lane, Isospin in Nuclear Physics, ed. D. H. Wilkinson, (North-Holland, Amsterdam, 1969) p. 509.

A. M. Lane and R. G. Thomas, Rev. Mod. Phys. 30 (1958) 257.

D. P. Lindstrom, unpublished computer code (1969).

D. P. Lindstrom, "Fine Structure of Analogue States in ^{55}Co, ^{57}Co, and ^{59}Co", unpublished Ph.D. dissertation, Duke University (1970).

D. P. Lindstrom, H. W. Newson, and E. G. Bilpuch, Nucl. Phys. A168 (1971) 37.

J. E. Lynn, The Theory of Neutron Resonance Reactions, (Clarendon Press, Oxford, 1968) p. 202, 226.

J. B. Marion, Rev. Mod. Phys. 38 (1966) 660.

P. B. Moon and R. Tillman, Nature 135 (1935) 904.

J. D. Moses, "A High Resolution Study of Isobaric Analogue Resonances in ^{51}Mn, ^{53}Mn, and ^{55}Mn", unpublished Ph.D. dissertation, Duke University (1970).

T. R. Ophel and G. W. Kerr, Nucl. Instrum. Methods 128 (1975) 129.

D. A. Outlaw, "A High-Resolution Study of Proton Resonances in ^{31}P, ^{35}Cl, and ^{93}Tc", unpublished Ph.D. dissertation, North Carolina State University (1974)

P. B. Parks, H. W. Newson, and R. M. Williamson, Rev. Sci. Instrum. 29 (1958) 834.

C. E. Porter and R. G. Thomas, Phys. Rev. 104 (1956) 483.

H. Pose, Z. Phys. 30 (1929) 780.

H. Pose, Z. Phys. 64 (1930) 1.

N. H. Prochnow, H. W. Newson, E. G. Bilpuch, and G. E. Mitchell, Nucl. Phys. A194 (1972) 353.

D. Robson, Phys. Rev. 137 (1965) B535.

D. Robson, Isospin in Nuclear Physics, ed. D. H. Wilkinson, (North Holland, Amsterdam, 1969) p. 461.

D. L. Sellin, "Excited States in ^{19}F", unpublished Ph.D. dissertation, Duke University (1969).

E. Sherr, B. F. Bayman, E. Rost, M. E. Rickey, and C. G. Hoot, Phys. Rev. 139 (1965) B1271.

A. Sperduto, and J. Rapaport, MIT--LNS Progr. Rept., p.134 (November 1961); NYO-2668 (1961).

A. Sperduto and W. W. Buechner, Phys. Rev. 134 (1964) B142.

F. Stecher-Rasmussen, J. Kopecky, K. Abrahms, and W. Ratynski, Nucl. Phys. A181 (1972) 250.

G. M. Temmer, Isospin in Nuclear Physics, ed. D. H. Wilkinson, (North Holland, Amsterdam, 1969) p. 708.

W. J. Thompson, J. L. Adams, and D. Robson, Phys. Rev. 173 (1968) 975.

J. Vervier, Nuclear Data Sheets, Vol. 2, ed. K. Way (Academic Press, New York, 1969) p. B2-5-1.

B. E. Warren, J. L. Powell, and B. G. Herb, Rev. Sci. Instrum. 18 (1947) 559.

V. F. Weisskopf, Phys. Rev. 52 (1937) 295.

V. F. Weisskopf and E. Wigner, Z. Phys. 63 (1930) 54.

E. P. Wigner, Ann. Math. 62 (1955) 548.

E. P. Wigner, Phys. Rev. 51 (1937) 106.

E. P. Wigner and L. Eisenbud, Phys. Rev. 72 (1947) 29.

W. M. Wilson, "A High Resolution Study of Proton Resonances in ^{41}Sc, ^{43}Sc, and ^{45}Sc", unpublished Ph.D. dissertation, Duke University (1973).

BIOGRAPHY

David Sheldon Flynn

Personal:	Born June 2, 1942, Orlando, Florida
Education:	A.A., Orlando Junior College, 1968
	B.S. in physics, University of Florida, 1970
Positions:	N.D.E.A. Fellow, Duke University, 1970 – 1973
	Research Assistant, Duke University, 1973 - 1974
	Teaching Assistant, Duke University, Fall 1974
	Research Assistant, Duke University, 1975 – present
Membership:	American Physical Society